Mathematical Model to Analyze the Heat Transfer in Tunnel Kilns for Burning of Ceramics

Dissertation
zur Erlangung des akademischen Grades

Doktoringenieur
(Dr.-Ing.)

von **M.Sc. Hassanein Abdel Mohsen Hassanein Refaey**
geb. am 7. February 1978 in Qaliubiya, Ägypten

genehmigt durch die Fakultät für Verfahrens- und Systemtechnik
der Otto-von-Guericke-Universität Magdeburg

Prüfungskommission:

Prof. Dr.-Ing. Eckehard Specht (Gutachter und Betreuer)
Prof. Dr.-Ing. Gerd Walter (Gutachter)
Dr.-Ing. Anne Tretau (Gutachterin)
Prof. Dr.-Ing. Dominique Thévenin (Vorsitzender)

eingereicht am: 05.02.2013
Promotionkolloquium am: 02.05.2013

Preface

This dissertation is submitted to Otto von Guericke University Magdeburg for the degree of Doctor of Engineer. The research described herein was conducted under the supervision of Prof. Eckehard Specht between September 2009 and January 2013. To the best of my knowledge, this work is original, except where suitable references are made to previous works. Neither this, nor any substantially similar dissertation has been submitted for any degree, diploma or qualification at any other university or institution.

Hassanein Refaey
Magdeburg, Germany
30 January 2013

Don't think of it as being outnumbered, think of it as a wide target selection.

Acknowledgement

Hassanein Refaey
Magdeburg, Germany
30 January 2013

Contents

Nomenclature

Only commonly used symbols are listed below. The meanings of all other symbols are defined explicitly within the text.

Latin letter symbols

A	area, m^2
A_z	area per unit length, m^2/m
A_T	transverse area, m^2
a_1	slope of the equation
B_k	kiln width, m
B_c	car width, m
c	specific heat, kJ/(kg·K)
c_{pg}	specific heat of gas, kJ/(kg·K)
c_{pgo}	specific heat of air, kJ/(kg·K)
c_T	specific heat of transportation, kJ/(kg·K)
c_s	specific heat of solids, kJ/(kg·K)
D	pipe outside diameter, m
d	cylinder diameter, m
E	specific energy consumption, MJ/kg
e	exponential function
F_a	tubes arrangement factor
$F_{cyl \rightarrow pl}$	view factor from cylinder to perforated plate
$F_{fc \rightarrow pl}$	view factor from fire clay plate to perforated plate
$F_{pl \rightarrow p}$	view factor from perforated plate to pipe
f	percentage, %
$\dot{H}$	enthalpy flow, kW
$d\dot{H}$	change in enthalpy flow, kW
H_k	kiln height, m
H_p	pipe height, m
h_{cyl}	cylinder height, m
h_{fc}	fire clay height, m
hu	lower heating value of fuel, kJ/kg
L	air demand, kg_{air}/kg_{fuel}
L_c	characteristic length, m
L_f	firing length, m
L_k	kiln length, m
L_{pre}	preheating length, m

$\dot{M}$	mass flow rate, kg/s
$mbar$	millibar, $100N/m^2$
N	total number of pipes
N_c	number of columns
N_{cars}	number of cars
N_{cyl}	number of cylinders per car, $cylinders/car$
$N_{p_{cars}}$	number of pipes per car, $pipes/car$
N_r	number of rows
Nu	Nusselt number (hD/k)
Nu_D	Nusselt number based on pipe diameter (hD/k)
P	pressure, bar
Pr	Prandtl number for gases determined at gas temperature $(c_p\mu/\lambda_g)$
Pr_s	Prandtl number based on surface temperature
$\dot{Q}_w$	wall heat loss, kW
$d\dot{Q}$	change in heat transfer, kW
Re	Reynolds number (vD/ν)
St	Stanton number
s	beam length, m
S_D	diagonal pitch, m
S_L	longitudinal pitch, m
S_T	transverse pitch, m
td	thermal diffusivity, m^2/s
T	temperature, K
V	volume, m^3
w_a	air velocity, m/s
w_g	gas free stream velocity, m/s
w_{max}	gas maximum velocity, m/s
X_T	transportation percentage, %
$\tilde{X}$	volume concentration of the gas
Z	dimensionless length
z	independent variable

Greek symbols

α	heat transfer coefficient, W/(m^2·K)
ε	emissivity
λ	excess air number
λ_g	thermal conductivity of gas, W/(m·K)
μ_g	dynamic viscosity of gas, kg/(m·s)
ν_g	kinematic viscosity of gas, m^2/s
Ω	heat capacity ratio
Ω'	inverse of heat capacity ratio
Φ	factor
ρ	density, kg/m^3
σ	Stefan-Boltzmann constant, W/($m^2·K^4$)
φ_L	dimensionless longitudinal pitch (S_L/D)
φ_T	dimensionless transverse pitch (S_T/D)

Subscripts

a	air
ad	adiabatic
b	burning
cyl	cylinder
$conv$	convection
d	diameter
D	diameter
Eq	equation
F	fuel
Fig	figure
f	firing
fc	fire clay plate
g	gas
i	inner
in	inlet
k	kiln
m	constant
max	maximum
n	constant
no	nozzle
n_c	constant
n_μ	constant
n_λ	constant
out	outlet
p	pipe
pl	plate
pre	preheating
pro	products
r	radiation
s	solid
t	total
w	wall
z	element in z direction

Abbreviations

1D	one dimension
BVP	boundary value problem
bvp4c	boundary value problem four condition
CFD	computational fluid dynamics
Eq	equation

Eqs	equations
CFD	computational fluid dynamics
Fig	figure
ODE	ordinary differential equation
ODEs	ordinary differential equations
NG	natural gas
STP	standard temperature and pressure

Abstract

An analysis of preheating and burning processes in tunnel kilns was done to develop a simple mathematical model which can be used to predict gas and solid temperature profiles. In the simple model three special cases were studied. In the first case of no firing length, a system of ordinary differential equations was established to simulate the process in the kiln. In addition the analytical solution for that system was also obtained. The model estimated the energy consumption for that case. The second case was established to consider the kiln as a firing zone and obtaining its system of the ordinary differential equations (ODEs). As a consequence, the energy consumption for different excess air number was represented. The third case was done to the kiln with firing zone equal to preheating zone.

Moreover, the model studied the effect of the firing zone length on the energy consumption. It was evident that the energy consumption always increases progressively with the firing zone length. Therefore, up to approximately $\sim$30 %, the increase is relatively low and as a consequence, the firing zone length should be as short as possible for low energy consumption. In order solve all the foregoing ODEs systems to obtain the temperature profile MATLAB was used, specifically the bvp4c code.

The heat transfer mechanism is complex inside the tunnel kiln, due to the interactions of kiln car, kiln furniture, product types and product arrangements in the kiln. Therefore, it is important to establish a model to analyze the heat transfer in the kiln. Moreover, the type, the shape, and the arrangement of products are important in the analysis calculations. Consequently, the vitrified clay pipes were taken as a product of a simple shape to analyze the heat transfer. The system in this case included not only the ODEs for the product but also for the kiln furniture materials. The temperature profiles for products and kiln furniture were represented as well as gases temperature profiles. The heat transfer coefficients for both convection and radiation have been calculated along the two zones.

A simple mathematical model has been done for the two zones with an air addition along the preheating zone for the Sanitaryware kiln. A comparison between the new model results and the simple mathematical model results have been done to show the effect of this air addition on the energy consumption.

A computational fluid dynamics (CFD) was established for the Sanitaryware kiln to study the gas circulation in the cross section. The 3D simulations were carried out with the commercial software package FLUENT 6.3 for the preheating zone to show the flow field around the Sanitaryware. The flow field is distinctly visualized by images of velocity vectors. The CFD results showed that there was a good mixing of the gases

around the Sanitaryware. The study demonstrates simulation upon a scalable segment geometric model is capable of providing the main flow feature in the preheating zone of Sanitaryware kiln, which is nearly impossible to study in experimental setups. The average velocity inside the observed domain is low, around 1 m/s.

Zusammenfassung

In dieser Arbeit wird der Aufheiz- und Brennvorgang in Tunnelöfen analysiert. Es wird ein vereinfachtes mathematisches Modell entwickelt, das auf Grundlage von Energie- und Massenbilanzen das axiale Temperaturprofil anhand eines Systems von gewöhnlichen Differentialgleichungen beschreibt. Dabei werden drei gesonderte Fälle betrachtet. Der erste Fall beschreibt den Ofenprozess, wenn die Länge der Brennzone sehr klein ist. Somit wird von einem punktförmigen Wärmeeintrag am Ende der Aufheizzone ausgegangen. Im zweite Fall wird der gesamte betrachtete Ofenabschnitt als Brennzone angenommen, so dass die zugeführten Brenngase gleichmäßig auf die Ofenlänge verteilt werden. Der dritte Fall geht von einer gleichlangen Aufheiz- und Brennzone aus. Die Brenngase werde daher in der zweiten Hälfte des Ofens eingebracht.

Der Energieverbrauch wird in Abhängigkeit von wichtigen Betriebsparametern, wie z. B. der Luftzahl und der Länge der Brennzone, dargestellt. Es wird gezeigt, dass der Energieverbrauch mit der Länge der Brennzone progressiv zunimmt. Dadurch steigt der Energieverbrauch nur langsam an, wenn der Anteil der Brennzonenlänge im betrachteten Ofenabschnitt klein ist. Ein geringer Energieverbrauch kann somit erreicht werden, wenn die Länge der Brennzone minimiert wird. Zur Lösung der Differentialgleichungen wurde MATLAB, speziell der Löser "bvp4c", verwendet, um die Temperaturprofile der einzelnen Stoffströme im Tunnelofen anhand gegebener Randbedingungen berechnen zu können.

Der Wärmeübergangsmechanismus in Tunnelöfen ist komplex, da hier der Ofenwagen, das Brenngut sowie die Transporthilfsmittel in Wechselwirkung stehen. Es wird ein Modell zur Beschreibung des Wärmeübergangs präsentiert, das anhand von Steinzeugrohren die Art, die Form und den Besatz des Brenngutes berücksichtigt. Neben dem Gas- und Produktstrom werden hier Differentialgleichungen zur Bestimmung der Temperaturprofile des Ofenwagens und der Transporthilfsmittel angegeben. Der Wärmeübergangskoeffizient durch Konvektion sowie Strahlung konnte dadurch entlang der Aufheiz- und Brennzone bestimmt werden.

Des Weiteren wurde ein einfaches mathematisches Modell entwickelt, welches eine zusätzliche Luftzufuhr in der Aufheizzone von Tunnelöfen für Sanitärware berücksichtigt. Ein Vergleich zu den vorherigen Ergebnissen zeigt den Einfluss dieser zusätzlichen Luftzufuhr auf den Energieverbrauch. Anschließend wurde eine numerische Simulation der Gaszirkulation (CFD) im Querschnitt eines solchen Tunnelofenabschnitts mit dem Softwarepaket FLUENT 6.3 durchgeführt. Durch die drei-dimensionale Simulation kann unter anderem das Geschwindigkeitsfeld durch Vektoren in der Nähe der Sanitärware visualisiert werden. Die Simulationsergebnisse zeigen, dass die Sanitärware vom Gas gut umströmt wird. Außerdem demonstriert diese Untersuchung, dass durch die numerische

Simulation die Beschreibung der Strömungseigenschaften in der Aufheizzone von Öfen für Sanitärware, die durch Experimente nahezu nicht bestimmbar sind, möglich ist. Die mittlere Strömungsgeschwindigkeit im untersuchten Bereich ist gering und liegt bei etwa 1 m/s.

Chapter 1

Introduction

1.1 Introduction

Reducing energy consumption is one of the most important priorities of modern life. Therefore, it is of interest to reduce energy consumption in industrial processes, especially of ceramic products, which play a significant role in everyday human life. For example, there are numerous commonly used ceramic products including:

- refractory bricks

- high voltage electrical insulators

- roof tiles

- wall and floor tiles

- sanitary ware

- vitrified clay products

- table-and ornamental ware (household ceramics)

- technical ceramics.

The energy consumption for each type of product fluctuates greatly between the products of ceramics. For example, the maximum energy consumed for production of technical ceramic is $50\,\mathrm{MJ/kg}_s$ and the minimum energy consumed for the production of wall and floor tiles is $2.3\,\mathrm{MJ/kg}_s$, even though these two products are produced in tunnel kiln and have the same production sequences. In addition, the two most important product requirements for customers are high quality and low cost. Furthermore, environmental constraints, in terms of reducing emissions of the combustion process of the kilns constitute a restriction on design and calculations. Moreover, due to the high energy price, caused by the energy crisis, energy consumption in the tunnel kiln has to be reduced. Experimentation is also difficult in tunnel kiln, they can reach a length of 180 meters and have production cycles that can last days. In addition, the cost of experiments in the tunnel kiln is high. Also optimization of the process by experiments is difficult, therefore a mathematical model is required for a process simulation to find a solution for energy reduction. According to the large dimension of tunnel kiln, it is difficult to apply commercial CFD codes which need high computational time. As a solution, specific codes and models to solve the thermal problem involved in the tunnel kiln was developed.

1.2   Ceramic

Ceramic products are one of the most commonly used products in daily life and industry. The word ceramic [1] is a word derived from the Greek word (keramikos) which means pottery. "Ceramic" can be used to indicate making things from minerals. Pottery and bricks were found in ancient Roman, Chinese, Japanese civilizations and used for building towers of temples and palaces. The pharaohs' in ancient Egypt used glazed ceramic plates as wall decorations for the pyramids. In addition, porcelain making has been known by ancient Chinese people. Today ceramics include numerous products with a small fraction of clay or none at all. The following sections discuss ceramic classifications, production stages, and the firing process.

1.2.1   Ceramic classification

There are two kinds of ceramic classifications: traditional ceramics and ceramic products. There is also a different classification of ceramic [2]. These classifications are inorganic and non-metallic solids which subjected to high temperature in manufacture and/or use. Ceramics can also be porous or vitrified, glazed or unglazed. The compositions of most common ceramics are oxides, carbides, and nitrides. Ceramic processing generally involves high temperatures, to produce heat resistance materials or refractory.

Ceramic products are produced from unrefined clay and combinations of refined clay and powdered or granulated non-plastic minerals. In traditional ceramics, the clay content exceeds 20 percent. There are two general kinds of traditional ceramics [3]

- Pottery

- Whiteware.

Pottery : Ceramics that contains clay and are not used for structural, technical, or refractory purposes. The term ceramics is used to describe materials of the pottery industry. Pottery could be called in some classifications as heavy ceramics [4].

Whiteware : This type refers to ceramic ware that is white, Ivory, or light gray in color after firing. Whiteware could be called in some classifications as fine ceramics [4] as shown in Fig. 1.1. Whiteware could be further divided to earthenware, stoneware, chinaware, porcelain, and technical ceramics. The following paragraphs explain each of them [4].

- **Earthenware**: Glazed or unglazed nonvitreous (porous) clay-based ceramic ware. It has many applications such as artware, kitchenware, ovenware, tableware, and tile.

- **Stoneware**: This type is vitreous or semivitreous ceramic ware of fine texture. Primarily produced from non-refractory fire clay or some combination of clays, fluxes, and silica that when fired has properties similar to stoneware made from fire clay as shown in Fig. 1.2. There are a various applications for stoneware including: art-ware, chemical ware, cookware, drainpipe, kitchenware, tableware, and tile.
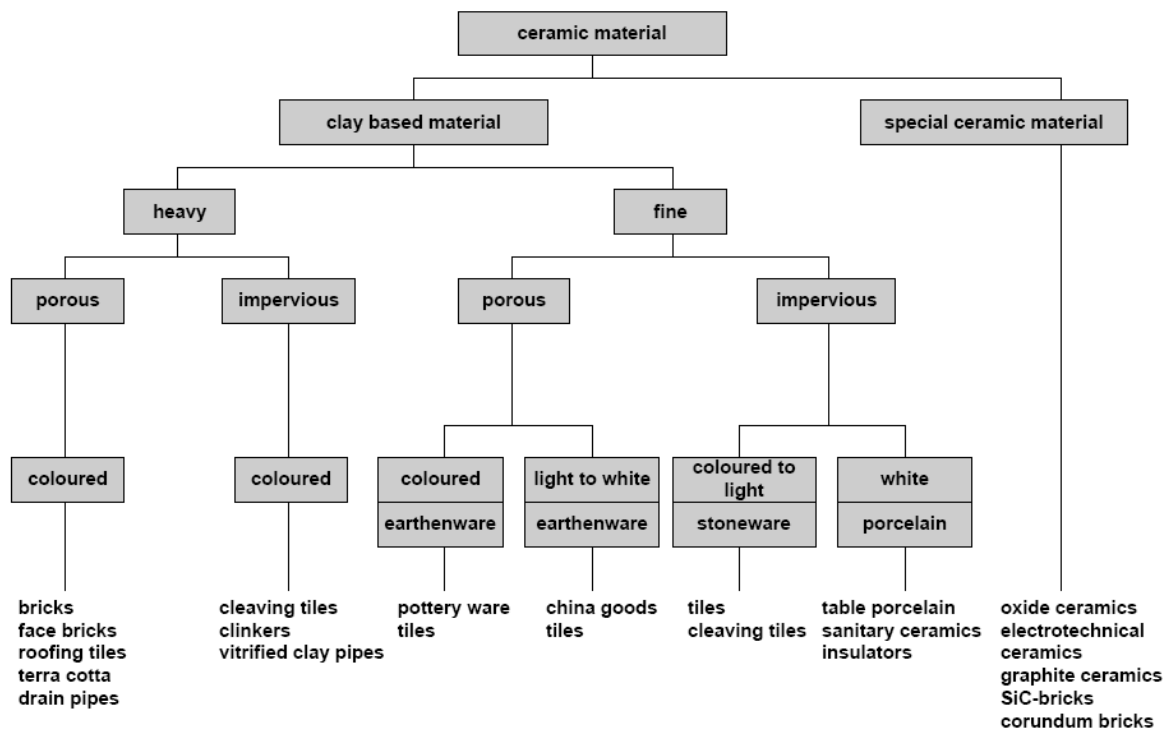
Figure 1.1: Classification of ceramic materials [4].

Figure 1.2: Vitrified clay pipes [5].

- **Chinaware**: It is a vitreous ceramic ware of zero or low absorption after firing that is used for non-technical applications. Chinaware has some applications include art-ware, ovenware, sanitary ware (Fig. 1.3), and tableware.

- **Porcelain**: Can be defined as glazed or unglazed vitreous ceramic ware. Porcelain is used primarily for technical purposes. Figure 1.4 shows some applica-

Figure 1.3: Sanitary ware [6].

tions of porcelain which also include artware, ball mill balls, ball mill liners, chemicalware, insulators, and tableware.

Figure 1.4: Porcelain [7].

- **Technical ceramics**: It includes vitreous ceramic whiteware which used in electrical insulation and electronic pieces production. This technical ceramics supply elements for the aerospace and automotive industries (engine parts, catalyst carriers), biomedical products [8] (bone replacement) as shown in Fig. 1.5 and many other applications.

(a)Biomedical implants

(b) Fixed partial denture, or "bridge"
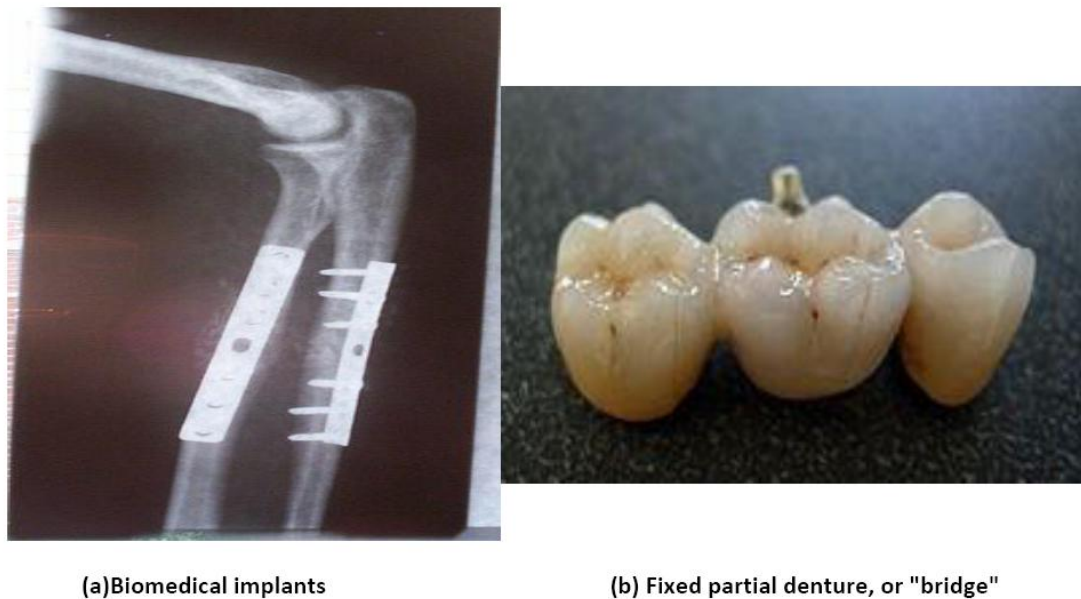
Figure 1.5: Technical ceramics products (a)Biomedical implants (b) Fixed partial denture, or "bridge" [8].

Ceramic products made from highly refined natural or synthetic compositions and designed to have special properties. Advanced ceramics can be classified according to its application as electrical, magnetic, optical, chemical, thermal, mechanical, biological, and nuclear. Most ceramic products are clay-based and are made from single clay or more clay mixed with mineral modifiers such as quartz and feldspar. The types of commercial clays used for ceramics are primarily kaolin and ball clay.

1.2.2 Ceramic production stages

Production of ceramic products has main steps which are largely independent of the materials used and the type of final product. Figure 1.6 schematically shows the typical process and possible or necessary supply and disposal facilities. The process consists of the following steps: mining of raw material, transportation and storage of raw material, preparation of raw material, shaping, drying, surface treatment, firing, and subsequent treatment [9].

1.2.3 Firing process in ceramic production

One of the most important stages in ceramic production is the firing process which could be called as sintering process. Firing process controls many properties of the final ceramic products such dimensional stability, mechanical strength, fire resistance, resistance to water and chemicals, and abrasion resistance. There are a lot of parameters which affect the firing process including temperature, pressure, time, and the surrounding atmosphere. The firing process is thermally activated and depends upon the temperature level and upon the time of holding of the solid material at this temperature. The effect of firing time appears in the structure of ceramic products. Using conventional methods, a short firing time produces porous and low density products while long firing times
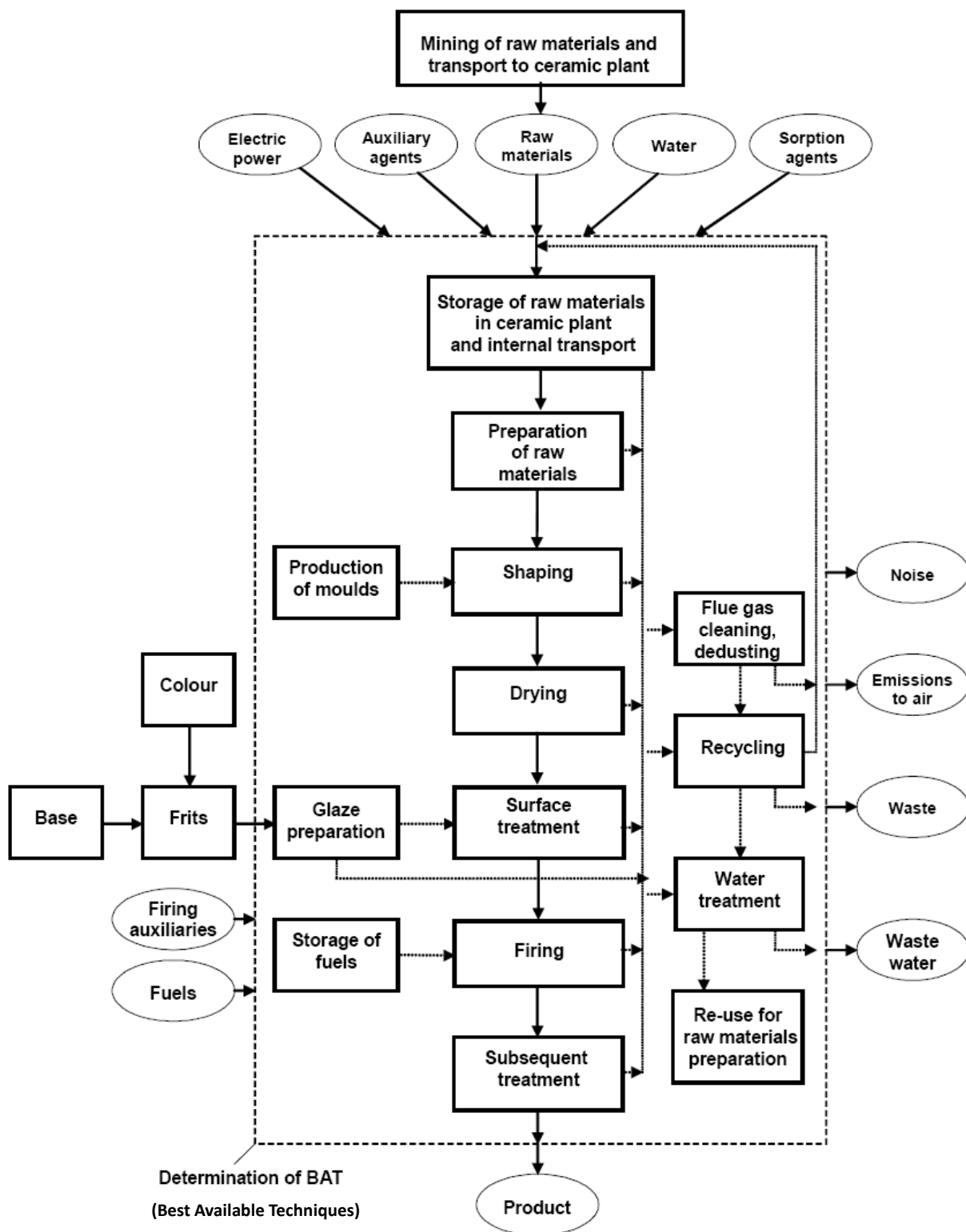
Figure 1.6: Schematic diagram represents ceramic production stages [9].

produces a coarse-grained product.

Often two methods are used in firing, conventional firing and pressure firing. The following paragraph concentrates on conventional firing, because it is most widely used

method.

In **conventional firing**, the green ceramic is heated up to approximately two-thirds of the melting point of the material at ambient pressure and holding it for a specified time in the kiln [3]. Various fuels are used to obtain the temperatures necessary for the firing process in conventional firing, natural gas and oil are the most popular. In addition, solid fuels, biogas/biomass, and electric power are also used for heat generation in some cases. However, most of modern kilns now use natural gas because it is cleaner, efficient, and easy to control during firing process. Natural gas and electric heating can be fitted, adjusted, and controlled by computerized program during the firing process [3]. Typically, gas and electric kilns are common for smaller scale production. Several methods are used for the firing process including pressure firing, plasma firing, microwave firing, hot forging, and infrared firing in addition to conventional firing. Due to higher cost of pressure firing, it is usually reserved for manufacturing ceramics that are difficult to fire to high density with conventional firing. Figure 1.7 shows the industrial maturing temperatures ranges for different product groups.
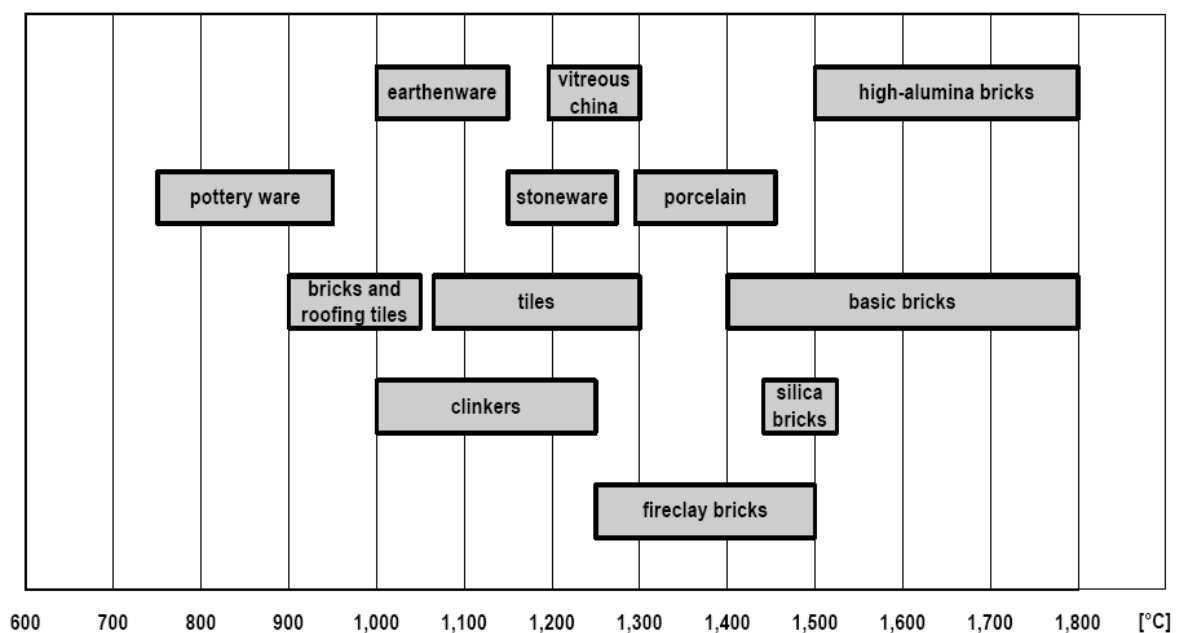
Figure 1.7: Firing temperature for different ceramic products [4].

1.3 Tunnel kiln

1.3.1 Introduction

Tunnel kiln is one of the basic continuously operated kilns in the firing process. Tunnel kiln is a long structure in which only the central portion is directly heated. The ware enters the kiln and is slowly transported through it, and then the temperature of ware is increased steadily as it approaches the central of the kiln which considered as the highest temperature section of the kiln. The temperature is reduced until the products exit the

kiln near room temperature. Tunnel kilns are considered as the most energy-efficient kilns because the heat given off during cooling part is used for all previous drying processes. Figure 1.8 shows a schematic diagram of the tunnel kiln. The different parts of the kiln, the charging, and discharging track are labeled. The figure additionally shows the flue gas passage and the stack which withdraw the flue gas.
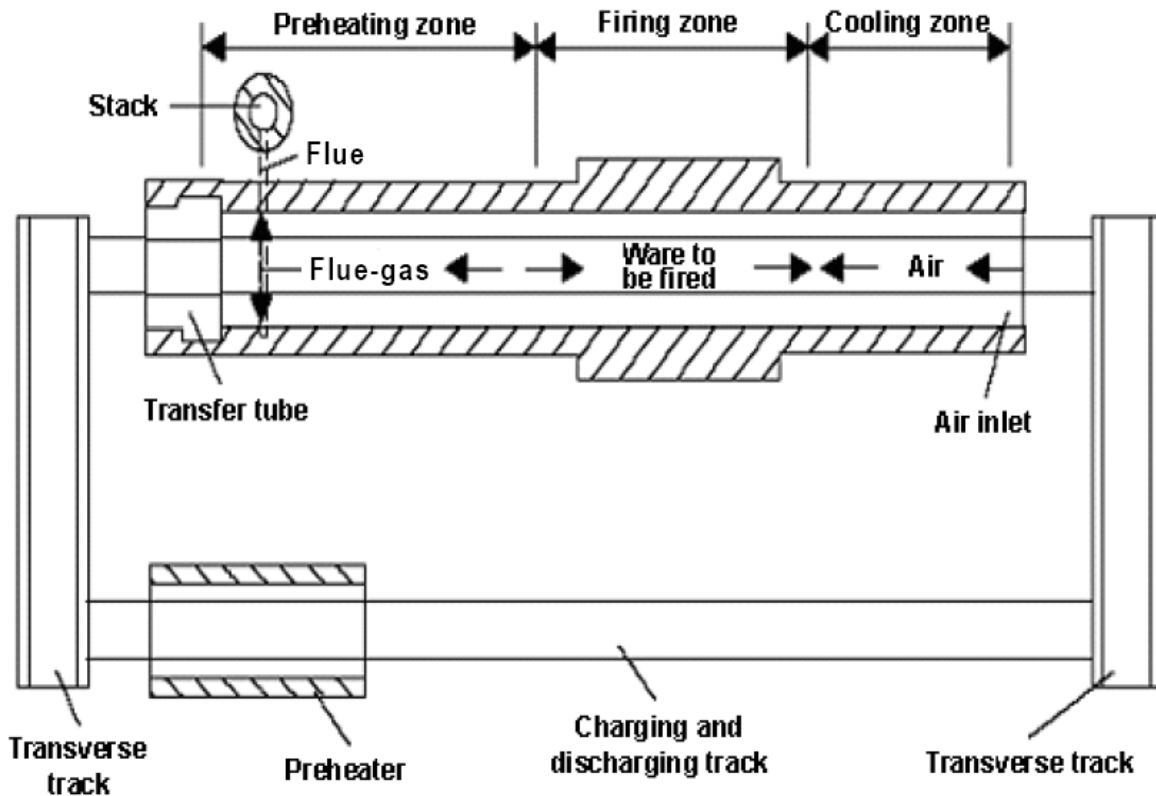
Figure 1.8: Schematic description of tunnel kiln layout [9].

1.3.2 Tunnel kiln history

The history of tunnel kiln design can be traced back to the early 20thcentury since then the design has been continuously enhanced to increase its productivity, product efficiency, and quality. Optimization of the size of kilns, capacity, and rate of firing are still in progress, as shown in Fig. 1.9, photo taken at KERAMAG Company. Tunnel kilns, are a type of modern kilns which look like a tunnel. They are about (90-130 m) long, (3-4.25 m) wide, and (2.4-3.6 m) high (inside dimension), in some cases kilns180 m long have been built. Tunnel kiln design has two schools: **Firstly** the American designs, or traditional design. These kilns are narrower, taller, and the burners placed in the kiln sidewalls, firing toward the center. **Secondly** the European designs in which kilns are generally lower and wider than the American design, the burners are located in the kiln roof and firing straight downward [10].

In the middle of 20thcentury, the tunnel kiln replaced other types of old kilns and became the most popular kiln at the beginning of the 20thcentury. The constructions and insulation materials of old tunnel kilns were commonly from refractory bricks as shown in Fig. 1.10.The figure shows the kiln car with wares and also shows the fire in the firing

Figure 1.9: Old tunnel kiln (this photo had been taken at KERAMAG Company).

zone of the kiln. Figure 1.11 shows photo for such new design in which the kiln is opened and has no doors on both sides, photo taken at KERAMAG Company.
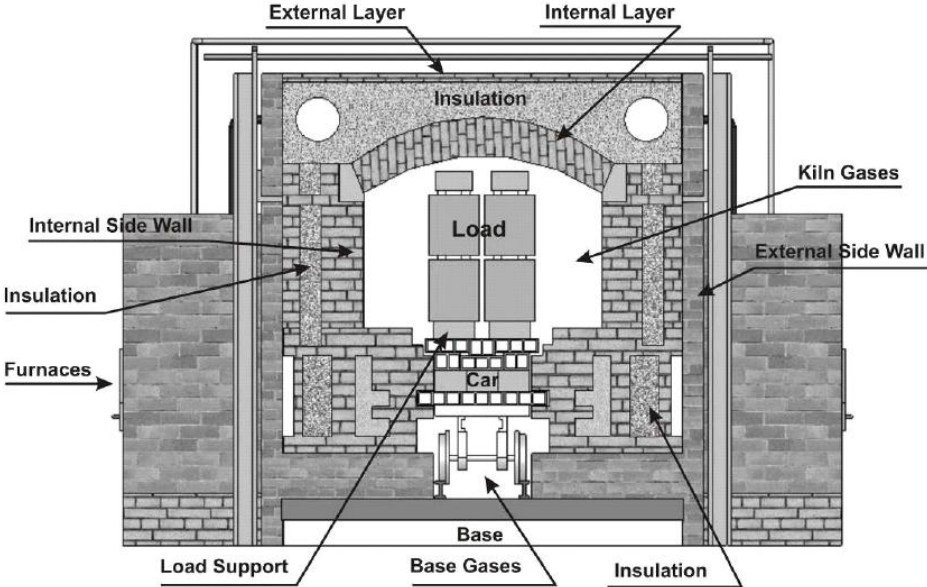
Figure 1.10: Tunnel kiln cross section [11].

Figure 1.11: Tunnel kiln new conception (this photo had been taken at KERAMAG Company).

1.3.3   Tunnel kiln description

Tunnel kiln consists of three main zones; Preheating zone, Firing zone and Cooling zone. The three zones will be described in more details in the following sections.

- **Preheating zone**: This zone considers the first zone in tunnel kiln, whereas the green products enter the kiln on the kiln car. The temperature of these green products increases gradually to a certain temperature due to contact with flue gases which coming from the firing zone, so it could be considered as countercurrent flow heat exchanger.

- **Firing zone**: The firing zone (sometimes it called sintering zone) is the main zone in the kiln, in which the green products are subjected to heat from the combustion of fuel. This zone is responsible of heating up the green products to the desired temperature to produce the products before leaving it. Furthermore, the products go inside the kiln to cooling zone continuously.

- **Cooling zone**: Cooling zone play a main important role in the kiln to cool down the product temperature. Air comes from a blower at the end side of the tunnel kiln playing the function of a countercurrent flow heat exchanger. The cooling process has three main stages; **Rapid cooling**: to avoid the low-valency Fe to be oxidized. **Static cooling**: to avoid cracks in the products. **Final cooling**: to increase the production speed and improve the productivity. After the products go out from the cooling zone all the products have to be removed from the kiln car then the car is prepared for the next cycle of production as shown in Fig. 1.12.

The temperature profile for gas and solid inside the tunnel kiln is shown in Fig. 1.12 [12]. The figure demonstrates the heat exchange between flue gases and solid in the preheating

and firing zone in which the heat from flue gas preheats the solid (green ware); therefore the solid temperature increases and the flue gas temperature decreases. On the other hand, in the cooling zone the cooling air cools the solid coming from firing zone, so that the solid temperature decreases and cooling air temperature increases. Both heat exchange processes are considered as countercurrent flow heat exchanger. As a result to this, the solid on kiln cars moves continuously opposite to direction of all the gas flow.
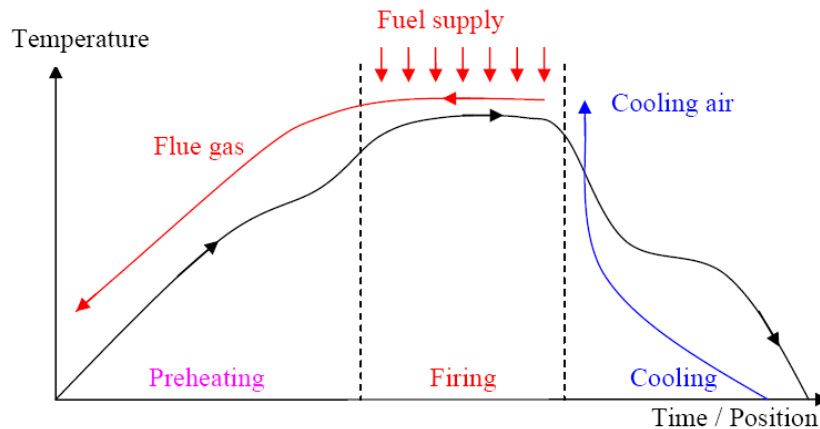
Figure 1.12: Temperature profile of solid and gas for tunnel kiln [12].

1.3.4 Energy consumption

Due to a wide distribution of clay materials throughout Europe, ceramic products and bricks are relatively inexpensive and manufactured virtually in all Member States. A lot of specialized products are mainly produced in a few countries due to its higher price. These countries have the necessary special raw materials, skills, and expertise. For example, a large percentage of ceramic tiles are manufactured in Italy and Spain; tableware in the United Kingdom, Germany, and France; vitrified clay pipes in Germany, United Kingdom, Belgium, and the Netherlands. Ceramic industry has a big importance in terms of employment and economics as shown in table 1.1 [9].

Table 1.1: Ceramics output, sales and employment figure.

Sector of Ceramic industry	EU-15 Output 2000 (x million tonnes)	EU-15 sales 2003 (x million EUR)	Manpower 2003 (x 1000)
Wall and floor tiles	25.0	10100	69
Bricks and roof tiles	55	6800	50
Table- and ornamental ware	0.5	2000	48
Refractory products	4.5	3100	18
Sanitaryware	0.5	1900	25
Technical ceramics	0.15	2000	9
Vitrified clay pipes	0.7	300	2
Expanded clay aggregates (2002)	3.0	300	2.5
Inorganic bonded abrasives (2003)	0.04	260	3.1

Energy consumption is a very important part in the production process because ceramic production consumes a large amount of energy. It is therefore necessary to know the amount of energy consumption due to emissions in the flue gas and then for the whole production process. As a result, energy consumption is a crucial factor in the final price of the product. All sectors which used to produce ceramic in industry are energy intensive, as a key part of the process involves drying followed by firing to temperatures of between 800 and 2000 °C. For example, the manufacture of porcelain has CO_2 emissions consume energy between less than 10 to 18% of the total cost. Another example, the manufacture of bricks has an energy cost between 17 and 25% with maximum levels of up to 30%. The following table 1.2 [9] shows the specific energy consumption in the ceramics industry in Europe.

Table 1.2: Specific energy consumption in the ceramics industry in Europe.

Sector	*Unit*	**1980**	**1985**	**1990**	**1995**	**2000**	**2003**
Brick and roof tiles	GJ/t	2.65	2.45	2.19	2.06	2.38	2.31
Wall and floor tiles	GJ/t	11.78	9.16	6.76	5.45	5.74	5.60
Refractory products	GJ/t	4.88	4.96	6.51	4.91	5.41	5.57
Sanitaryware	GJ/t	26.56	24.214	22.27	22.76	20.88	21.87
Vitrified clay pipes	GJ/t			5.75	5.77	6.10	5.23
Table- and ornamentalware	GJ/t			47.56	38.91	43.46	45.18
Technical ceramics	GJ/t					34.72	50.39

1.4   Motivation

Currently, saving energy is a global concern due to the soaring costs of energy. Energy consumption during the production process of any product affects the price of final product. Obtaining accurate numerical information about tunnel kiln allows for optimal development of the kiln. Therefore, the objective of this work is to understand the process inside the kiln. The following points show the main objectives of this work:

- Create a mathematical model to simulate the process inside the kiln; therefore, this will be done by solving simplified equations to predict the temperature profile for both gas and solid material.

- Rigorous numerical calculations are done to study different cases in the kiln. Furthermore, the analytical solution of simple case is compared with the numerical solution.

- Study the convective heat transfer in the kiln for different operating parameters.

- Study the radiative heat transfer in the kiln and its effects on temperature distribution for both gas and solid materials.

- Carry out 3D flow simulation with a commercial CFD program FLUENT 6.3 for pre-heating zone in Sanitaryware kiln to visualize the flow field.

- How the process and energy consumption can be principally influenced.

Chapter 2

Literature Review

2.1 Heat transfer

2.1.1 Convective heat transfer of setting in tunnel kiln

A laboratory model of a section of a tunnel kiln has been built to investigate a correlation to calculate convective heat transfer rates in the firing of refractory by Dugwell and Oakley [13]. A $1/10^{th}$ scale model in which chrome-magnetite blocks have been used to represent the blades of ware set on cars in the kiln. The data was collected from thermocouples located in the air stream, and on the surfaces of the chrome-magnesite blocks to estimate convective heat transfer coefficients on the sides, top, and end surfaces of the blocks. The data were reported in a correlation for heat transfer to rectangular blades of refractory differentiating between top, side, front, and back surfaces as shown in Eq. 2.1.

$$Nu = cRe^b \tag{2.1}$$

Where
b and c are constants which include the dependency on Prandtl number and on setting geometry. Table 2.1 shows the values of b and c for setting pattern number 1.

Table 2.1: Setting pattern 1

face	c	b
Side face	2.119	0.55
Front face	1.584	0.58
Back face	1.800	0.49
Top face	11.883	0.37

The data was reported as correlations for Reynolds number ranged from 11000 to 20000 and Prandtl number close to 0.7. However, the usage indicated that the correlations were valid for Reynolds number up to 10^5, so that they cover the normal range of kiln operations.

Karaush et al. [14] established an experimental study which involves a model unit conducted on heat absorption from the radiating walls of a kiln by the ceramic ware set up on a kiln car. Their results showed that there was an optimal spacing between the

ceramic pieces in the setting above which any further increase in the spacing would not increase the rate of heat absorption by the ware.

Abou-Ziyan [15] made an experimental investigation to explore the effect of brick arrangements on local, average heat transfer and pressure drop of setting composed of rectangular bricks as shown in Fig. 2.1. He provided reliable information for convective heat exchange between air and bricks in order to represent the actual arrangements so that three basic column configurations were valid for extended range of Reynolds number. A laboratory-scale experiment simulating a section of tunnel kiln by scale 1:4
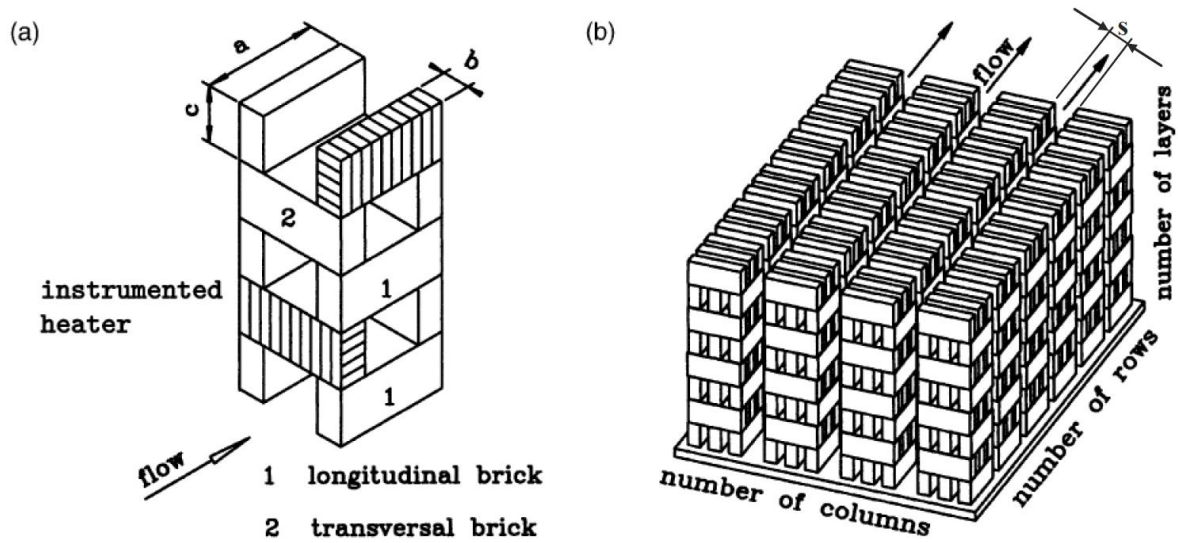
Figure 2.1: (a) Brick directions relative to air flow. (b) Brick arrangement of setting no.1. (c) Section of the duct at AA (four columns and eight layers shown) [15].

was designed and constructed to explore the effect of brick arrangements. He concluded that kilns which used lattice setting with equal spacing between columns and between bricks achieved the largest convection heat transfer coefficient, the shortest production time and provided high measure of energy saving. The following two correlations were reported from his experiments in the form of dimensionless groups, the first equation with correlation coefficient $f = 0.98$ and the second correlation with correlation coefficient of 0.86.

$$Nu = 0.088Re^{0.625}\left(\frac{s}{a}\right)^{-2.30}\left(\epsilon\frac{s}{b}\right)^{1.837} \tag{2.2}$$

$$Nu = 0.081f^{1.31}Re \tag{2.3}$$

Where
a, length of brick model, (m)
b, thickness of brick model, (m)
c, height of brick model, (m)
f, correlation coefficient, (m)
s, spacing between columns, (m), and
ϵ, void fraction.

Where the Nusselt number and the Reynolds number were calculated according to

the following equations

$$Nu = \frac{hD_h}{k} \tag{2.4}$$

$$Re = \frac{UD_h}{\nu} \tag{2.5}$$

Where

h, convective heat transfer coefficient, $(W/(m^2 \cdot K))$

D_h, hydraulic diameter, (m)

k, thermal conductivity of air, (W/(m·K))

U, interstitial velocity of air in the loaded duct (u/ϵ), (m/s)

u, superficial velocity of air in the empty duct, (m/s), and

ν, kinematic viscosity of air, (m^2/s)

Gol'tsova et al. [16] studied experimentally the thermal loss via the enclosing structures of a brick-firing kiln. All zones of the kiln at the Altair Works, which has 48 zones, were investigated from the sides, the top and the data on each zone were recorded. The interpolation method was used to determine the weighted mean temperatures for each kiln zone as shown in Fig. 2.2. The heat loss is based on the temperature fields
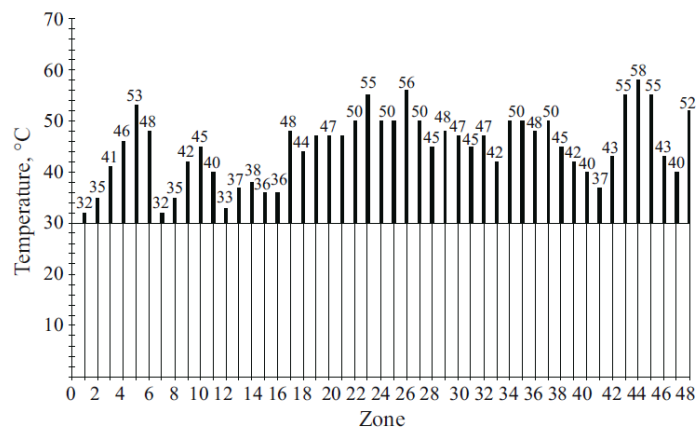
Figure 2.2: Weighted mean temperatures of external kiln walls split by zones: 30°C) theoretical temperature of the external surface of the kiln [16].

of the outer surfaces of the walls and the roof of the firing kiln were equal to 12.1 % instead of 6-8 %, which is considered as the recommended heat loss level meaning up to a 5 % savings in energy consumption. The type of destruction of the enclosing structure of thermal insulation was identified. As a result, it was possible to develop justified recommendations for repairing the kiln lining or thermal insulation. Furthermore, revealing the need for additional thermal insulation in zones with large heat loss even when the lining or thermal insulation were not destroyed.

Vogt and Beckmann [17] evaluated the measurements of Schroder, Hoyer, Abbakumow and Dugwell, generalized equations for the convective heat transfer in channels and extensions of brick settings as shown in Fig 2.3. The influence of the setting geometry was calculated with a factor (Φ) which used to describe the ratio of the Nusselt number of the respective setting arrangement to the fully developed steady pipe flow. Regarding the heat transfer in the channel, the influences of the non-dimensional channel length G_1

and the non-dimensional length of the extension G_2 were proved to be roughly equivalent. In addition, they deduced that in the extension itself the influence of the non-dimensional channel length was forced back strongly compared to the influence of the non-dimensional length of the extension and the area ratio G_3. Furthermore, a maximum in the heat transfer occurred in the extension at $G_2 = 0.9$. The heat transfer values attained in the results were only reached approximately again above a non-dimensional length of the extension of $G_2 > 2.5$.

Where
G, the geometrical similarity index
$G_1 = l_k/d_{GL}$, (channel length/equivelent diameter)
$G_2 = l_E/d_{GL}$, (extension length/equivelent diameter), and
G_3, area ratio.
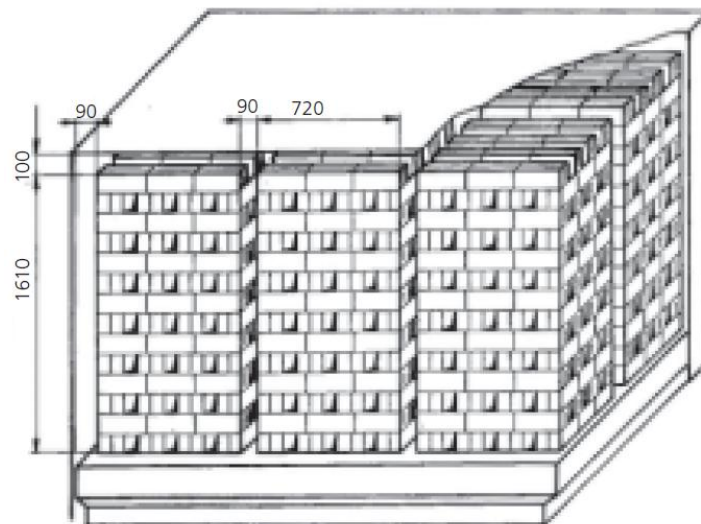
Figure 2.3: Multi-layer lattice-shaped block setting [17].

2.1.2 Numerical and analytical studies

Mandhani et al. [18] investigated, numerically, the forced convective heat transfer characteristics for an incompressible, steady, and Newtonian fluid flow over a bundle of circular cylinders. In the study the role of the type of thermal boundary conditions, namely constant temperature and constant heat flux, on overall heat transfer characteristics were elucidated. The finite difference based numerical solution procedure was used to solve momentum and energy equations for a range of physical and kinematic conditions. Moreover, results on the temperature fields, and on the variation of the Nusselt number on the surface of a typical cylinder in the assemblage were obtained for two values of Prandtl number (air and water) with Reynolds number of flow varied from 1 to 500. The results showed that the surface averaged value of Nusselt number increases with the decreasing value of porosity and increasing values of Prandtl and Reynolds numbers. In addition, the results were in satisfactory agreement with the previous numerical and experimental results for a single cylinder and for the arrays of cylinders

in the overlapping ranges of conditions. The study clearly showed that the cell models offer a viable approach to the modeling of momentum, heat and mass transfer in such multi-cylinder systems.

Kang and Rong [19] used a hybrid method based on numerical simulation and analytical equations to calculate the radiation, convection, and conduction heat transfers in heat treatment processes. The view factors between the furnace and workpieces, among workpieces were calculated by the exposed surface area over the total surface area in the radiation model as shown in Fig. 2.4. In case of conduction model the workpieces
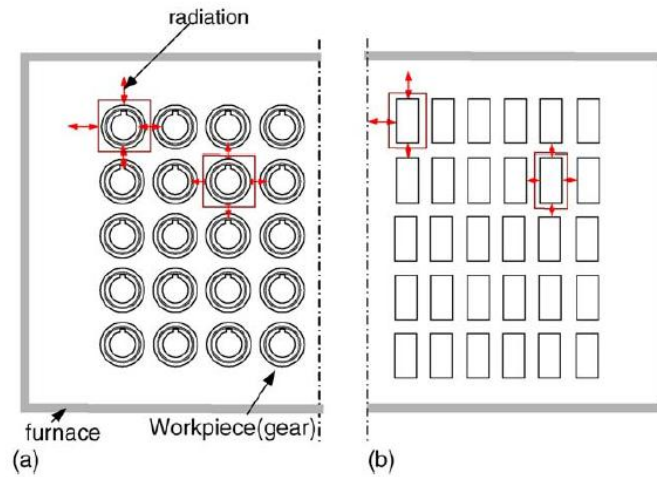
Figure 2.4: The 2D illustrative diagram of view factor calculation between furnace and workpiece and among workpieces: (a) round workpieces; (b) rectangular workpieces [19].

were classified into lumped capacitance and massive objects. In addition the workpieces were classified into three basic shapes: sphere, cylinder, and sheet. Furthermore, natural and forced convection were solved by analytical algorithms for aligned and staggered load patterns. In their calculations the convective heat transfer coefficient and Reynolds number were calculated as follow:

$$h_{conv} = \frac{\lambda_g Nu_{L^*}}{L^*} \tag{2.6}$$

$$Re_{L^*} = \frac{U_\infty L^*}{\nu} \tag{2.7}$$

Where
h_{conv}, convective heat transfer coefficient,
L^*, the characteristic length of workpiece, ($L^* = A^{1/2}$)
A, the external surface area of the workpiece,
Nu_{L^*}, Nusselt number related to the geometrical features of workpiece, and
Re_{L^*}, Reynolds number.

The velocity which was used to calculate Reynolds number was calculated as

$$U_\infty = \frac{\frac{\pi}{4} D^2{}_{fan} H_{fan} R_{fan}}{A_{ws}} \tag{2.8}$$

Where

$D_{fan}, H_{fan}, R_{fan}$ were the diameter, height, and rotational speed of the circulation fan respectively, and

A_{ws}, load area which facing the flow direction of atmospheric gas.

A comparison between the models and two experimental case studies of blades and drill bits has been done as shown in Fig. 2.5.
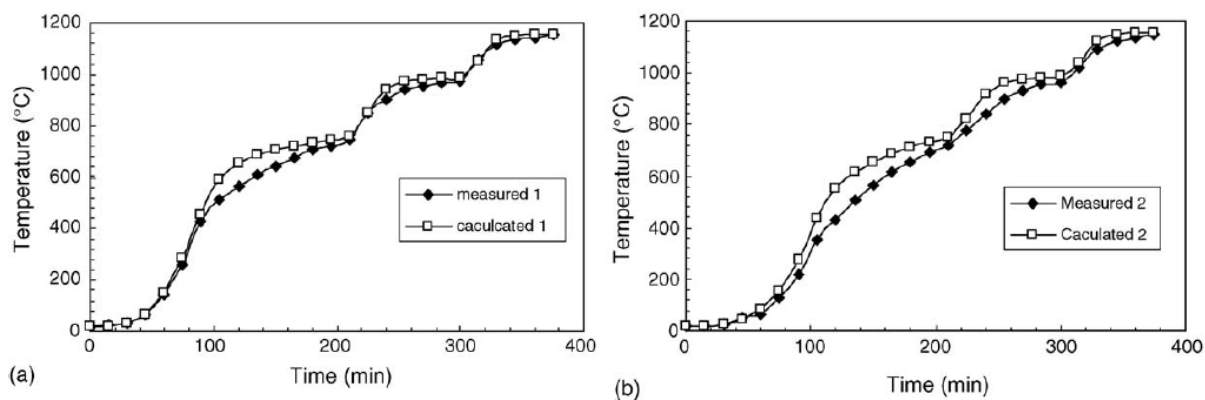
Figure 2.5: Comparison of measured and calculated results of heating of blades:(a) workpiece at location 1; (b) workpiece at location 2 [19].

Becker et al. [20] investigated the convective heat transfer under superimposed longitudinal and cross flow conditions in a fast firing tunnel kiln for glost firing of porcelain. A commercial CFD-code for the simulation is used as shown in Fig. 2.6. Due to complexity of the geometry and the resulting huge number of cells for the simulation, all three segments of the flow model were not simulated at once. In addition, a 1:5 cold model of a real existing tunnel kiln for firing flat tableware was used in order to determine the convective heat transfer coefficient by similarity examinations, in which Reynolds numbers for longitudinal flow (Re_L) and for cross flow (Re_Q) were calculated according to the following equations.

$$Re_L = \frac{w_L d_T}{\nu} \tag{2.9}$$

$$Re_Q = \frac{w_Q d_T}{\nu} \tag{2.10}$$

Where
d_T, plate diameter
w_L, velocity inside the empty canal
w_Q, velocity of the injection, and
ν, kinematic viscosity

Stirrer vessel flow conditions were assumed to calculate the combustion gas temperatures. The total heat transmission coefficient under inclusion of the radiant heat portion was calculated, the kiln room temperature and energy demand of the tunnel kiln plant. Furthermore, a satisfactory compliance between the CFD results and total energy

demand measurements was made on a real kiln plant.
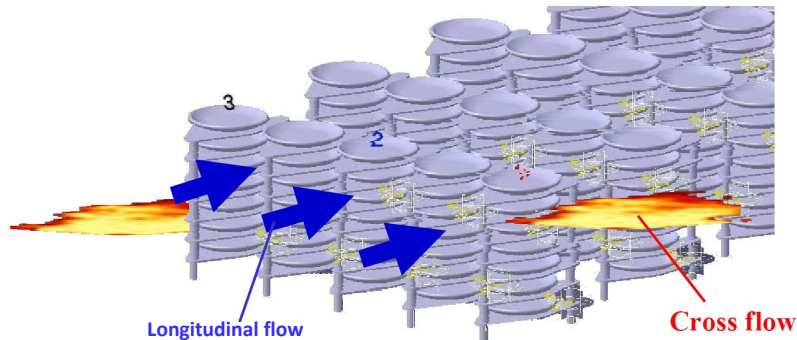
Figure 2.6: The heated model plates are placed at different positions inside the stack to determine the heat transfer coefficients [20].

2.2   Mathematical models for tunnel kiln

Abbakumov [21] analyzed the heating and cooling of products in tunnel kilns and developed relationships which permit accurate thermal analysis of tunnel kilns. Moreover, he analyzed the thermal work of a high temperature tunnel kiln and explained the essential role of radiation. Figure 2.7 shows the temperature distribution for solid and gas according to Abbakumov results. Abbakumov simplified the analysis to examine the counterflow of the setting of endless plates; heat transfer at the ends of the setting, the proportion of which was comparatively small. He introduced appropriate corrections into the coefficient of heat exchange of the longitudinal side surfaces of the columns. Furthermore the system was solved for the case of symmetrical heating (cooling) of the plates.

Dugwell and Oakley [22] made a mathematical model for a firing refractory ware in gas-fired tunnel kilns which can be used to predict gas temperature and composition and ware temperature profiles during firing. The cross section of the studied tunnel kiln is shown in Fig. 2.8. This mathematical model was supported by new correlations for convective heat transfer coefficients on a laboratory scale model. Three models were produced. First, the simplest 1-D model to provide quick prediction of gas and ware temperature profiles. Second, a 2-D model for good prediction of gas temperature profile and improve prediction of ware temperature profile. Finally, a 3-D model to predict ware temperature distribution along the firing zone.

Boming Yu [23] developed a dynamic model of a tunnel kiln consisted of five blades of wares set on a refractory lined kiln car. The model based on the transient heat conduction which occurred in the products (or wares) and in the lining bricks of kiln cars (LBKC), as well as on the gas continuity, heat balance, and material balance equations. Boming performed a numerical simulation on a 72-m-long tunnel kiln which used for firing clay bricks. Furthermore, the numerical results showed that the proposed dynamic model could predict the temperature distributions in both wares and LBKC. In addition, the proposed model could predict the fuel consumption, heat loss, heat storage, and heat

Figure 2.7: Change in temperature of material and gases in a high temperature tunnel kiln; x calculated temperature of gases; o) calculated temperature of material; a) heating of column; b) cooling of column (figures on the curves show the number of the position). Zones: 1) heating; 2) firing; 3) cooling. [21]
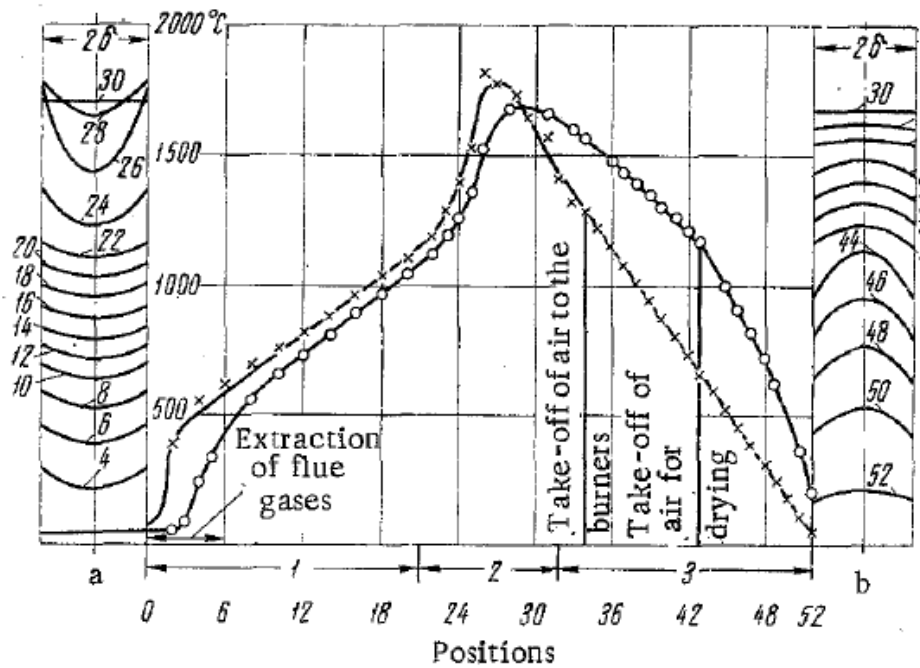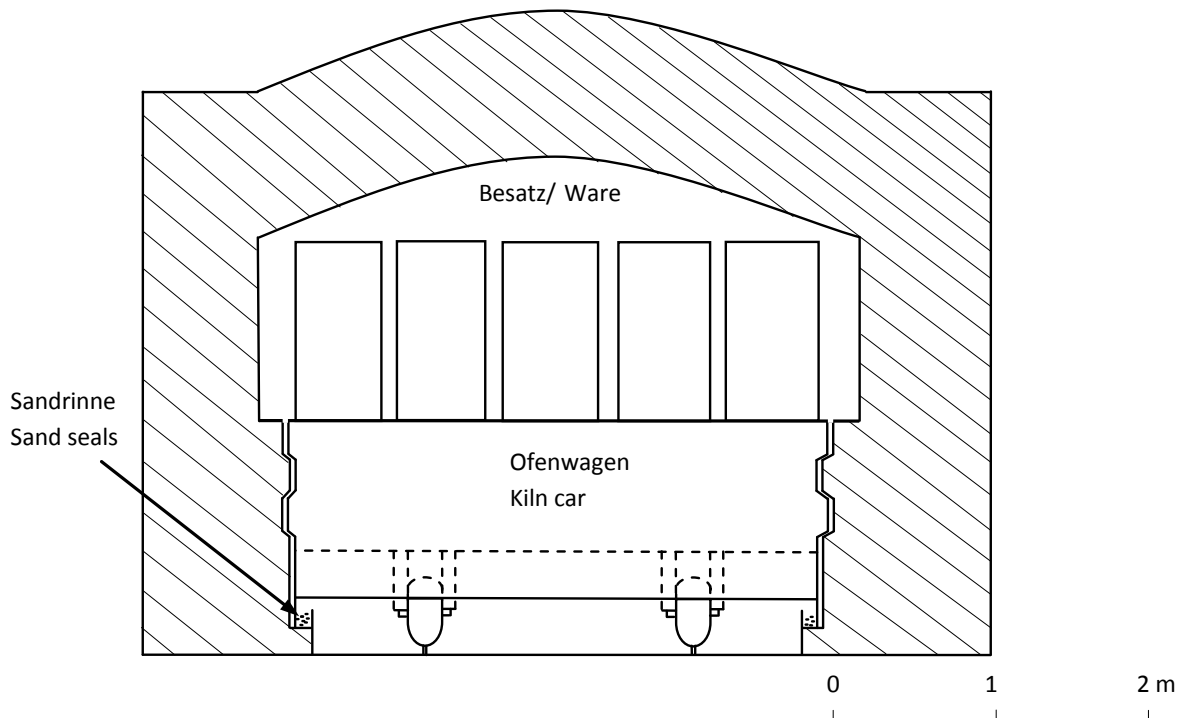

Figure 2.8: Cross section view of kiln and kiln car. [22]

storage rates in both ware and lining bricks as well as in metal parts of kiln cars, gas flow, and exhaust components. Moreover, from simulations two types of energy-saving structures of kiln cars were suggested. Boming also concluded that his dynamic model can be used not only to describe the thermodynamic processes, but also to help design a tunnel kiln and to compute heat balances.

Essenhigh [24] introduced an analysis of tunnel kiln performance to determine the relation between input energy (H_f) and useful output energy (H_s). He applied the integral energy equation which leads to a firing equation of standard form. Essenhigh developed an analytical structure specifically for the tunnel kiln represented as a firing section flanked by two (upstream and downstream) heat exchanger. However, the general design and theoretical structure has potentially wider application, particularly with respect to the influence of heat exchangers in a furnace system. He concluded that these assumptions and constraints were important factors to be identified in extension to other systems. Furthermore, there was generally a governing temperature requirement and time-held at that temperature for the processing to go to completion for the material being heat-treated, such as firing brick, ceramics or heat treatment of steel parts. Then, materials could be cooled and the enthalpy could be recovered, but the determining temperatures and processing times which translated into thus specifying the throughput rates, were set by the internal process requirements.

An approach to determine the temperature fields in tunnel kiln for brick production together with different possibilities of decreasing specific fuel consumption were investigated by Durakovic and Delalic [25]. They developed a software to execute a simulation of temperature distribution in furnace during brick production process in real conditions.

Gol'tsova et al. [26] examined a mathematical model that could be used to maintain the process parameters in real time as a function of the amount of brick manufactured. In the model, they divided the entire kiln into 48 zones equal processing zones. In addition, they assumed that the temperature in each zone was constant, i.e., was not a function of time. The results of the mathematical model were compared with a tunnel kiln from Altair Ceramics Co. (Izhevsk). Furthermore, the results of the kiln operating conditions founded that the rhythm and operating conditions of the kiln vary up to 10 times each month, which affected the quality of the bricks. Moreover, the results showed a large excessive of power consumption. Although, the analysis of operation of the factory showed the annual volume and product assortment were very similar. Comparison between the factory results and their mathematical model results is shown in Fig. 2.9.

Mancuhan et al. [27] developed a one dimensional model to simulate the drying bricks in the preheating zone of a tunnel kiln. Two different profiles and vent locations for the ambient air into the preheating zone were used to achieve the desired gas temperature for high quality bricks. The simulated results were compared to measured plant data. Figure 2.10 showed a comparison between the obtained results and a measured data.
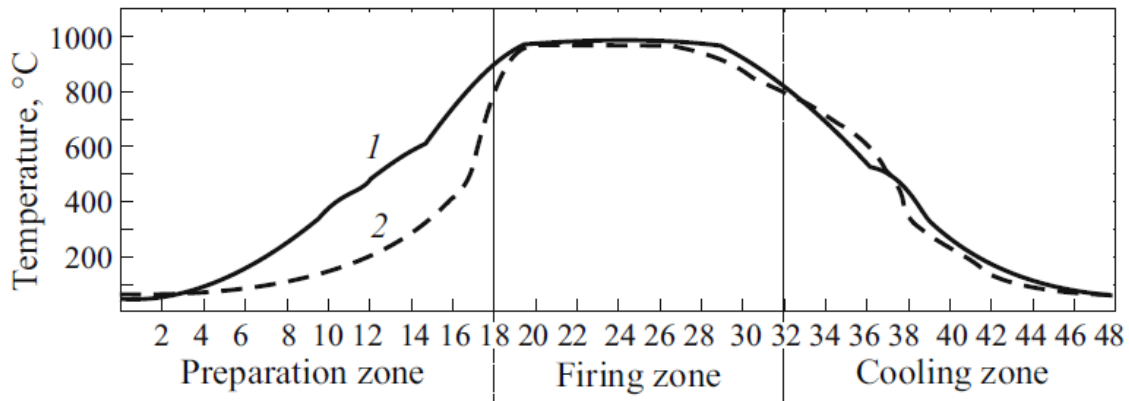
Figure 2.9: Tunnel kiln temperature conditions: for the process (1: operational) and real (2: production). [26]
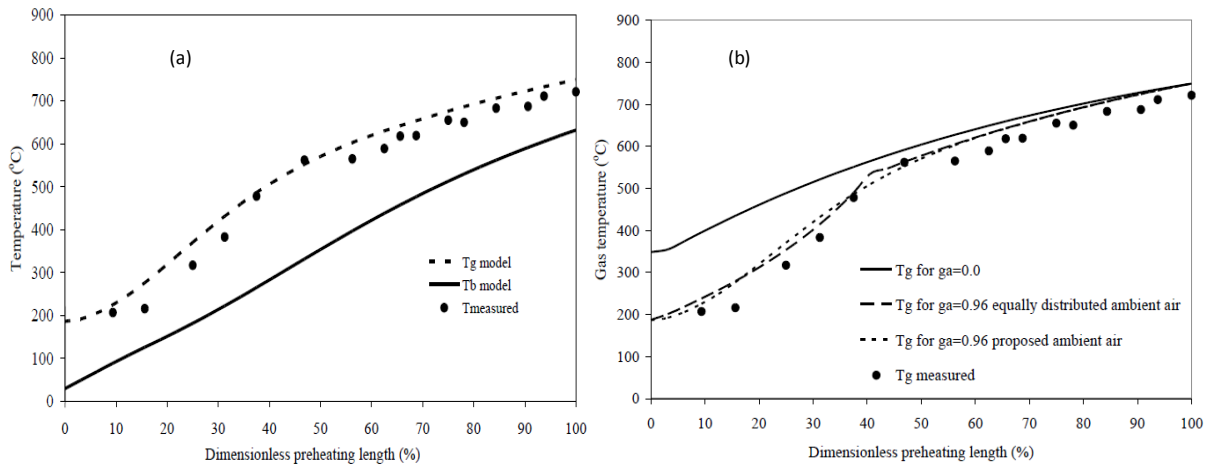
Figure 2.10: (a) Comparison of the measured temperatures to the computed gas and brick temperatures, (b) Variation of kiln gas temperature profiles as a function of different mass fluxes of ambient air. [27]

2.3 Mathematical models for burning zone

Shvartsman et al. [28] deduced an equation for assessing the uniformity of firing over the length of the setting in tunnel kiln. The results showed that, to reduce the firing irregularity over the setting's length it was necessary to reduce the distance between the burners, reduce the heat losses into the surroundings, and increase the total volume of combustion products by using only hot air. The result declared that with reduction in the distance between the burners and increasing in the volume of combustion products, it was possible to obtain fuel economies. They concluded, it was best to use tunnel kiln equipped with roof burners with continuous movement of the goods to increase the uniformity of firing. The uniform heating of the entire volume of the setting on the tunnel kiln car reduced the firing time and as a result, the output of the kiln was increased and also the specific outlay on fuel was reduced.

Mancuhan and Kucukada [29] presented an optimization of the fuel and air used around a tunnel kiln producing bricks with low calorific value (LCV) coal as an additive. In the model, the mass and energy balance computations to calculate the energy were computed based on the plant data. They concluded that the use of admixed coal for both cases which using pulverized coal or natural gas (NG) in firing zone is considered as an advantage. Furthermore, the heating value of the admixed coal (AC) didn't significantly change the total fuel cost when pulverized coal was preferred. They recommended the high calorific value (HCV) of admixed coal when the plant use natural gas as the fuel supplied to the firing zone as shown in Fig. 2.11[1]. In addition, although the natural gas
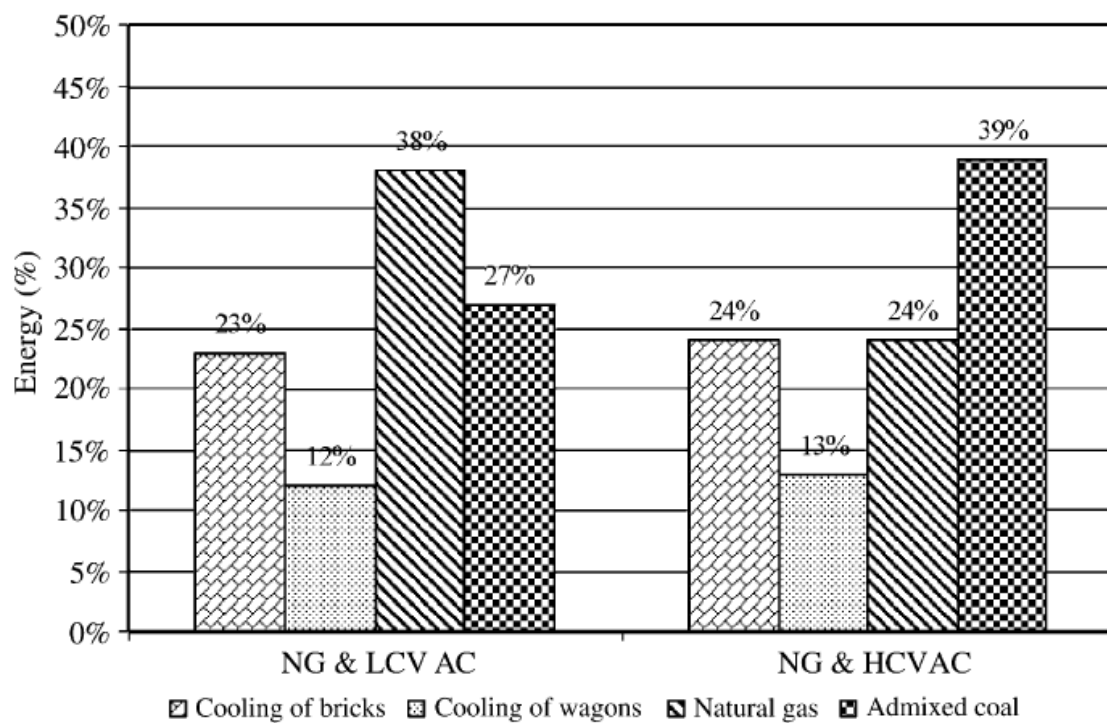
Figure 2.11: Percentages of the energy sources for the tunnel kiln when NG and AC are used [29].

is more expensive than the pulverized coal, it eases the combustion. Their optimization results may change depending on the properties of fuels and its prices.

Kaya et al. [30] made an optimization of the firing zone to minimize the fuel cost as being the objective function. In the work, they demonstrated how the optimal operating conditions could be predicted by using a mathematical model representing in the simplest form the phenomena of heat transfer, combustion of admixed coal (AC) and pulverized coal (PC), together with gas flow. The fuel cost is used as an objective function with the necessary constraints. The optimization was realized by considering the tunnel kiln to be composed of number of increments. The optimized value of PC was found to be lower than the existing tunnel kiln. The optimization results were compared to the plant data of brick kiln as shown in Fig 2.12.The overall energy balance predicted an energy use of 3385 kJ/kg of brick, which was 2.7 % higher than the optimized results.

---

[1]This figure is used based on license agreement between the author and Elsevier with license number of 2950900525607.
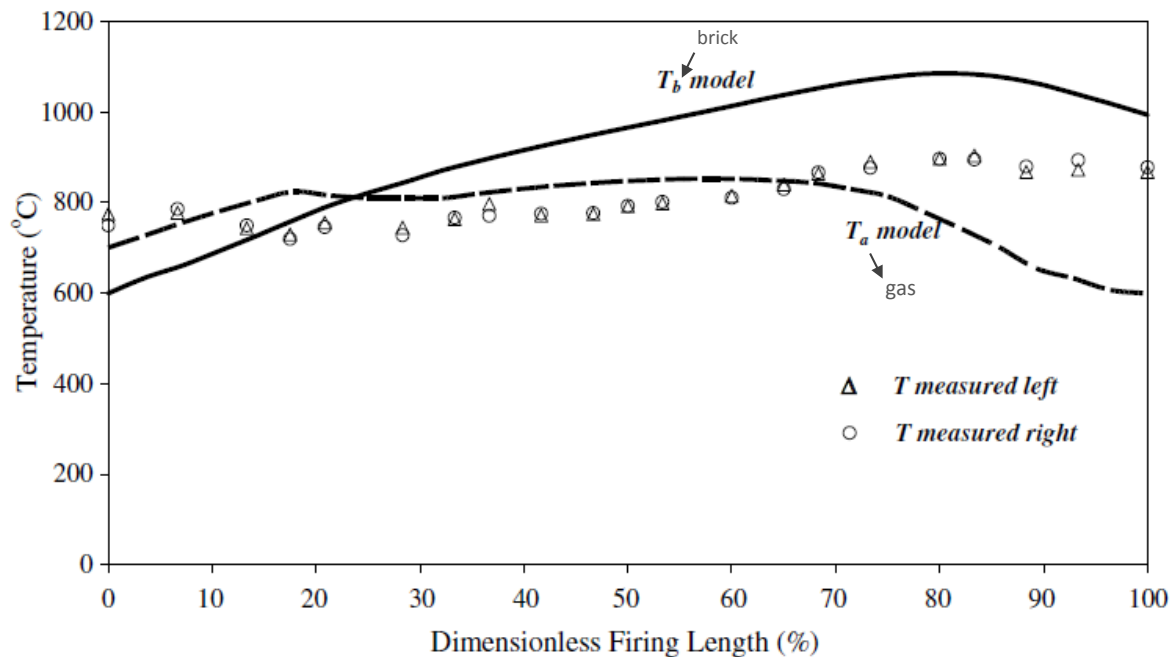
Figure 2.12: Comparison of the measured temperatures to the computed gas and brick temperatures [30].

2.4 Numerical simulation for tunnel kiln

Numerical simulation of the thermal process inside a ceramic frits melting kiln with CFD and a global FORTRAN code were developed by Possamai et al. [31]. The used domain in the analysis was consisted of a rectangular refractory kiln as shown in Fig. 2.13, working in a mean inside temperature of 1400°C. The coupled codes were proved to be a helpful tool in two main aspects. First, by providing good values estimation for different variables which allow easy investigation of the influence of several variables in the process such as kiln geometry, burner position, fuel, and oxidizing type. The second was by providing data for a more complete approach of the problem involving also the structure of the kiln not idealizing it. Improvements could be contributed to several aspects of industrial interest as reduction of material cost on maintenance of the refractory walls, improve productivity, increase of the efficiency of the fusion process, optimization of burner position, and kiln geometry. The comparison of the CFD results with experimental data proved that the mathematical models used in the numerical simulation were consistent in practice. Furthermore, comparison with global results from the FORTRAN code was expected to have even better accuracy with experimental values.

De Paulo Nicolau and Dadam [11] developed a thermal model of a tunnel kiln which allows efficient and less energy consuming design using numerical simulation. The model was used for firing clay tiles, bricks, and similar products with natural gas and sawdust as fuels. The numerical simulation results were compared to measured values. A comparison between the numerical results and experimental results is shown in Fig. 2.14. The amount of reduction in the fuel consumption with an increase in
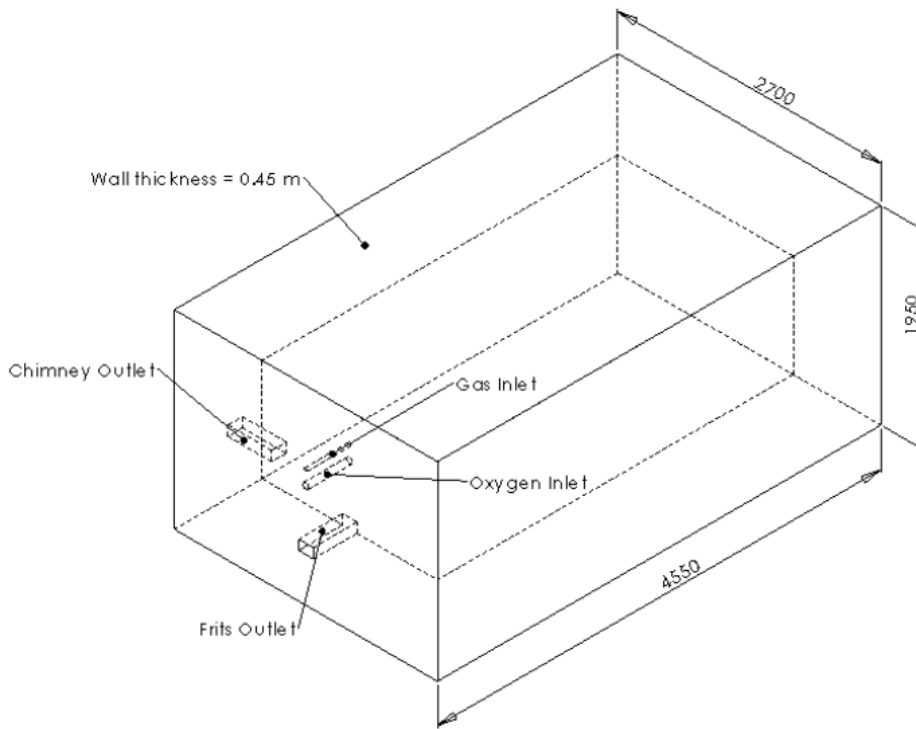
Figure 2.13: Kiln geometry [31].

the thermal insulation thickness used on the walls was determined from results. The results demonstrated the influence of the load internal area on the heat exchanged with combustion gases inside the kiln. Also, it showed the effectiveness of the heat exchange inside the load stacks which occurs above a threshold value for the internal area to external area ratio. Furthermore, the results showed the need to use a larger number of less tortuous channels inside the load to promote efficient gas circulation.
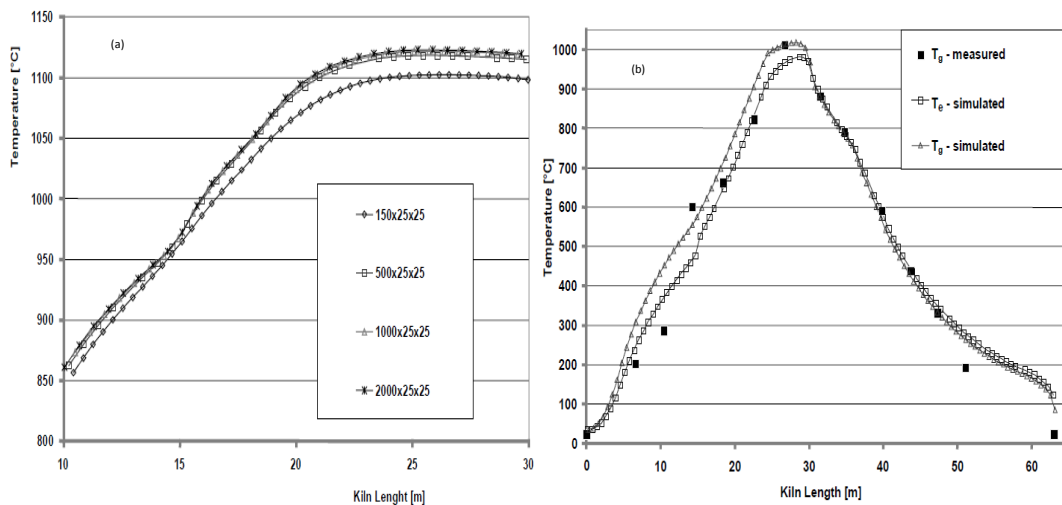
Figure 2.14: (a) Temperature within the load for the central part of the tunnel kiln, (b) Gas temperature compared to simulated temperature of the gas and temperature inside the load [11].

Oba et al. [32] presented a numerical model to simulate a tunnel kiln applied in ceramic industry. The dimensions of the used kiln in calculations is shown in Fig. 2.15, in which the load was one block. The model solved a 3D problem with models for energy distribution in the burning zone, the advection of gases inside the kiln, and the radiation between ceramic load and refractory walls. The energy loss from the kiln to the surroundings was solved. The results presented the characteristic firing curve of the kiln as shown in Fig. 2.16. The results also illustrated the temperature distribution in the load, walls, and gases; additionally, it estimated production and distribution of energy flows in the kiln. Moreover, the results were based in some parameters such as fuel, cooling air flow, and extraction air flow. In addition, the model was capable of estimating the temperature and energy distribution and kiln efficiency. The authors concluded that although the numerical prediction given was consistent, experimental data of the kiln in operation condition was necessary for real validation.
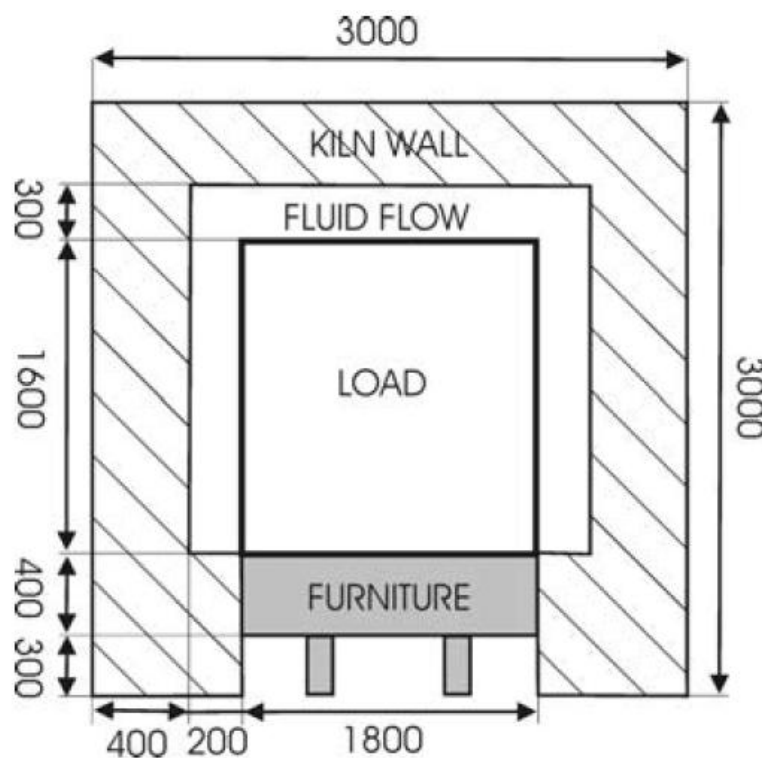
Figure 2.15: Dimensions of the furnace, load and lorry. [32]

2.5 Modeling and control systems for tunnel kiln

Due to requirements of automated tunnel kilns on the basis of microprocessor technology, this makes it possible to reduce the volume of control and measuring instruments and apparatus on the kiln. Furthermore, requirements to increase the accuracy in maintaining temperature conditions by the use of the most up-to-date methods of control.

Abbakumov and Vel'sin [33] developed a mathematical model and a program for
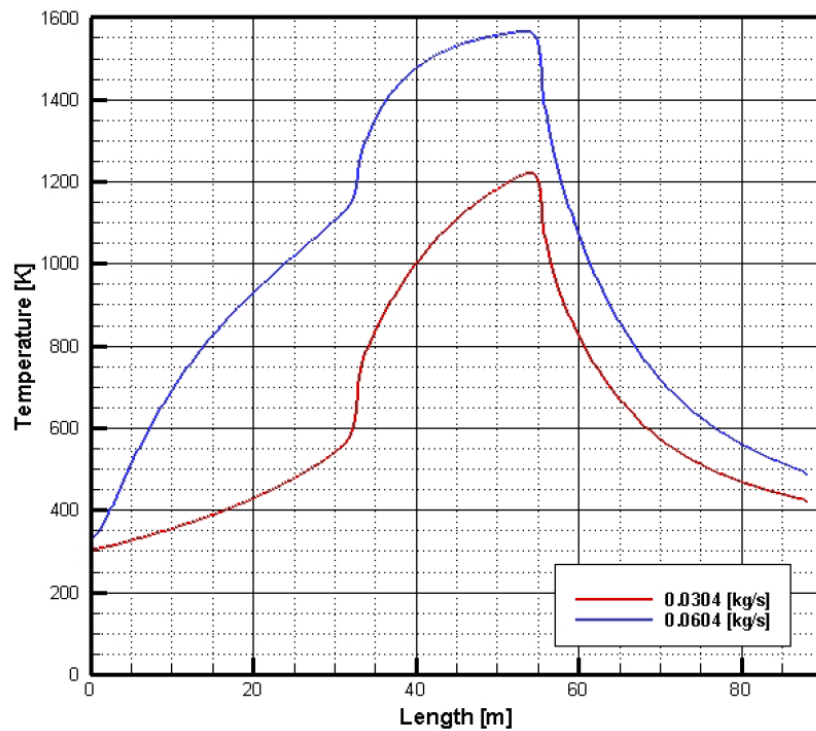
Figure 2.16: Temperature curve of flow inside the kiln. [32]

calculating the firing zone of a tunnel kiln with automatic control of the firing process. The developed program made it possible to select the best method of control and to determine the optimum parameters of the system. The basic advantages and disadvantages were revealed by use of the developed method of control. Their mathematical model may serve as an element of software of an automated system of production operation control of firing in a tunnel kiln.

Chen et al. [34] proposed an intelligent computer-aided design (CAD) system for ceramic kiln. The developed system used an object-oriented programming (OOP) technology with a user friendly interface. In addition, the expert system and the drafting system were discussed in detail. Furthermore, in the integrated intelligent CAD system, the object oriented database was taken as a kernel, the design calculation, the expert system, and the parametric drafting system interfaced directly with the engineering database. The results provided a foundation for the intelligent automatic design of ceramic kilns.

Michael and Manesis [35] proposed a control scheme for model-based coordination of the individual subsystems which were controlled locally by fuzzy controllers combined with conventional ones in brick and tile production tunnel kiln. The proposed control structure could be easily applied to the process environment and the implementation may be realized directly on a programmable logic controller. Furthermore, in the upper level of the hierarchy supervisory controller classified the actual system situation based on the mathematical model of the process and in the lower level performed the specific control mode selection. A result from this study is shown in Fig. 2.17.
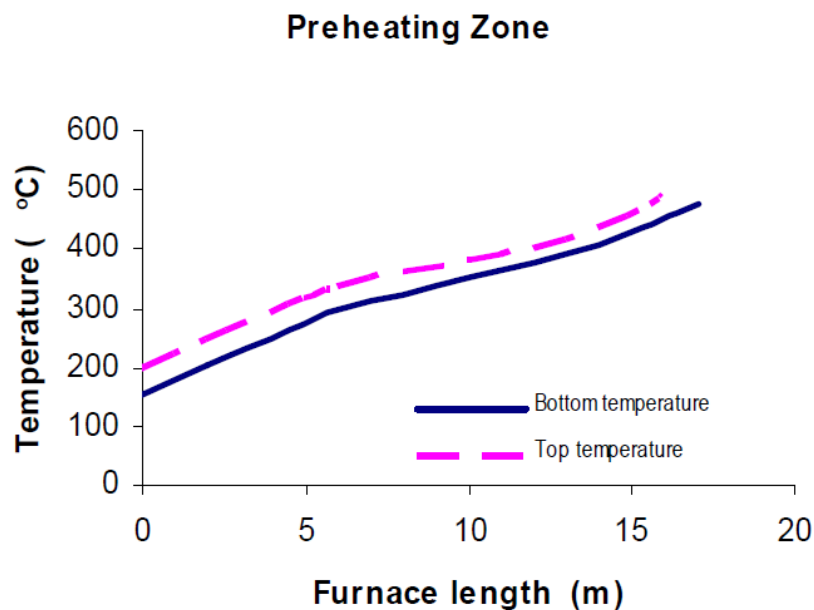
Figure 2.17: Temperature difference after the action of the fuzzy supervisory controller. [35]

2.6   Energy saving in tunnel kiln

Tunnel kiln consumes different amounts of energy. The consumed energy varies according to the type of products; consequently, there is much interest in tunnel kiln energy savings. The following literature focuses on energy saving in tunnel kilns.

The tunnel kiln car's refractory system in the ceramic industry protects the steel chassis and wheel sets from high temperatures. There are two main types of losses for kiln car, transmission losses due to accumulated heat flow via the bottom surface of the tunnel kiln cars and cumulative losses corresponds to the heat content of the kiln cars when they leave the kiln. Therefore, De Wit [36] developed a computer program called Q-CAR for the exact calculation of energy loss in the kiln car (transmission losses and cumulative losses). The developed system reduced energy consumption in cars because kiln cars accounted for about 40 % of the internal surface area of the kiln. The used system is a particularly suitable auxiliary for the selection of tunnel car refractory systems.

Carvalho and Nogueira [37] presented the utilization of dedicated modeling tools for the optimization of a variety of thermal equipment for high- medium- and low-temperature heat transfer processes. The equipment considered for this study was (ceramic and glass-melting furnaces, cement kilns, and baking ovens). A significant reduction of energy consumption and low-cost abatement was achieved for these four industrial situations. The authors believed that the achievements were contributed to pollution abatement strategies for industries that were intensive energy users. The following figure shows different brick settings used in the study.

Unaspekov [38] presented a result on updating the firing technology for aluminosilicate refractory materials in a high-temperature tunnel furnace at the Kazogneupor Plant.
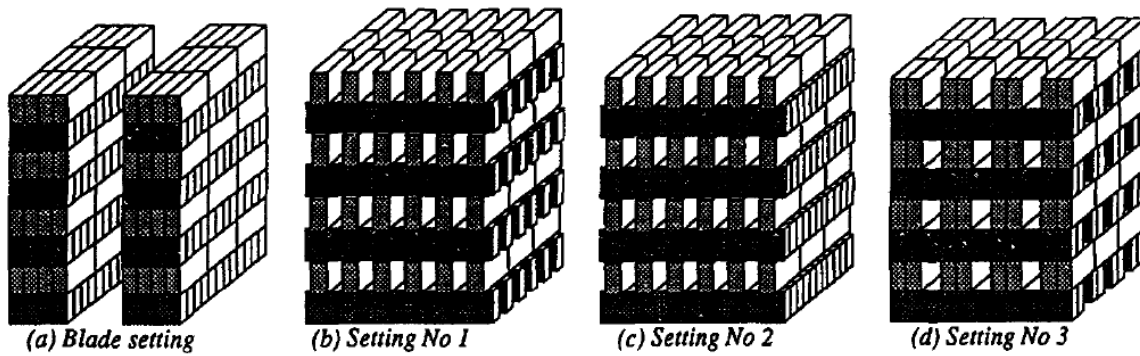
Figure 2.18: Typical brick setting geometry [37].

Unaspekov concluded that the use of the advanced gas heating system provided rational supply and burning of fuel to attain the required firing temperatures. Furthermore, a large amount of work has to be done to optimize the performance of the combined system of heating depending on the gas-dynamic and hydraulic operational parameters of the tunnel furnace. In addition, special concern must be placed on the reduction of heat loss through the refractory lining of high-temperature furnaces.

2.7 Conclusions on literature review

The previous work in the literature review sections of the present chapter, provides guidelines and an extensive background for the present study. The literature survey of the previous work revealed most of the research has been done on tunnel kiln used in brick manufacturing. Some experimental works have been done to investigate the convective heat transfer coefficient and effect of brick settings in brick tunnel kilns. In addition, some works have been done to calculate the radiative heat transfer for some products in tunnel kilns. Mathematical models have also been created to simulate the thermal process in certain tunnel kilns. Literature review revealed that further research in tunnel kilns with other combinations of parameters and consideration of kiln furniture are required.

In spite of many published studies, it still seems possible to develop a model to estimate the temperature profile for gas, products, and kiln furniture. There are a plethora of studies regarding various types of products that are produced in tunnel kilns. Previous models yielded no information regarding changes in the heat transfer coefficient with various kiln geometries. Also, the measured profile doesn't present the whole section. There is a scarce amount of research that is independent of product types. The current work presents a simplified mathematical model for the kiln and studies the effect of burning zone length on the temperature profile for both gases and solids. In addition, examine the heat transfer in the kiln furniture with special supports and geometry. Finally, observe the effect of air addition in the preheating zone. Such studies are crucial in order to fully understand tunnel kiln dynamics.

Chapter 3

Simplified Mathematical Model for Tunnel Kilns

3.1   Introduction

The heat transfer mechanism is complex inside the tunnel kiln, because of the interaction of kiln car, kiln furniture, product types, and product arrangements in the kiln. Therefore, it is important to establish a simplified model to understand the principal behavior of the kiln process. This model considers the preheating and burning zone in which the solid materials (product, furniture, and car) are heated up to the required sintering temperature. The cooling air is sucked away from the kiln and then used in the dryer. It is assumed that the enthalpy of the cooling covers the energy for the drying process. As a consequence, the energy of the fossil fuel of the kiln is the required energy for the total process. This is the case for the most processes of ceramics burning. Therefore, the following is assumed and are valid for counter current heat exchanger.

Assumptions :

⋆ The process is assumed to be a steady state process.

⋆ The temperature of product and of gas is assumed to be constant at any cross section. As a consequence, the temperature depends only on the length.

⋆ The temperature of product and transportation materials are the same.

⋆ The heat transfer coefficient is constant.

⋆ The heat losses through the walls are neglected.

⋆ The material properties (specific heat capacity, density) are assumed as constant.

⋆ The material does not store latent energy.

3.2   Energy balance

The basis of all kiln processes is an energy balance. The enthalpies in heat balances are always referred to the reference temperature (0°C). In energy balance analysis, the energy inserted by fuel is equal to the heat gain by solid, heat removed from gas, and

heat loss through walls. By applying the energy balance, the following equation is obtained

$$\dot{M}_s c_s \left(T_{s,f} - T_{s,in}\right) + \dot{M}_g c_{pg} \left(T_{g,out} - T_a\right) + \dot{Q}_w = \dot{M}_F hu. \tag{3.1}$$

Where $\dot{M}_s$ represents solid mass flow rate, c_s specific heat of solid, $T_{s,in}$ and $T_{s,f}$ represent inlet and outlet solid temperature respectively, $\dot{Q}_w$ heat loss through kiln walls, $\dot{M}_F$ fuel mass flow rate, $\dot{M}_g$ gas mass flow rate, c_{pg} gas specific heat at constant pressure, the inlet gas temperature is T_a (ambient air temperature), and $T_{g,out}$ outlet gas temperature .

In the following, the heat loss through walls is neglected ($\dot{Q}_w = 0$) as mentioned before. Regarding the energy balance equation, the solid material ($\dot{M}_s$) represents the two masses for product ($\dot{M}_{pro}$) and transportation ($\dot{M}_T$) as

$$\dot{M}_s = \dot{M}_{pro} + \dot{M}_T.$$

The ratio between the product materials to the transportation material is defined as

$$X_T = \frac{\dot{M}_T c_T}{\dot{M}_{pro} c_{pro}}.$$

Where c_T specific heat capacity of transportation ($c_T \cong c_s$), c_{pro} specific heat capacity of products.

Therefore, the following equation is obtained

$$\dot{M}_s = \dot{M}_{pro}(1 + X_T \frac{c_{pro}}{c_s}). \tag{3.2}$$

The outlet gas mass flow rate from the combustion process is the summation of the fuel mass flow rate, $\dot{M}_F$, and the air mass flow rate $\dot{M}_a$

$$\dot{M}_g = \dot{M}_F + \dot{M}_a. \tag{3.3}$$

The mass flow rate of air can be expressed in terms of air demand (L), excess air number (λ) and fuel mass flow rate as

$$\dot{M}_a = \lambda L \dot{M}_F. \tag{3.4}$$

Then the gas mass flow rate can be specified directly as a function of fuel mass flow rate, air demand, and excess air number

$$\dot{M}_g = \dot{M}_F \left(1 + \lambda L\right). \tag{3.5}$$

The energy equation Eq. 3.1 requires the mean specific heat capacity. Therefore, the following equation is used to calculate the mean specific heat capacity with gas properties referred to reference temperature, $T_o = 273\,K$ [39]

$$\frac{\bar{c}_{pg}(T)}{c_{po}(T_o)} = \frac{1}{n_c + 1} \left(\frac{(T/T_o)^{n_c+1} - 1}{(T/T_o) - 1}\right). \tag{3.6}$$

For this specified case the specific heat of air with ($c_{po(T_o)}= 1.0$) and index ($n_c= 0.1$) are used. Moreover, equation 3.7 is used to simplify the energy consumption equation

$$c_{pg}(1 + \lambda L) \cong c_{pgo}\lambda L. \tag{3.7}$$

Then, the specific energy consumption equation referred to the solid flow is introduced

$$E_s = \frac{\dot{M}_F hu}{\dot{M}_s}. \tag{3.8}$$

Solving Eq. 3.1 to Eq. 3.8 results in the following form for the specific energy consumption

$$E_s = \frac{c_s \left(T_{s,f} - T_{s,in}\right)}{1 - \dfrac{c_{pg} \left(1 + \lambda L\right) \left(T_{g,out} - T_a\right)}{hu}}. \tag{3.9}$$

In industry the specific energy consumption is referred to the product flow as in the following equation

$$E_{pro} = \frac{\dot{M}_F hu}{\dot{M}_{pro}}. \tag{3.10}$$

Where
E_{pro}, is the specific energy consumption per kg of product.

By joining Eq. 3.2, Eq. 3.10 together with Eq. 3.8 the specific energy consumption per kg of products can be presented as

$$E_{pro} = E_s \left(1 + X_T \frac{c_{pro}}{c_s}\right). \tag{3.11}$$

The specific energy consumption E cannot be calculated because $T_{g,out}$ is not known. The outlet temperature depends on area and heat transfer coefficient. Therefore, the outlet gas temperature is calculated in the following sections for different basic cases. The energy consumption related to the product is therefore always higher than the energy consumption related to the solid.

3.3   Simple analysis case A (firing zone zero)

3.3.1   Description of the case

For this case the burning zone is considered with zero length. Therefore, the two zones are considered as one zone (preheating only) which is called "case A". Figure 3.1 shows a schematic description of the tunnel kiln with a gas input from one position. In the shown figure, the combustion of fuel with air occurred in an adiabatic combustion chamber. Therefore, the outlet gas temperature from this combustion process is the adiabatic flame temperature. As illustrated in the figure, the kiln car carries the product through the kiln in counter direction to gas flow. The kiln process is reduced to a simple counter current heat exchanger.
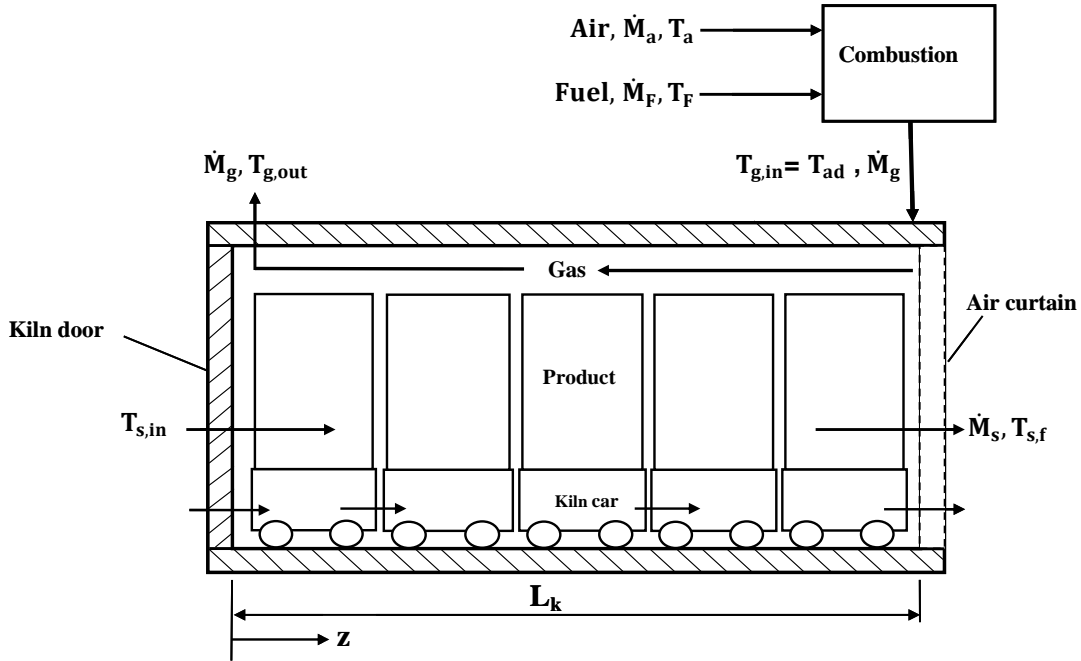
Figure 3.1: Input of gas at one position.

3.3.2 Temperature profile

The temperature profile of the solid and the gas for this heat exchanger can be calculated using an energy balance for a differential kiln length dz. The gas enthalpy flow change $d\dot{H}_g$ and solid enthalpy flow change is expressed as

$$d\dot{H}_g = d\dot{Q}_{conv}, \;\; d\dot{H}_s = d\dot{Q}_{conv}. \tag{3.12}$$

Also the gas enthalpy flow change $d\dot{H}_g$, can be expressed by the following equation:

$$d\dot{H}_g = \dot{M}_g c_{pg} dT_g. \tag{3.13}$$

The convective heat transfer between the gas and solid can be expressed as

$$d\dot{Q}_{conv} = \alpha \left(T_g - T_s \right) dA. \tag{3.14}$$

Where

$$dA = \frac{A_t}{L_k} dz. \tag{3.15}$$

α, heat transfer coefficient,
dA, the element area,
A_t, total surface area of solid, and
L_k, the kiln length.

The following ordinary differential equation (ODE) for gas is obtained

$$\dot{M}_g c_{pg} dT_g = \frac{\alpha A_t}{L_k} \left(T_g - T_s \right) dz. \tag{3.16}$$

The equation can be represented with dimensionless parameters

$$\frac{dT_g}{dZ} = St_g \left(T_g - T_s \right).$$ (3.17)

Where the Stanton number for the gas is expressed as

$$St_g = \frac{\alpha A_t}{\dot{M}_g c_{pg}}.$$ (3.18)

and the dimensionless length coordinate is represented as

$$dZ = \frac{dz}{L_k}.$$ (3.19)

Regarding the solid, the solid enthalpy flow change is expressed by equation

$$d\dot{H}_s = \dot{M}_s c_s dT_s.$$ (3.20)

Then the following first order ordinary differential equation (ODE) for solid is obtained as follows

$$\dot{M}_s c_s dT_s = \frac{\alpha A_t}{L_k} \left(T_g - T_s \right) dz.$$ (3.21)

And in the dimensionless form the ODE for solid is expressed as

$$\frac{dT_s}{dZ} = St_s \left(T_g - T_s \right).$$ (3.22)

Where the Stanton number for solid is expressed by the following equation

$$St_s = \frac{\alpha A_t}{\dot{M}_s c_s}.$$ (3.23)

Moreover, the specific heat capacity ratio is defined as

$$\Omega = \frac{St_s}{St_g} = \frac{\dot{M}_g c_{pg}}{\dot{M}_s c_s}.$$ (3.24)

Then by substituting the value of $(\dot{M}_g)$ from Eq. 3.5 the following equation for specific heat capacity ratio is obtained

$$\Omega = \frac{\dot{M}_F c_{pg} \left(1 + \lambda L \right)}{\dot{M}_s c_s}.$$ (3.25)

Furthermore, the fuel mass flow rate is replaced by energy consumption E_s from Eq. 3.8. Therefore, the specific heat capacity ratio Ω is represented in the following new form

$$\Omega = \frac{E_s c_{pg} (1 + \lambda L)}{c_s hu}.$$ (3.26)

The two first order ordinary differential equations need two boundary conditions to be solved. These two boundary conditions are

$$T_{s_{(z=0)}} = T_{s,in}$$

$$T_{s_{(z=L_k)}} = T_{s,f}.$$

(3.27)

Where
$T_{s,in}$, the inlet solid temperature, and
$T_{s,f}$ is the outlet temperature from the burning zone.

3.3.3   Analytical solution for $\Omega = 1$

This section describes the analytical solution for a special case in which the heat capacity ratio is equal to unity ($\Omega = 1$, $St_s = St_g$). For $\Omega = 1$ the temperature profiles for solid and gas are linear as shown in Fig. 3.2. From heat exchanger basics the following two equations are obtained
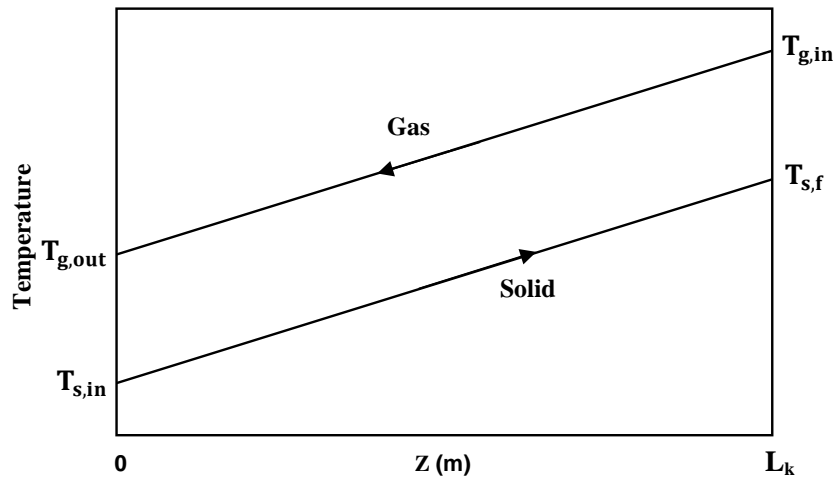

Figure 3.2: Schematic representation for the temperature profile in case of $\Omega =1$.

$$\frac{T_{g,in} - T_{s,in}}{T_{g,out} - T_{s,in}} = 1 + St_s$$

(3.28)

$$\frac{T_{s,f} - T_{s,in}}{T_{g,out} - T_{s,in}} = St_s.$$

(3.29)

From Eq. 3.29 the outlet gas temperature is obtained as follows

$$T_{g,out} = \frac{\Delta T_s}{St_s} + T_{s,in}.$$

(3.30)

Where
$\Delta T_s = T_{s,f} - T_{s,in}$, the solid temperature difference.

By solving Eq. 3.28 and Eq. 3.30 together, the inlet gas temperature is obtained as

$$T_{g,in} = \Delta T_s \left(\frac{1 + St_s}{St_s}\right) + T_{s,in}. \tag{3.31}$$

From the energy balance for the combustion chamber the gas inlet temperature is obtained as

$$T_{g,in} = T_{ad} = \frac{hu}{c_{pg}(1 + \lambda L)} + T_a. \tag{3.32}$$

From these two equations Eq. 3.31 and Eq. 3.32, the excess air number which achieve the heat capacity ratio of unity (Ω=1) is obtained as

$$\lambda = \frac{1}{L}\left(\frac{huSt_s}{c_{pg}\left(\Delta T_s(1 + St_s) + St_s(T_{s,in} - T_a)\right)} - 1\right). \tag{3.33}$$

Then from Eqs. 3.9, 3.30 and 3.33 the energy consumption equation is obtained as

$$E_s = \frac{c_s\left(\Delta T_s(1 + St_s) + St_s(T_{s,in} - T_a)\right)}{St_s}. \tag{3.34}$$

In most cases $T_{s,in} \cong T_a$, therefore the equation can be represented in easier form as following

$$T_{g,out} = \frac{\Delta T_s}{St_s} \tag{3.35}$$

$$T_{g,in} = \Delta T_s \left(\frac{1 + St_s}{St_s}\right) + T_{s,in} \tag{3.36}$$

$$\lambda = \frac{1}{L}\left(\frac{huSt_s}{c_{pg}\Delta T_s(1 + St_s)} - 1\right) \tag{3.37}$$

$$E_s = \frac{c_s\Delta T_s(1 + St_s)}{St_s}. \tag{3.38}$$

Figure 3.3 represents the energy consumption as function of the Stanton number. The higher the Stanton number and the heat transfer coefficient (α), the lower the energy consumption (E_s). This E_s only depends on the required firing temperature and the Stanton number. In this figure the solid temperature difference is ΔT_s= 950 K for example. The specific heat capacity c_s is assumed as 0.85 $kJ/(kg.K)$. For $St_s \longrightarrow \infty$ the lower limit of energy consumption is $E_s = 0.83\ MJ/kg_s$.

In addition, Fig. 3.4 represents the excess air number as function in the Stanton number. The higher the Stanton number the higher the excess air number (λ) which fulfill the specific heat capacity ratio of unity (Ω= 1).

Figure 3.5 represents the outlet gas temperature as the function of Stanton number. It is obvious from the figure that the higher the Stanton number is the lower the outlet gas temperature ($T_{g,out}$). The data is represented in table 3.1.
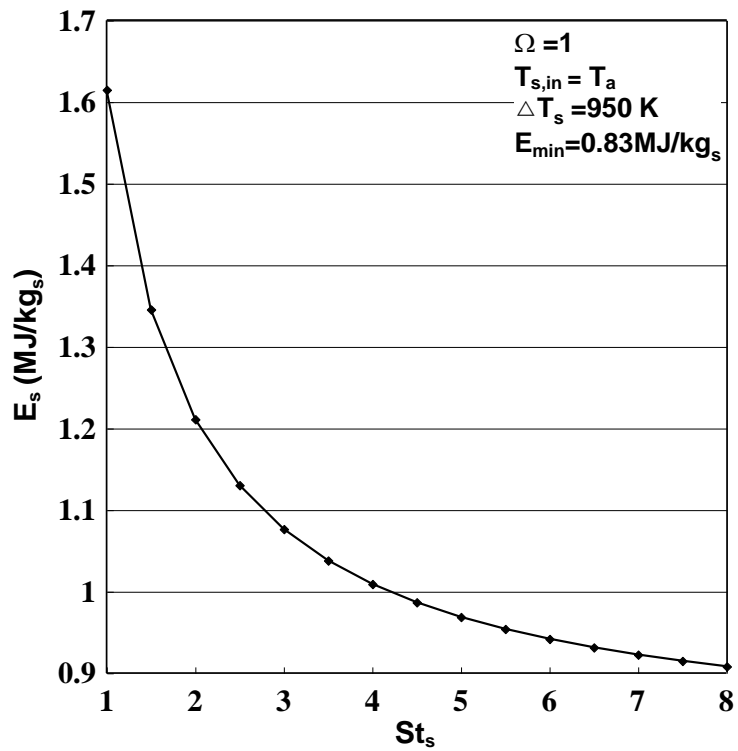
Figure 3.3: Energy consumption for $\Omega =1$.
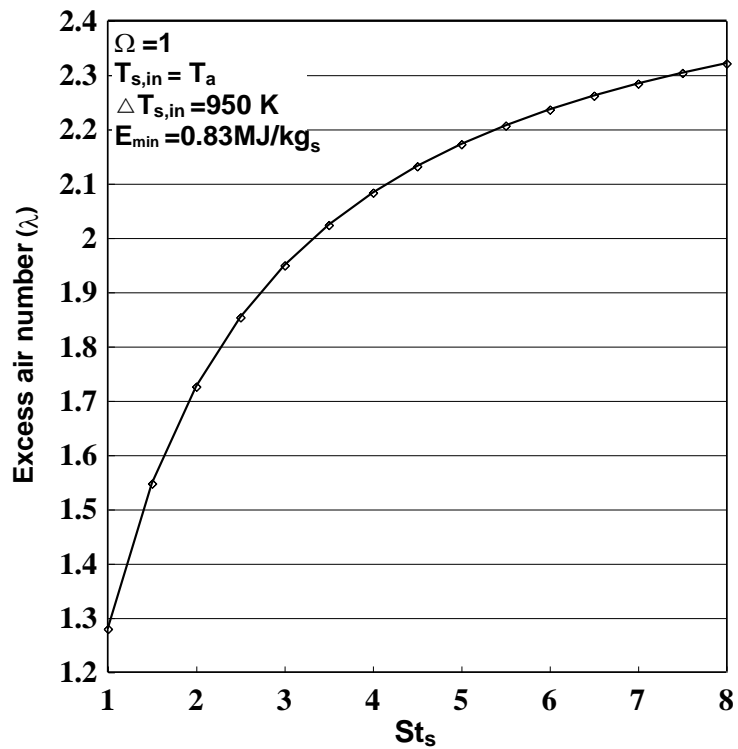
Figure 3.4: Excess air number for special case of $\Omega =1$.

Table 3.1: Some data used in calculations

Symbol	Description	Value	Unit
used fuel	natural gas H type		
c_{pgo}	specific heat of air	1.0	$kJ/(kg.K)$
L_k	kiln length	50	m
c_s	Specific heat of solid	0.85	$kJ/(kg.K)$
$\dot{M}_s$	capacity of kiln	20000	$t/year$
$T_{s,in}$	solid inlet temperature	50	°C
$T_{s,f}$	solid outlet temperature	1000	°C
L	air demand	16.9	kg_{air}/kg_{fuel}
hu	lower heating value	47300	kJ/kg_F
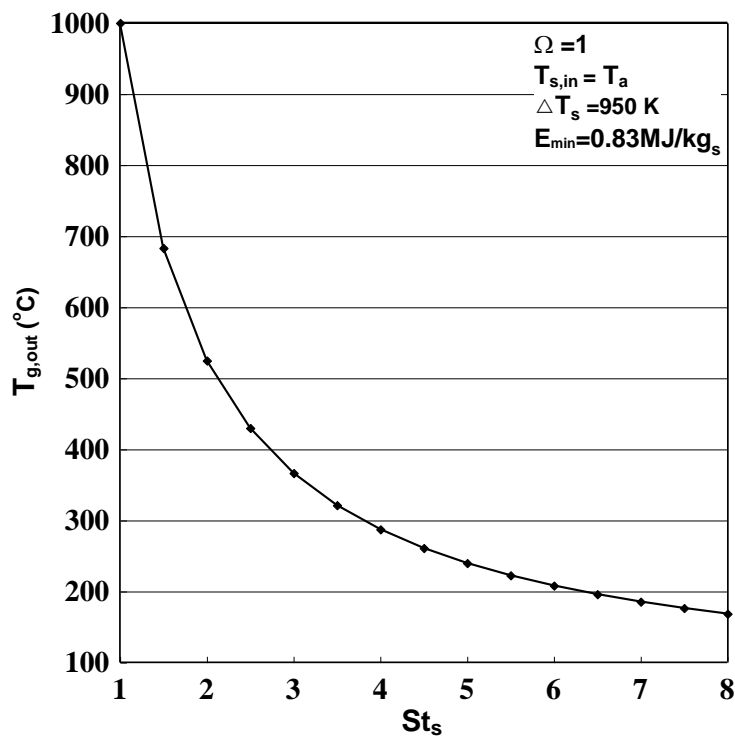
Figure 3.5: Outlet gas temperature for special case of $\Omega = 1$.

3.3.4 Analytical solution for different Ω

It is important to obtain the analytical solution not only for the foregoing special case $\Omega = 1$, but also for the other values of the specific heat capacity ratio (i.e. $\Omega \neq 1$). The following two equations are the obtained equations from solving the foregoing two ODEs

$$T_g(Z) = \frac{\Omega' T_{s,in} \left(1 - e^{St_s(\Omega'-1)Z}\right) + T_{g,out} \left(\Omega' e^{St_s(\Omega'-1)Z} - 1\right)}{\Omega' - 1} \tag{3.39}$$

$$T_s(Z) = \frac{T_{s,in} \left(\Omega' - e^{St_s(\Omega'-1)Z}\right) + T_{g,out} \left(e^{St_s(\Omega'-1)Z} - 1\right)}{\Omega' - 1}. \tag{3.40}$$

Where

$$Z = \frac{z}{L_k} \tag{3.41}$$

and

$$\Omega' = \frac{1}{\Omega} = \frac{\dot{M}_s c_s}{\dot{M}_g c_{pg}}. \tag{3.42}$$

To obtain the outlet gas temperature equation, the following boundary condition $(T_{s(z=L_k)} = T_{s,f})$ has to be applied in Eq. 3.40

$$T_{g,out} = \frac{T_{s,f}(\Omega' - 1) - T_{s,in}(\Omega' - e^{St_s(\Omega'-1)})}{e^{St_s(\Omega'-1)} - 1}. \tag{3.43}$$

Then from these two equations 3.39 and 3.40 the temperature distribution for gas and solid for case "A" can be drawn. The energy consumption E_s is represented by Eq. 3.9, $T_{g,out}$ is represented by Eq. 3.43 and the specific heat capacity ratio is represented by Eq. 3.26. From these equations the energy consumption is a function of the Stanton number and excess air number $(E_s = \text{f}(T_{g,out}, \lambda))$. The data used in the calculations are represented in table 3.1.

The equations are solved by a MATLAB program. The output results from this program are represented in Fig. 3.6 which shows a comparison of the energy consumption for omega equal one $(\Omega = 1)$ with that of case A under the same condition of case A. The figure shows the energy consumption as a function of the Stanton number for
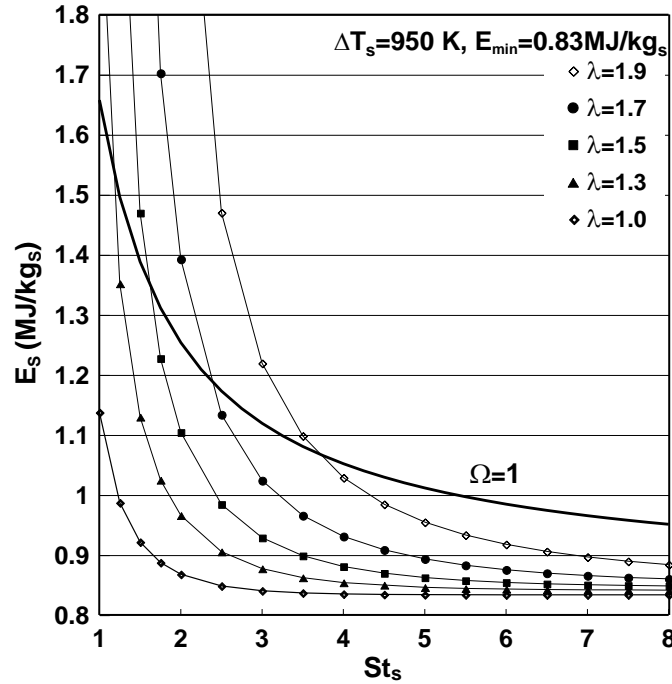

Figure 3.6: Energy consumption for case A.

different excess air numbers. It is obvious that for constant excess air number, the energy consumption decreases as Stanton number increases. The trend is the same for any excess

air number. The Stanton number increases if the heat transfer coefficient (α) increases. The figure demonstrates that for Stanton < 3, with a little decrease in Stanton number results in a big decrease of E_s for same excess air number. Furthermore, the figure shows also that as excess air number increase the energy consumption increase. From the figure the value of the Stanton number with excess air number with its corresponding energy consumption the specific heat capacity ratio which is equal to one could be found.

The following sections focus on the results from solving the two first order ordinary differential equations (ODEs) Eqs. 3.16 and 3.21 of gas and solid numerically. The commercial code (bvp4c) is used to solve system of coupled ODE and boundary conditions. The bvp4c solver requires two boundary conditions for the solution in which the solid inlet and outlet temperatures are known (inlet temperature of solid $T_{s,in}$, and outlet solid temperature $T_{s,f}$). Appendix (A), shows the basics of bvp4c solver. Furthermore, from the program results the temperature profiles for the gas and solid along the two zones (preheating and firing) are obtained. Some variables used in solving this system are listed in table 3.1.

Figure 3.7 shows the effect of Stanton number on temperature distribution for constant excess air. This figure illustrates that as Stanton number increases the energy consumption E decreases and so the outlet gas temperature decreases. The value of energy consumption could be seen in Fig. 3.6. Also figure 3.7 shows that as Stanton number increases the temperature profiles are completely different. As a consequence, the Stanton number has a big influence on the outlet gas temperature.
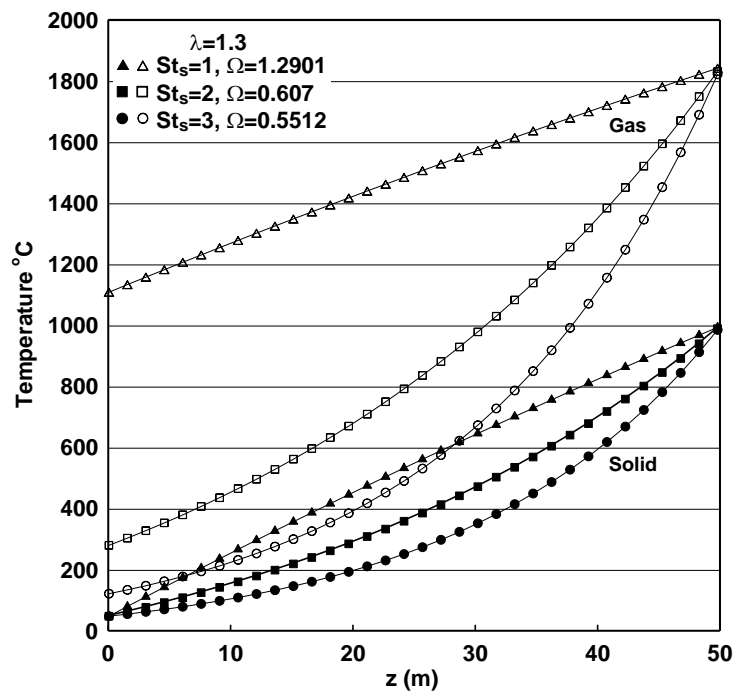
Figure 3.7: Temperature profile, case A, $\lambda = 1.3$.

Figure 3.8 shows the influence of excess air number on both temperature distribution and outlet gas temperature. The figure shows that the lower the excess air number the lower the outlet gas temperature, this is due to the decrease in energy consumption for

St_s= 3 with the required outlet solid temperature. The figure shows that at λ = 1.3 the flue gases has a lower temperature which is required to prevent thermal pollution. Moreover, from these results the outlet gas temperature can be controlled and regulated according to the requirements. In some cases the outlet flue gases are used for the drying process and its temperature should be a little bit higher.
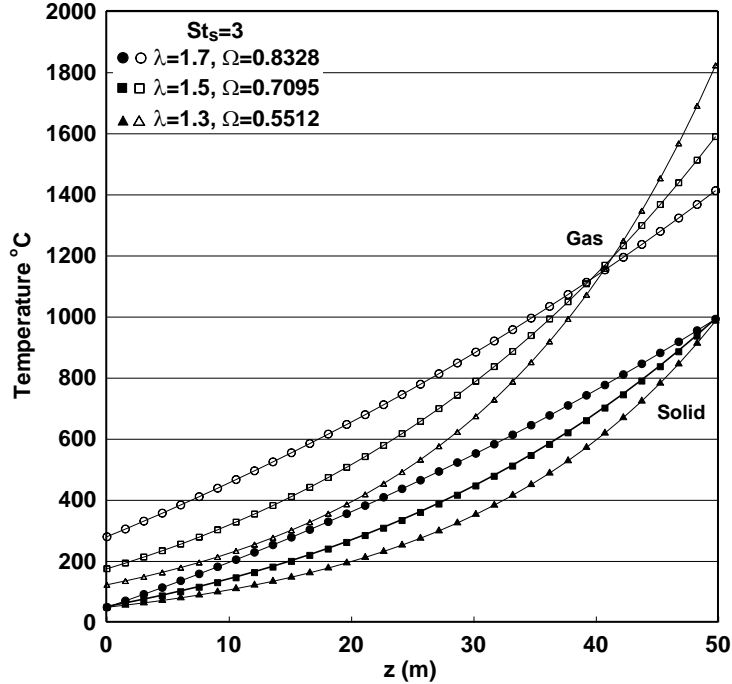
Figure 3.8: Temperature profile for different excess air number, case A, St_s=3.

3.4 Effect of firing zone length

Case A has a low heat transfer coefficient (α) because of low axial velocity, the gas flows mainly above and not through the load. Therefore, a row of burners is used for gas mixing in cross section. The following sections study the effect of firing zone length.

3.4.1 The whole kiln is the firing zone : Case B

In this section the two zones, firing and preheating zones, are considered as firing zone and will be further called "Case B". In addition to the previous assumptions used in case A, the following assumption is included.

Assumption :

⋆ The fuel is distributed uniformly along the firing zone of length L_f.

Figure 3.9 shows schematic description for case B. This figure shows that there is a homogeneous inlet of combustion gas along the kiln.
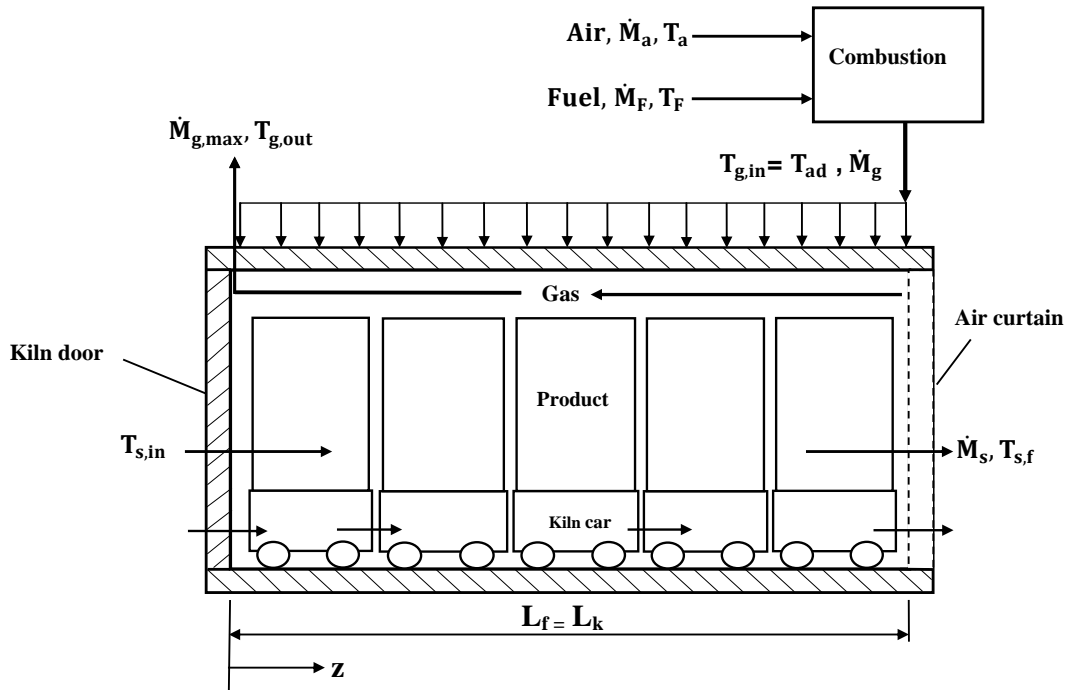
Figure 3.9: Continuously combustion gas injection along the entire kiln (case B only firing zone).

The axial distribution of gas flow is given as

$$\dot{M}_g(z) = \frac{\dot{M}_{g,max}}{L_f}(L_k - z).$$

(3.44)

Then, with Eq. 3.41 the dimensionless form is obtained

$$\dot{M}_g(Z) = \frac{\dot{M}_{g,max}L_k}{L_f}(1 - Z).$$

(3.45)

Where
L_k, the length of the kiln,
L_f, the length of the firing zone,
$\dot{M}_{g,max}$, the maximum mass flow rate of gases, and
$Z = \dfrac{z}{L_k}$.

Then by differentiation with respect to Z the following differential form for the gas mass flow rate is obtained

$$\frac{d\dot{M}_g}{dZ} = -\frac{\dot{M}_{g,max}L_k}{L_f}.$$

(3.46)

- **Ordinary differential equation for gas**

  The gas enthalpy flow is expressed as

$$\dot{H}_g = \dot{M}_g(z)c_{pg}T_g(z).$$

(3.47)

Now there are two variables depending on length, z, so that the change in gas enthalpy flow is represented as

$$d\dot{H}_g = \dot{M}_g(z)c_{pg}dT_g + T_g c_{pg}d\dot{M}_g(z). \tag{3.48}$$

Furthermore, the convective heat transfer between the gas and solid can be expressed as mentioned in Eq. 3.14. For this case there is another source of enthalpy flow input due to combustion of fuel is expressed as in the following equation

$$d\dot{H}_{in} = \dot{Q}_{f,t}\frac{dz}{L_f} = \dot{M}_{g,max}c_{pg}T_{ad}\frac{-dz}{L_f}. \tag{3.49}$$

There is a negative sign in $d\dot{H}_{in}$ because the addition is in the opposite direction of axes z.

From the energy balance, the inlet energy to the element is equal to the outlet one with neglecting heat loss. This energy balance is shown in the following equation

$$\dot{M}_g(z)c_{pg}dT_g + T_g c_{pg}d\dot{M}_g(z) = \frac{\alpha A_t}{L_k}(T_g - T_s)dz - \dot{M}_{g,max}c_{pg}T_{ad}\frac{dz}{L_f}. \tag{3.50}$$

Equation 3.50 can be represented in the following form as a general equation

$$\dot{M}_g(z)\frac{dT_g}{dz} = \frac{\alpha A_t}{L_k c_{pg}}(T_g - T_s) - \frac{\dot{M}_{g,max}}{L_f}(T_{ad} - T_g). \tag{3.51}$$

By substituting Eq. 3.18 and Eq. 3.45 in Eq. 3.51 the general form for the first order ordinary differential equation (ODE) is obtained as in the following equation

$$(1 - Z)\frac{dT_g}{dZ} = St_g\frac{L_f}{L_k}(T_g - T_s) - (T_{ad} - T_g). \tag{3.52}$$

In case B, the firing length is equal to kiln length ($L_f = L_k$). Therefore, by replacing this condition in the foregoing equation, the equation for case B is obtained

$$(1 - Z)\frac{dT_g}{dZ} = St_g(T_g - T_s) - (T_{ad} - T_g). \tag{3.53}$$

- **Ordinary differential equation for solid**

  There is no change in energy for the solid, so that Eq. 3.22 represents the solid equation as before in case A. The two first order ordinary differential equations need two boundary conditions to be solved. These two boundary conditions are

$$T_{s_{(z=0)}} = T_{s,in}$$

$$\tag{3.54}$$

$$T_{s_{(z=L_k)}} = T_{s,f}.$$

By the same way the MATLAB (commercial code) is used to solve the system of ordinary differential equations (ODEs) by bvp4c solver to obtain the results.

Figure 3.10 illustrates the energy consumption as a function of Stanton number for different excess air numbers. The figure demonstrates that for constant excess air number, the energy consumption decreases as Stanton number increases. The trend is the same for any excess air number. Furthermore, the figure shows that as excess air number increase the energy consumption increase for the same Stanton number.
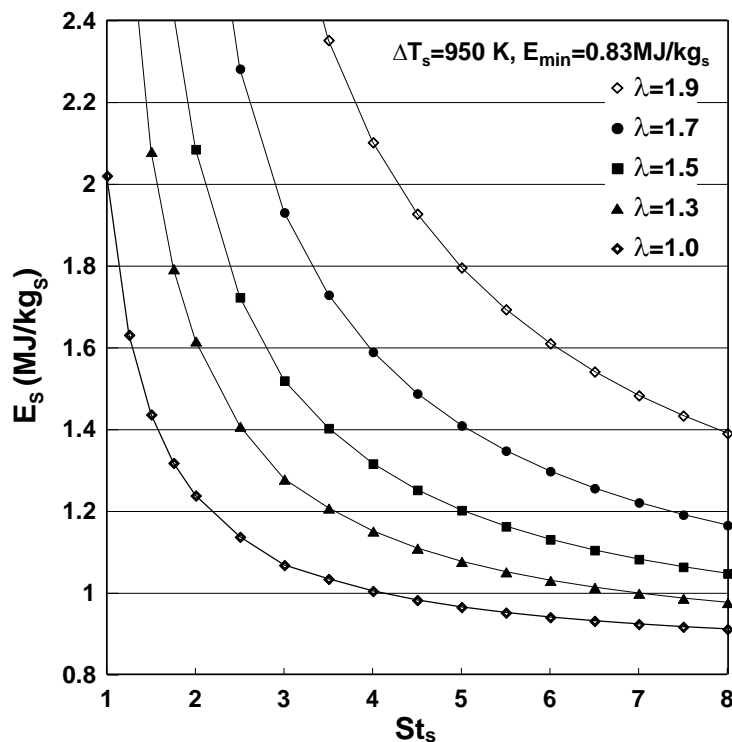
Figure 3.10: Energy consumption for case B.

Figure 3.11 shows the ratio of energy for both cases "B" and "A" as a function of Stanton number for different values of excess air number. From the figure, it can be seen that the energy consumption for case "B" is always higher than case "A". The difference is the higher the Stanton number and the lower excess air number is.

Figures 3.12 and 3.13 show the temperature profiles of the gas and the solid.
Figure 3.12 shows the effect of Stanton number on temperature profile for constant excess air number of value $\lambda = 1.3$. The figure shows that the lower the Stanton number is the higher the energy consumption which results in a higher flue gas temperature. By comparing Fig. 3.12 with the corresponding figure in case "A" (Fig. 3.7), it is obvious that the profiles are completely different.

The influence of excess air number on temperature distribution for both gas and solid is shown in Fig. 3.13. By comparing Fig. 3.13 with the corresponding figure in case "A" (Fig. 3.8), it is obvious that the profiles are completely different. The gas

temperature has a maximum value. The temperature of the solid increases sharply at the entrance and weaker at the end of the firing zone.
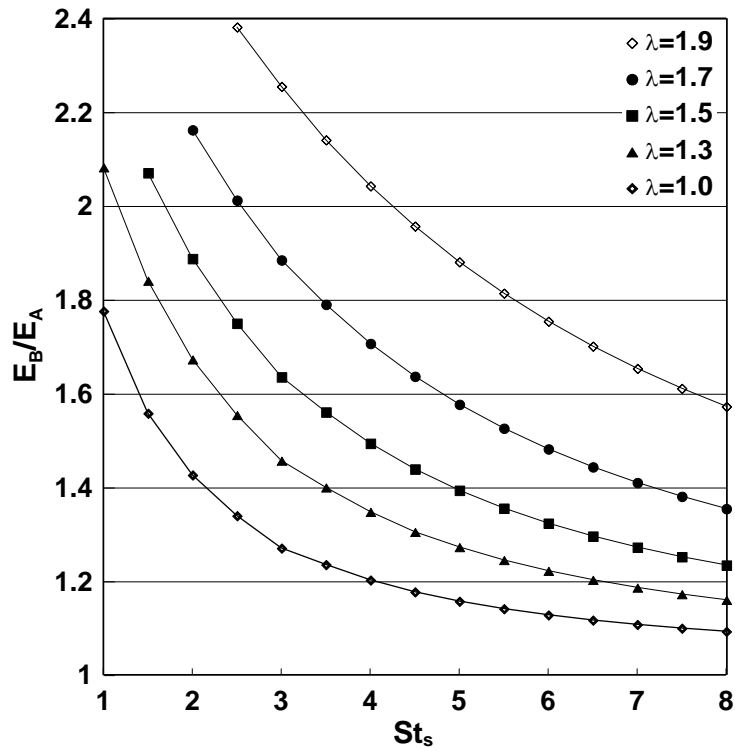
Figure 3.11: Comparison of energy consumption for cases A and B.
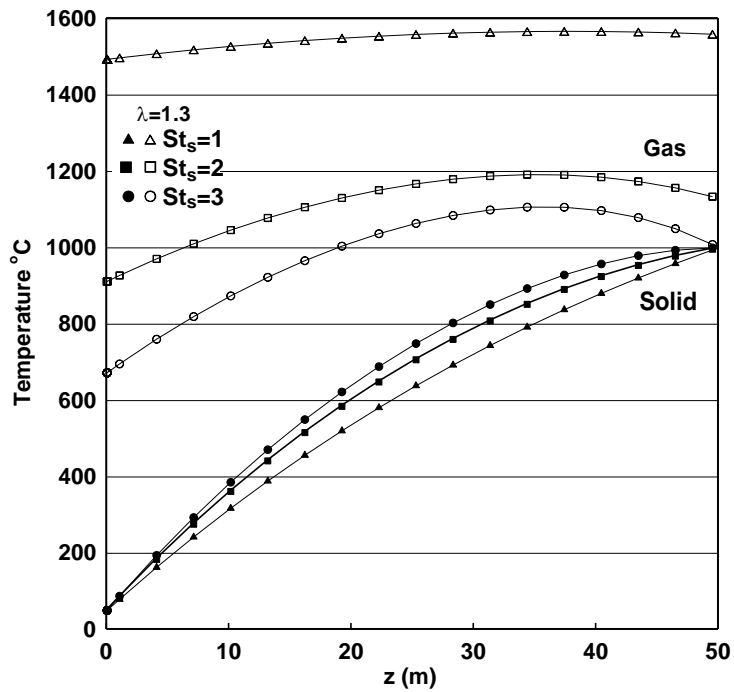
Figure 3.12: Temperature profile, case B, $\lambda = 1.3$.
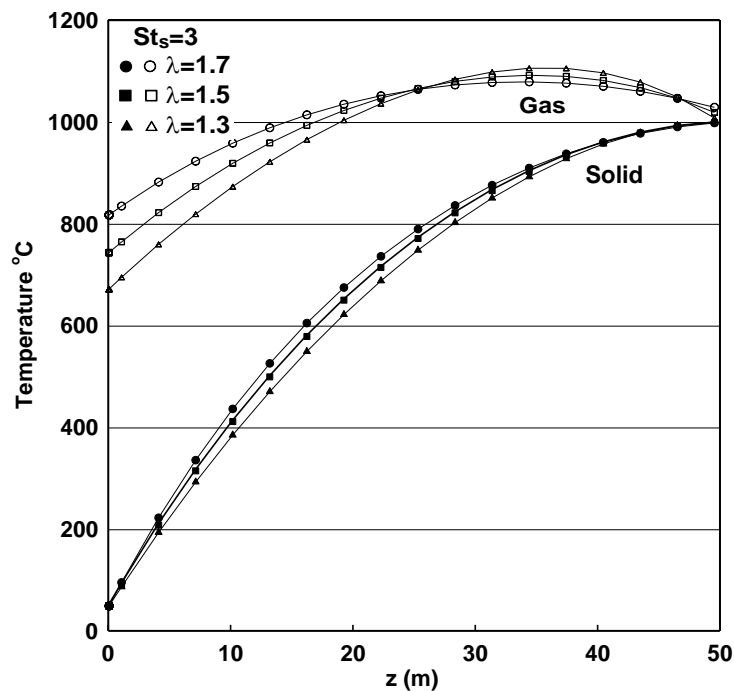
Figure 3.13: Temperature profile, case B, $St_s = 3$.

3.4.2 Firing zone length equal to preheating zone: Case C

In this section, another special case in which the firing length is equal to the preheating length ($L_f = 0.5L_k$) is considered. This case will be called "case C". Figure. 3.14 shows a schematic description of case "C". This figure shows that there is a homogeneous inlet of combustion gas along the firing zone. For case "C", equation Eq. 3.22 for solid is the same in the two zones (preheating, firing). The gas equation depends on the zone. The preheating zone has the same ODE which represents gas as described in case "A" Eq. 3.17. On the other hand, equation 3.52 represents the gas equation for the firing zone. Also as previously analyzed in case "B", case "C" can be solved numerically. The following sections describe the results from the numerical solution of case "C".

Figure 3.15 illustrates the energy consumption as a function of the Stanton number for different excess air numbers. The trend is the same as illustrated before in cases "A" and "B".

Figure 3.16 shows the energy ratio for both cases "C" and "A" as a function of Stanton number for different values of excess air number. From the figure, it can be seen that case "C" has higher energy consumption than case "A".

Figure 3.17 and 3.18 demonstrate the effect of Stanton number and excess air number λ on temperature profiles.

Figure 3.17 shows the temperature profile slope for the gas changes from firing zone to preheating zone. The influence on the solid temperature is weak. The increase of the solid temperature is approximately linear. The figure shows that, the lower the Stanton number is the higher the energy consumption which results in a higher flue gas

Figure 3.14: Kiln with heating and firing zones(case C).
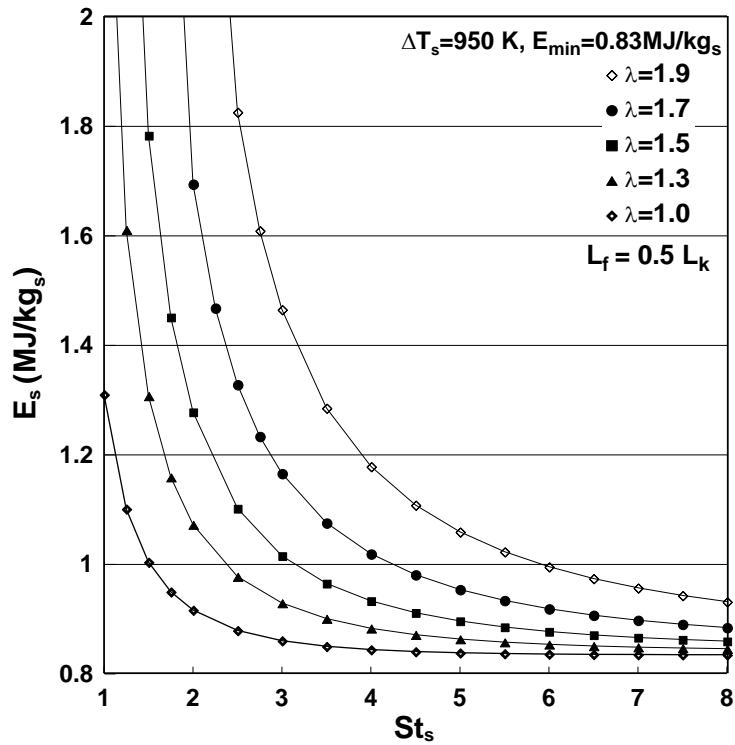
Figure 3.15: Energy consumption for case C.

temperature.

Figure 3.18 shows the influence of excess air number on temperature profile for both gas and solid. The influence on the solid temperature is weak. The increase of the solid temperature is approximately linear. The figure shows that the higher the excess air

number is the higher the energy consumption, resulting in a higher flue gas temperature.
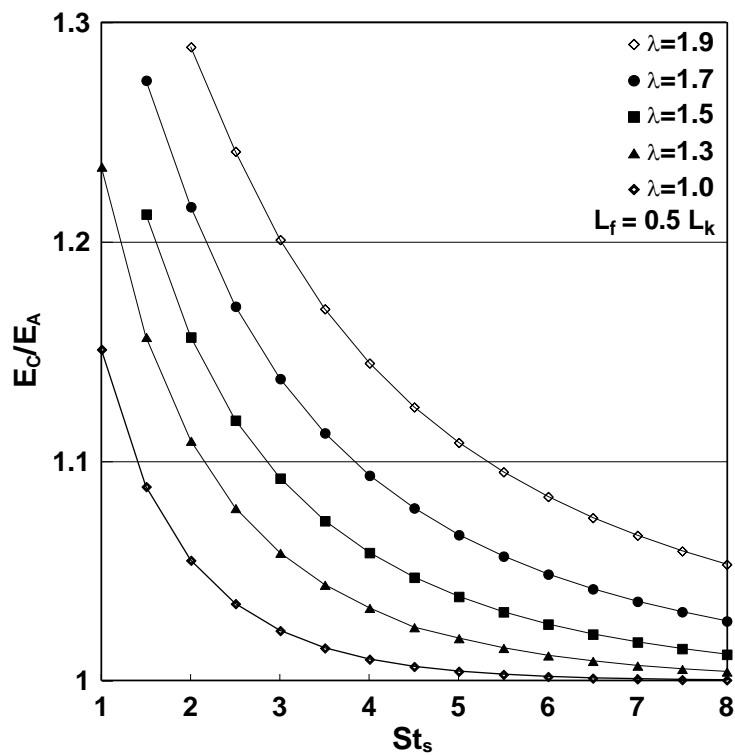
Figure 3.16: Comparison of energy consumption for cases A and C.
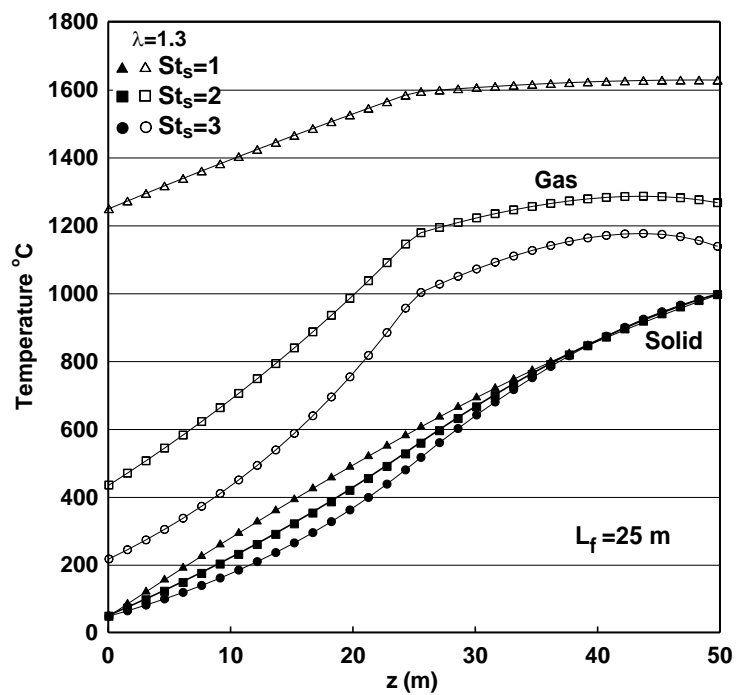
Figure 3.17: Temperature profile, case C, with firing zone length of 25 m, $\lambda = 1.3$.
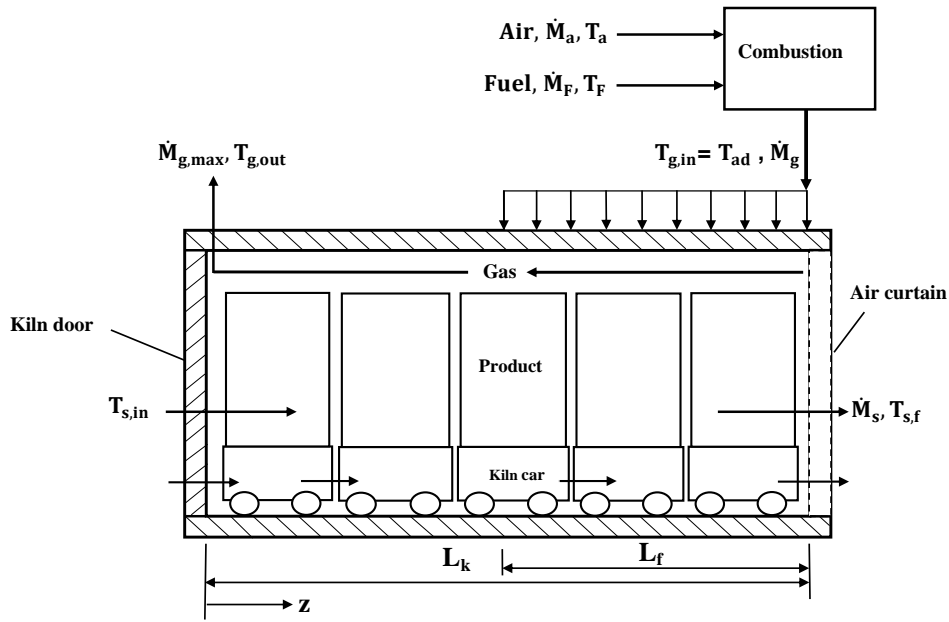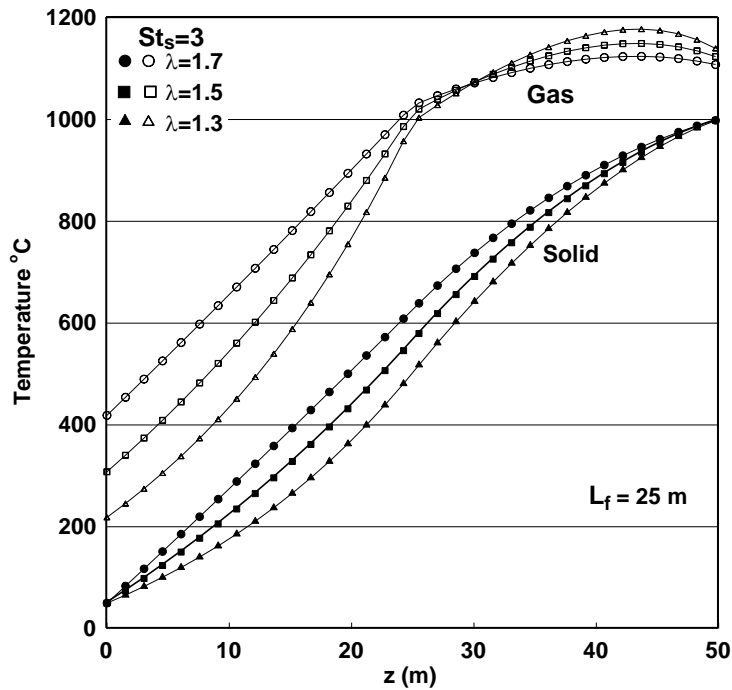
Figure 3.18: Temperature profile, case C, with firing zone length of 25 m, St_s=3.

3.4.3 Different firing zone length

This section presents a sample of results to show the effect of firing zone length on temperature profiles for both gas and solid. In the burning zone the two general equations Eq. 3.22 and Eq. 3.52 for solid and gas respectively are solved. In the preheating zone the two general equations Eq. 3.22 and Eq. 3.17 for solid and gas are solved so that the effect of firing zone length can be studied.

Firing length has great effects on the energy consumption according to the value of excess air number for the same Stanton number. The following curves explain the effect of the firing length on energy consumption.

Figure 3.19 and 3.20 show the influence of the firing length ratio on the energy consumption for different excess air numbers and Stanton numbers. The energy consumption always increases with the firing zone length. The increase is stronger the lower the Stanton number and the higher the excess air number. The energy consumption increases progressively with the firing zone length. However, up to approximately $\sim$30 %, the increase is relatively low. As a consequence, from the model, the firing zone length should be as short as possible for low energy consumption.

In Fig. 3.21 the temperature profiles are compared for the three cases for $St_s = 2$ and $\lambda = 1.3$ as an example. From the figure it can be seen that, the longer the firing zone is the stronger is the increase of the solid temperature at the beginning and the lower at the end of the firing zone. For case "A" a very high gas inlet temperature occurs. This high gas temperature results in high NO_x emissions and a higher quality product and expensive refractory materials. As a consequence, an extreme short firing zone results in overly high gas temperatures and in a used proper profile of the solid temperature.
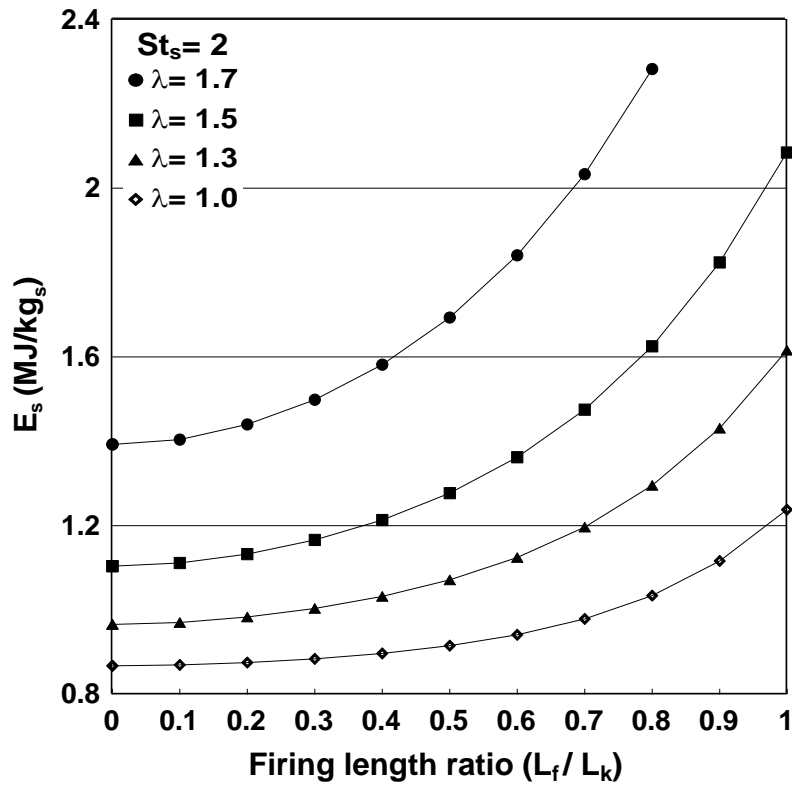
Figure 3.19: Influence of firing zone length on energy consumption for $St_s = 2$.
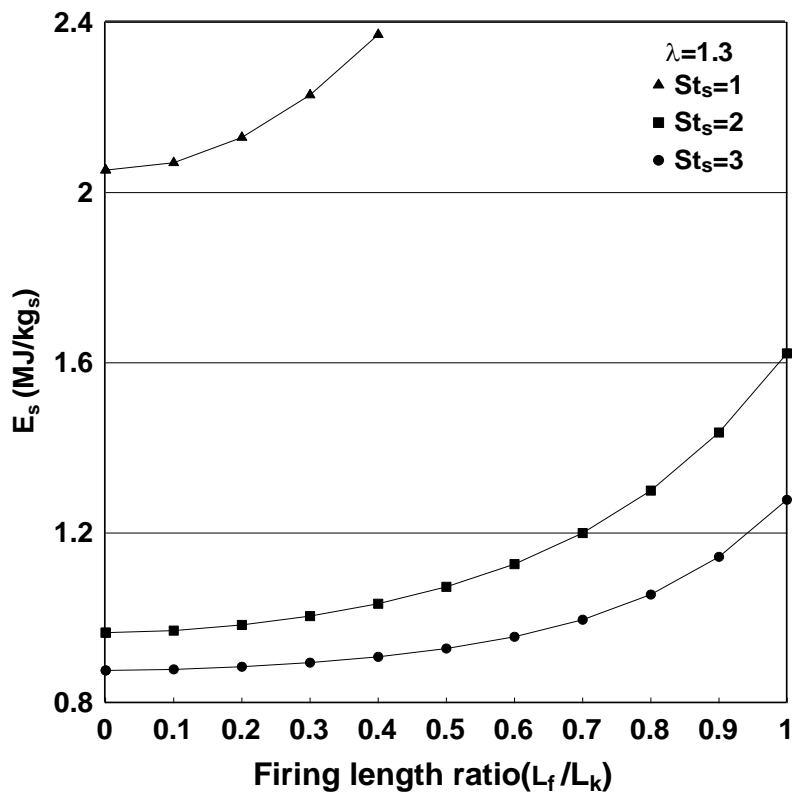
Figure 3.20: Influence of firing zone length on energy consumption for $\lambda = 1.3$.
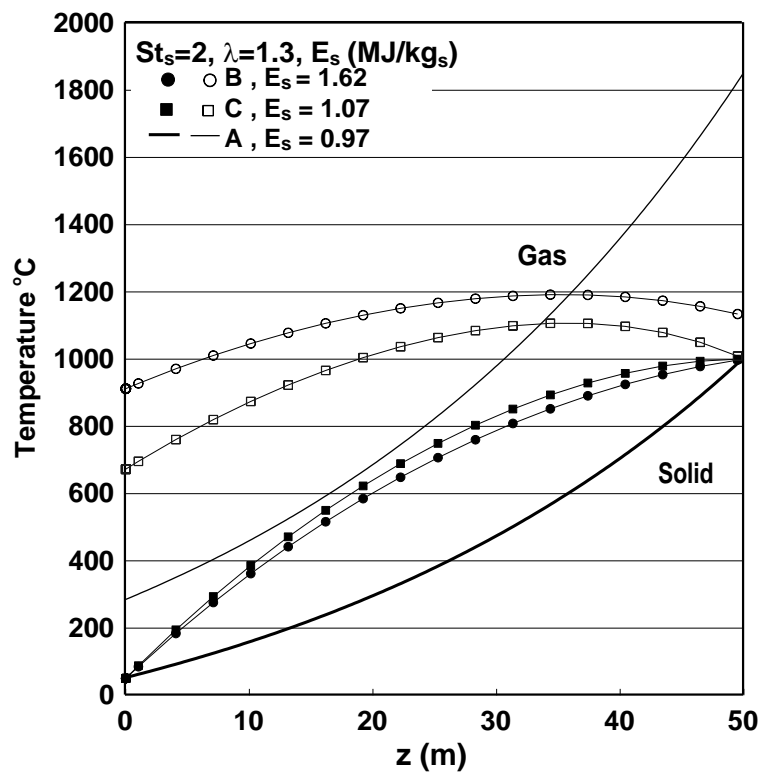
Figure 3.21: Comparison between cases A, B and C with same outlet solid temperature for $St_s = 2$.

Chapter 4

Heat Transfer Modeling for Vitrified Clay Pipes Kiln

4.1 Introduction

Based on the complexity of heat transfer mechanism in a tunnel kiln, it is important to study the heat transfer for a product with a simple shape. Therefore, vitrified clay pipes kiln is used to analyze the heat transfer.

Figure 4.1 shows the cross sectional view of a vitrified clay pipe kiln. The vitrified clay pipes are carried on the kiln car which moves inside the kiln on a railway. The kiln car consists of car bricks and kiln furniture. The kiln furniture consists of supported cylinders which lay between a layer of fire clay plate and a plate. It is obvious
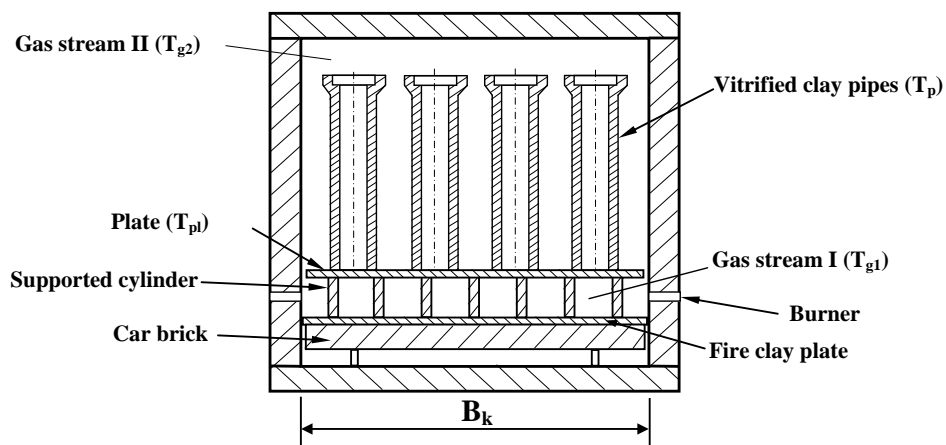
Figure 4.1: Cross section of vitrified clay pipes kiln.

from Fig. 4.1 that the outlet gases enter the kiln from the indicated burners. The gases enter the kiln furniture between the plate and the fire clay plate. Based on the last assumptions, the fuel is distributed uniformly along the burning zone. As a consequence, the gases are distributed uniformly along the burning zone as seen in Fig. 4.2. A portion of the combustion gases escapes from the kiln furniture and goes up to heat the vitrified clay pipes. As a result, there are two streams of gases: gas stream I, which passes across the supported cylinders and between the two parallel plates (fire clay plate, plate)

gas stream II, which escapes from the space between the kiln side walls and the plate and it passes across the vitrified clay pipes. Obviously, the main source of the gases is the combustion gases which come from the burners. The used data in calculations is represented in table 4.1.
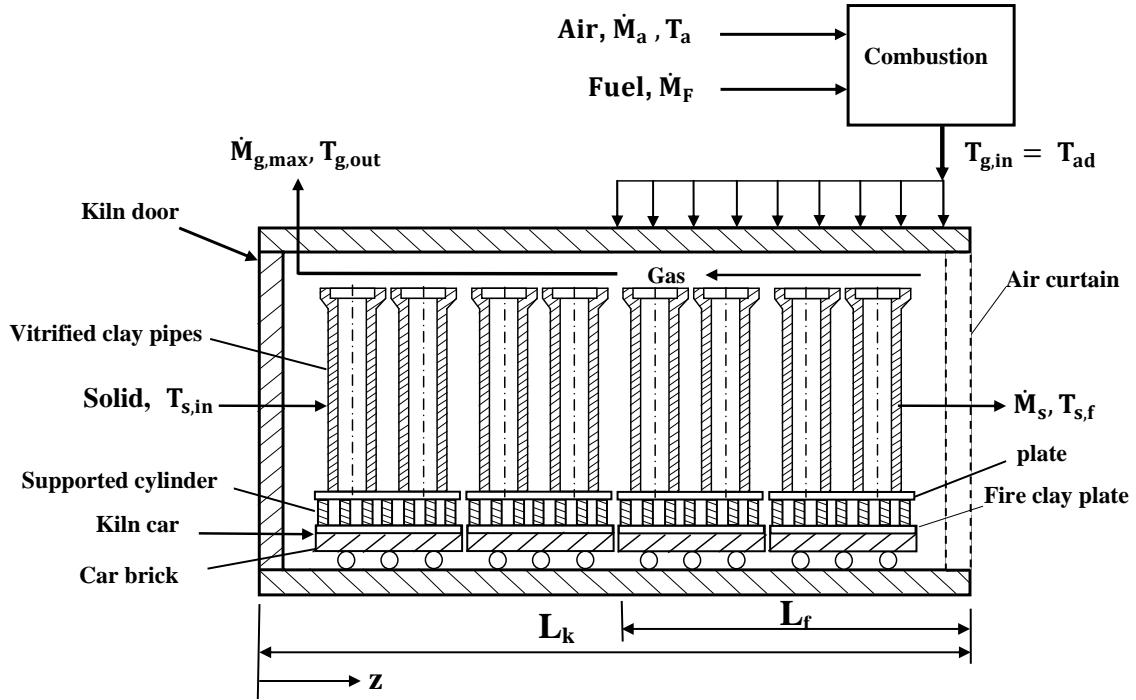
Figure 4.2: Schematic description of vitrified clay pipes kiln.

This thesis focuses on the burning and preheating zones, so that the calculations are related to these two zones. Furthermore, the calculations take into consideration the pipes and kiln furniture without car bricks. Due to highly sintering region in the tunnel kiln, the heat transfer analysis of the kiln must include radiation. The radiation analysis includes gas to solid radiation and solid to solid radiation.

4.2 Modeling of heat transfer

From the last description of the kiln and the gas flows inside the kiln, the heat is transferred from the first gas stream (gas$_I$) to the kiln furniture (fire clay plate, supported cylinders and plate) by convection and radiation. The heat is transferred by convection from the gas to the solids from the gas motion. According to high temperature of the gas the heat is radiated from gas I to plate, fire clay plate, and the supported cylinders. The second part of radiation is due to solid to solid radiation which comes from the fire clay plate to the plate and the radiation which comes from the supported cylinders to the plate. Then the plate radiates the heat to the vitrified clay pipes. Regarding the second gas stream (gas$_{II}$) the two types of heat transfer exist. Due to gas motion through the vitrified clay pipes the heat is transferred by convection to the pipes. Moreover, the gas radiates heat to the pipes. The following sections describe in detail these two types of heat transfer

Table 4.1: Data used in calculations

Symbol	Description	Value	Unit
used fuel	natural gas H type		
B_k	kiln width	4.1	m
B_c	car width	4.0	m
c_{pgo}	specific heat of air	1.0	kJ/(kg·K)
c_{cyl}	specific heat of cylinders	0.85	kJ/(kg·K)
c_{fc}	specific heat of fire clay	0.85	kJ/(kg·K)
c_p	specific heat of pipes	0.85	kJ/(kg·K)
c_{pl}	specific heat of plate	0.85	kJ/(kg·K)
D_i	pipe inner diameter	0.5	m
D	pipe outer diameter	0.613	m
d_{cyl}	cylinder diameter	0.15	m
H_k	kiln height	3.3	m
H_p	pipe height	2.6	m
h_{cyl}	cylinder height	0.300	m
h_{fc}	fire clay height	0.050	m
h_{pl}	plate height	0.080	m
hu	lower heating value	47300	kJ/kg_{fuel}
L_k	kiln length	77	m
L_f	burning zone length	35	m
L	air demand	16.9	kg_{air}/kg_{fuel}
$\dot{M}_{car}$	car mass flow rate	65	t/day
$\dot{M}_{cyl}$	supported cylinders mass flow rate	4	t/day
$\dot{M}_{fc}$	fire clay plate mass flow rate	10	t/day
$\dot{M}_p$	vitrified clay pipes mass flow rate	115	t/day
$\dot{M}_{pl}$	plate mass flow rate	11	t/day
N	total number of pipes	406	
T_a	air temperature	298	K
T_o	reference temperature	273	K
$T_{s,in}$	all solid inlet temperature	150	°C
$T_{p,f}$	pipe outlet temperature	1115	°C
ρ_{cyl}	density of cylinders	800	kg/m³
ρ_{fc}	density of fire clay	1200	kg/m³
ρ_p	density of pipes	2000	kg/m³
ρ_{pl}	density of plate	1000	kg/m³
ε_{cyl}	cylinder emissivity	0.59	
ε_{fc}	fire clay emissivity	0.59	
ε_p	pipe emissivity	0.8	
ε_{pl}	plate emissivity	0.59	

(convection and radiation) inside the kiln. The calculations are done for the vitrified clay pipes kiln.

4.3   Convective heat transfer analysis

Convection takes place due to gas motion along the axial direction of the kiln and its direct contact with solids. As a result, calculating the convective heat transfer coefficient α along the axial direction of the kiln is important. There are two arrangements in the vitrified clay pipes kiln, the first arrangement is a staggered arrangement for the pipes, the second an in-line arrangement for the supported cylinders. Therefore, the following section describes the convective heat transfer analysis for both arrangement.

4.3.1   Vitrified clay pipes

This section describes the way to determine the convective heat transfer coefficient for the vitrified clay pipes in the kiln. Vitrified clay pipes are arranged on kiln car in staggered arrangement. Reynolds number and Nusselt number are required in the calculation of convective heat transfer. So that, some properties are required in the calculations. The following set of equations Eq. 4.2 calculates these required gas properties (density, kinematic viscosity and thermal conductivity). In these equations, the reference temperature $T_o = 273\,K$ is taken [39]. The gas properties at this reference temperature is taken from table 4.2.

$$\frac{\bar{c}_{pg}(T)}{c_{po}(T_o)} = \frac{1}{n_c + 1}\left(\frac{(T/T_o)^{n_c+1} - 1}{(T/T_o) - 1}\right) \tag{4.1}$$

$$\frac{\rho_g}{\rho_o} = \left(\frac{T}{T_o}\right)^{-1} ; \; \frac{\mu_g}{\mu_o} = \left(\frac{T}{T_o}\right)^{n_\mu} ; \; \frac{\nu_g}{\nu_o} = \left(\frac{T}{T_o}\right)^{n_\mu+1} ; \; \frac{\lambda_g}{\lambda_o} = \left(\frac{T}{T_o}\right)^{n_\lambda} \tag{4.2}$$

Table 4.2: Gas properties at reference temperature.

Gas	$\tilde{M}$ (kg/kmol)	ρ_o (kg/m³)	c_{po} (kJ/(kg·K))	n_c -	λ_o (W/(m·K))	n_λ -	μ_o (mg/(m·s))	n_μ -	Pr -
N_2	28	1.26	1.00	0.11	0.024	0.76	16.8	0.67	0.70
Air	29	1.29	1.00	0.10	0.025	0.76	17.4	0.67	0.70
O_2	32	1.44	0.9	0.15	0.025	0.8	19.7	0.67	0.70
CO_2	44	1.98	0.84	0.3	0.017	1.04	14.4	0.77	0.73
H_2O	18	0.81	1.75	0.2	0.016	1.42	8.7	1.13	0.95

Hence to get the heat transfer coefficient in the kiln the following approach is used.

Figure 4.3 illustrates the arrangement of the vitrified clay pipes on the plate. For the staggered arrangement, the flow area decreases from area $(A_{1,p} = S_T H_{k1})$ to the transverse area $(A_T = (S_T - D)H_{k1})$ where, H_{k1}, is the total height of the kiln without the height of kiln furniture (i.e. $H_{k1} = H_k - h_{fc} - h_{cyl} - h_{pl}$) and D, the outer diameter of the pipe.

From basic calculations of cross flow over tube of banks, Reynolds number is calculated from equation 4.3 [40]. The value of Reynolds number in cross flow calculations based on
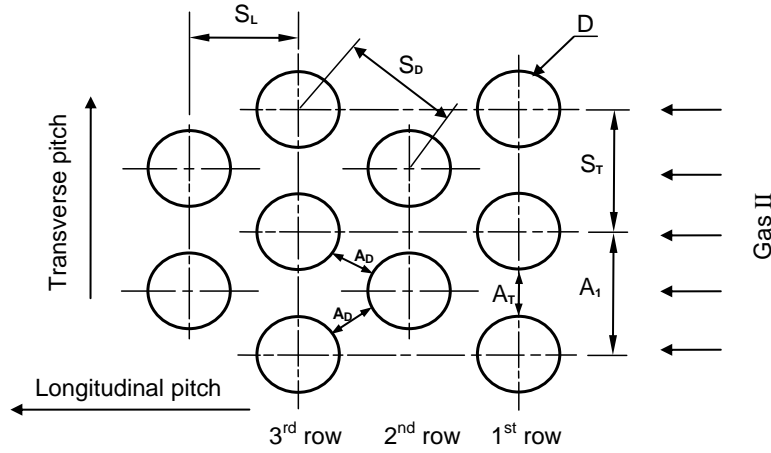
Figure 4.3: Schematic description for pipes arrangement on kiln car.

the maximum velocity w_{max} which is based on the arrangement of pipes

$$Re = \frac{w_{max} D}{\nu_g}. \tag{4.3}$$

Where

$$w_{max} = \frac{S_T}{S_T - D} w_g \tag{4.4}$$

and w_g, the approach velocity of the gas and it is calculated from the following equation

$$w_g = \frac{\dot{M}_g}{\rho_g H_{k1} B_k}. \tag{4.5}$$

The maximum velocity w_{max} is calculated according to Eq. 4.4 for staggered arrangement when the following condition occurred

$$S_D > \frac{(S_T + D)}{2}. \tag{4.6}$$

Where
S_D, the diagonal pitch and it is calculated from the following equation

$$S_D = \sqrt{S_L^2 + \left(\frac{S_T}{2}\right)^2}. \tag{4.7}$$

on the other hand if the condition does not occurred, the maximum velocity will calculated according to Eq. 4.8

$$w_{max} = \frac{S_T}{2(S_D - D)} w_g. \tag{4.8}$$

4.3.2 Supported cylinders

Figure 4.4 demonstrates the arrangement of the supported cylinders which lies between the plate and fire clay plate. The supported cylinders are part of kiln furniture. In the in-line arrangement, the flow area decreases from area $(A_{1,cyl} = S_{T,cyl} h_{cyl})$ to the transverse area $(A_{T,cyl} = (S_{T,cyl} - d) h_{cyl})$. Where h_{cyl}, is the cylinder height and d, the cylinder diameter.
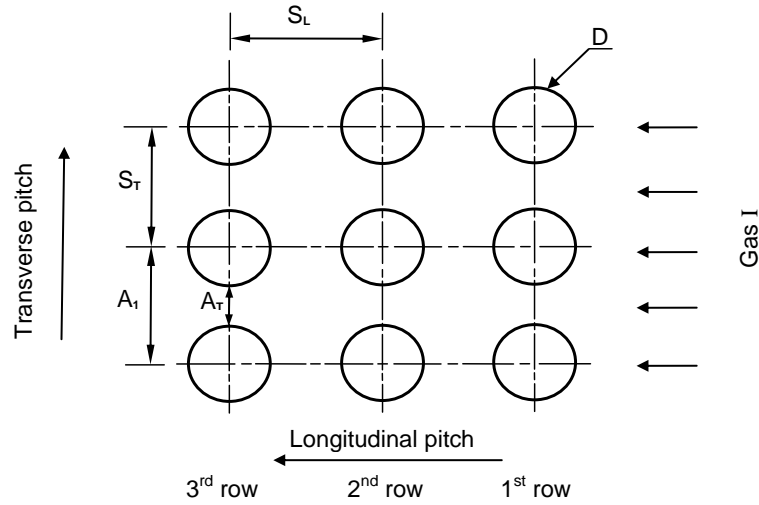
Figure 4.4: Schematic description for cylinders arrangement in the kiln furniture.

The calculation of Reynolds number for the supported cylinders is represented in Eq. 4.9. Where, the maximum velocity w_{max2} is calculated according to Eq. 4.10 which is based on the arrangement of the supported cylinders

$$Re_2 = \frac{w_{max2} d}{\nu_g}. \tag{4.9}$$

$$w_{max2} = \frac{S_{T,cyl}}{S_{T,cyl} - d} w_{g2} \tag{4.10}$$

Where
w_{g2}, the approach velocity of the gas and it is calculated from the following equation

$$w_{g2} = \frac{\dot{M}_{g2}}{\rho_g h_{cyl} B_k}. \tag{4.11}$$

4.3.3 Nusselt number determination

Nusselt number is important to calculate the heat transfer coefficient for convection problems. The Nusselt number can be represented as a function in convective heat transfer coefficient (α) as

$$Nu = \frac{\alpha Lc}{\lambda_g}. \tag{4.12}$$

Where
α, the convective heat transfer coefficient,
λ_g, the thermal conductivity of gas, and
Lc, the characteristic length which is the corresponding diameter in this case.

Consequently, the change in convective heat transfer is as following

$$d\dot{Q}_{conv} = \alpha A_t \left(T_g - T_s\right) dZ. \tag{4.13}$$

Many correlations are used to obtain Nusselt number. These correlations depend on the solid arrangements and type of flow. Zukauskas [41] proposed a correlation to calculate the average Nusselt number. In addition to Zukauskas correlation, there is another correlation derived by Huge [42] and Pierson [43]. But Hausen [44] modified slightly the Previous correlation and presented an empirical formula for the tubes arrangement factor F_a instead of the graphical representation. Therefore, Nusselt number correlations differ from one case to another.

Recently, Khan et al. [45] investigated analytically the heat transfer from tube banks for in-line or staggered arrangement in cross flow under isothermal boundary condition. A correlation for Nusselt number for both arrangements (in-line and staggered) was represented. This correlation is shown in equation 4.14 in which Reynolds number is calculated according to Eq. 4.3 or Eq. 4.9 which is based on the diameter

$$Nu_D = C_1 Re_D^{1/2} Pr^{1/3}. \tag{4.14}$$

Where
D, the diameter of tube, (m)

C_1 was determined according to the arrangement and was reported as follows :

- For in-line arrangement

$$C_1 = \left(0.25 + \exp(-0.55\varphi_L)\right) \varphi_T^{0.285} \varphi_L^{0.212} \tag{4.15}$$

- For staggered arrangement

$$C_1 = \frac{0.61\varphi_T^{0.091}\varphi_L^{0.053}}{\left(1 - 2\exp(-1.09\varphi_L)\right)} \tag{4.16}$$

Where
φ_L, the dimensionless longitudinal pitch, and
φ_T, the dimensionless transverse pitch.

- for pipes

$$\varphi_T = \frac{S_T}{D}, \varphi_L = \frac{S_L}{D} \tag{4.17}$$

- for cylinders

$$\varphi_T = \frac{S_{T,cyl}}{d}, \varphi_L = \frac{S_{L,cyl}}{d} \tag{4.18}$$

4.4 Radiative heat transfer analysis

4.4.1 Introduction

Radiation is one of the heat transfer mechanisms which depends on the high flow temperatures. There are two types of radiation that occur in a kiln; gas radiation and solid to solid radiation. The gas radiation depends on solid emissivity and gas emissivity. For solid emissivity each solid material has an emissivity value stated in tables. The gas emissivity depends on gas temperature and gas mixture. Carbon dioxide and water vapor are the most important gases in gas mixture. Therefore, calculating the emissivity of CO_2 and H_2O is one of the most important steps in radiation calculations.

- **Carbon dioxide and water vapor emissivities determination**

  The total emissivity ε_g of $CO_2 - H_2O$ mixture depends on the temperature, the thickness ($P_g \cdot$s) of the layer (mean beam length), the partial pressure P_g of the radiant gas, and the total pressure p of the gas mixture. An approximate value for the mean beam length s for geometries can be obtained from the equation [46]

$$s = 0.9 \frac{4V_g}{A}. \tag{4.19}$$

  Wherein
  V_g, volume of the gas, and
  A, the surface area around the gas body.
  For example $V_{g_{II}} = V_{k1} - V_{pipes}$, A= surface area of pipes, V_{cyl} =9.68 m^3 total volume of the supported cylinders, and $A_{s,cyl}$=258 m^2.

  The beam length for $gas_I = 0.37$ m.
  The beam length for $gas_{II} = 1.05$ m.

  The volume concentration which is used to calculate the partial pressure for carbon dioxide and water vapor in the gas mixture is obtained from Fig. 4.5 [47]. Therefore, the partial pressure is obtained as

$$P_g = P_t \tilde{X}_g. \tag{4.20}$$

  Where, $\tilde{X}_g$, the volume concentration of the gas, and
  P_t, total pressure.

  Figure 4.6 and Fig. 4.7 show the Hottel's charts used to obtain the CO_2 and H_2O emissivity, respectively. Equation 4.21 represents the approximated equation which used to calculate CO_2 and H_2O emissivities (ε_{g_i}) [48] and i refers to the gas

$$\varepsilon_{g_i} = A_b \exp^{-B_b T}. \tag{4.21}$$

  Where
  A_b and B_b are functions in beam length and partial pressure for carbon dioxide and water vapor. The equation which represent the two functions could be represented as in table 4.3. T represents gas temperature in Kelvin degree.
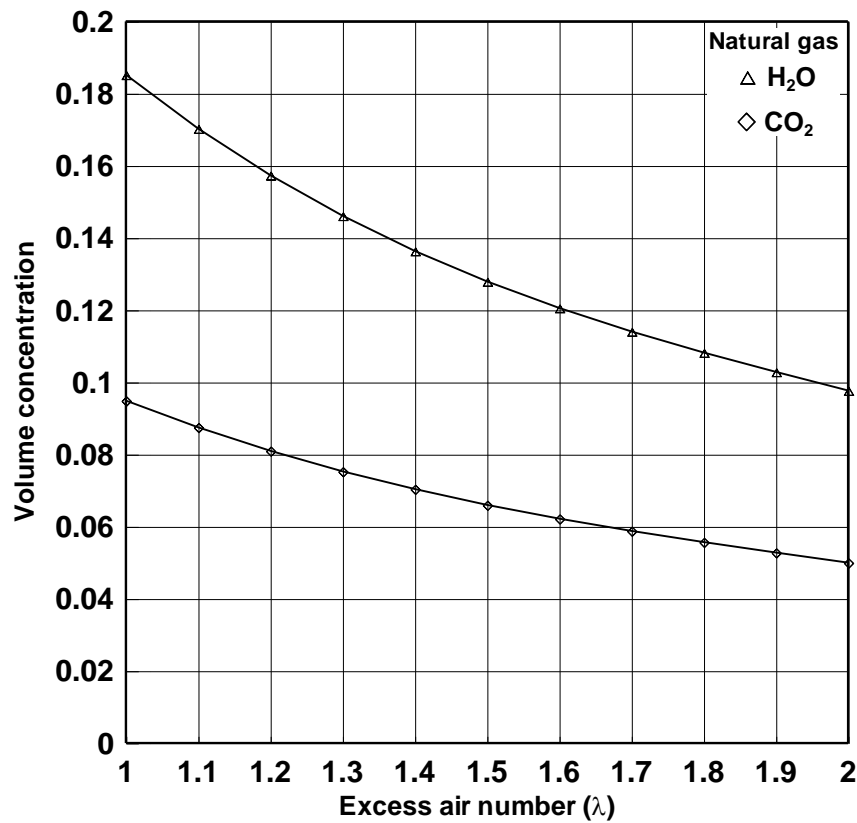
Figure 4.5: Composition of combustion gas of natural gas [47].

Table 4.3: Used equations to calculate $CO_2 - H_2O$ emissivity [48].

Gas	A_b	B_b	P_g·s in bar.m	T in K
CO_2	$0.51(P_g\text{·s})^{0.26}$	$6.7 \times 10^{-4}(P_g\text{·s})^{-0.085}$	$0.01 - 1.5$	> 1200
	$2.0(P_g\text{·s})^{0.54}$		$0.001 - 0.01$	
H_2O	$0.6(P_g\text{·s})^{0.25}$	$5.3 \times 10^{-4}(P_g\text{·s})^{-0.2}$	$0.1 - 2$	> 1000
	$0.87(P_g\text{·s})^{0.47}$		$0.01 - 0.1$	

- **Gas mixture emissivity**

An approximated equation which can be directly used in MATLAB program is used to determine the gas mixture emissivity. The approximated equation 4.22 [48] is used to calculate the total emissivity of carbon dioxide and water vapor mixture

$$\varepsilon_g = \varepsilon_{CO2} + \varepsilon_{H2O} - \varepsilon_{CO2}\varepsilon_{H2O}. \tag{4.22}$$

4.4.2   Gas to solid radiation calculations

Regarding, the previous calculations of gas emissivity for gases and gas mixtures, the radiative heat transfer between gas and its surroundings can be analyzed. In order to perform to do such calculations there is a simplification that should be taken into consideration, the emissivity is equal to the absorptivity ($\alpha_g = \varepsilon_g$) [49].
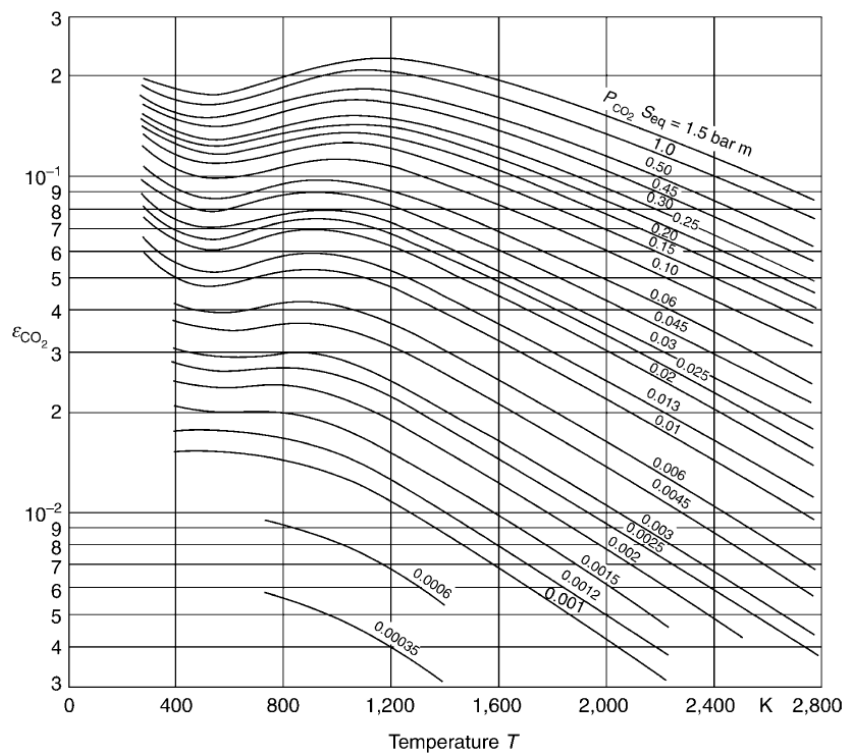
Figure 4.6: Emissivity ε_{CO_2} of carbon dioxide at a total pressure of 1 bar as a function of temperature and the product of $P_{CO_2} \cdot s$ [46].
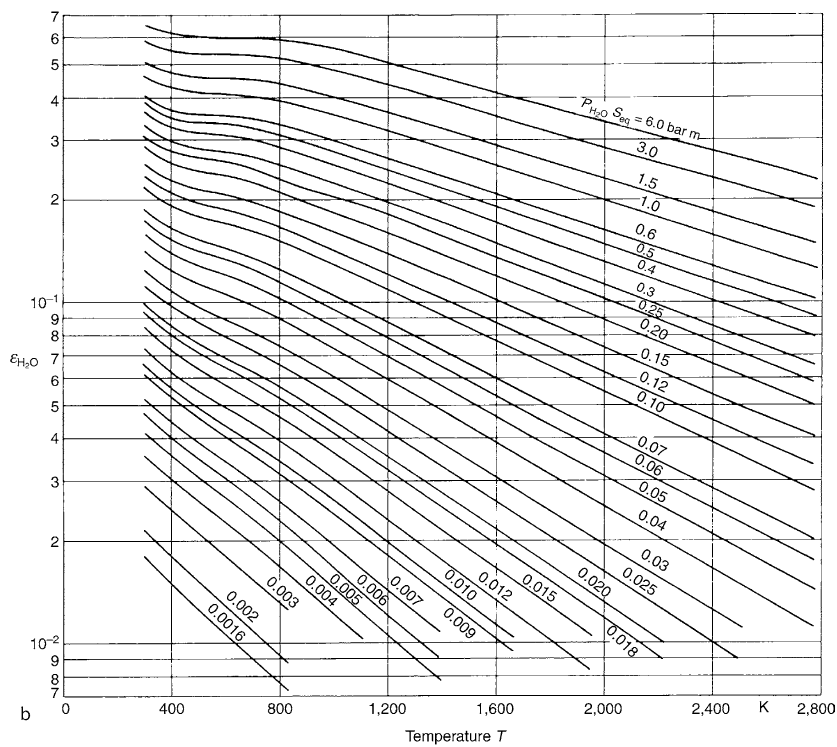
Figure 4.7: Emissivity ε_{H_2O} of water vapor at a total pressure of 1 bar as a function of temperature and the product $P_{H_2O} \cdot s$ [46].

The general form of change in radiative heat transfer between gas and solid is represented in Eq. 4.23. This change depends on the elementary area and it is a function of the length

$$dQ_r = \frac{\varepsilon \sigma A_t}{L_k} \left(T_g^4 - T_s^4\right) dz. \tag{4.23}$$

The effective emissivity between the gas mixture and solid material is calculated according to Eq. 4.24

$$\varepsilon = \frac{1}{\dfrac{1}{\varepsilon_s} + \dfrac{1}{\varepsilon_g} - 1}. \tag{4.24}$$

Where
T_g, the temperature of gas,
T_s, the temperature of solid,
ε, the effective emissivity, and
ε_s, the emissivity of solid material.

Solving Eq. 3.19 and Eq. 4.23 together, the following equation for the change in radiative heat transfer is obtained

$$dQ_r = \alpha_r A_t \left(T_g - T_s\right) dZ. \tag{4.25}$$

Where
α_r, the radiative heat transfer coefficient.

The following equation represents one of the approximated forms of the radiative heat transfer coefficient as a function of effective emissivity and gas and solid temperatures

$$\alpha_r = \varepsilon \sigma T_g^3 \left[1 + \left(\frac{T_s}{T_g}\right) + \left(\frac{T_s}{T_g}\right)^2 + \left(\frac{T_s}{T_g}\right)^3\right]. \tag{4.26}$$

4.4.3   Solid to solid radiation

Radiation from surface to another depends on the orientation relative to each other. Therefore the view factor must be determined. In special geometrical cases, the view factor is tabulated for many technical situations. In other arbitrary cases in the vitrified clay kiln, some views factors have to be explained. Figure 4.1 shows the arrangements of vitrified clay pipes and the kiln furniture arrangements so the view factor could be explained for such arrangements. The following sections describe these different view factors in the illustrated vitrified clay kiln.

- **Fire clay plate to plate view factor :**

    The fire clay plate is placed on the kiln car. According to the expected temperature difference between the fire clay plate and the plate, there is heat transferred by radiation. In Fig. 4.8, the fire clay plate is parallel to the plate. From heat transfer
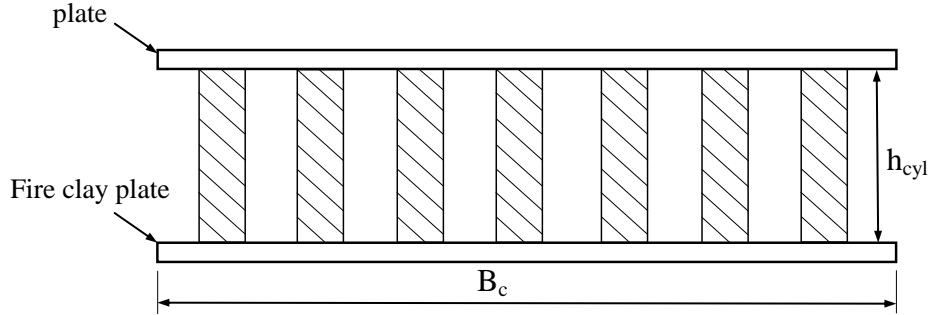
Figure 4.8: Schematic description of the kiln furniture.

basics with some replacements by the shown dimensions, the view factor between two parallel plates is represents by Eq. 4.27 [40].

$$F_{fc \to pl} = \left[1 + \left(\frac{h_{cyl}}{B_c} \right)^2 \right]^{1/2} - \left(\frac{h_{cyl}}{B_c} \right) \tag{4.27}$$

Where
B_c, the kiln car wide,
h_{cyl}, the cylinder height, and
$F_{fc \to pl}$, the view factor between fire clay plate and plate.

- **Cylinder to plate view factor :**

  Referring to the vitrified clay tunnel kiln Fig. 4.2, there is an obvious case of cylinder sited on a plate. Now, it is required to obtain the view factor for this case. Figure 4.9 [50] shows such a case, the figure represents some dimensions which are used to calculate the view factor. Equation 4.28 demonstrates the symbols related to the geometry, these symbols are used in view factor calculation. Equation 4.29 [50] represents the view factor from cylinder to plate.
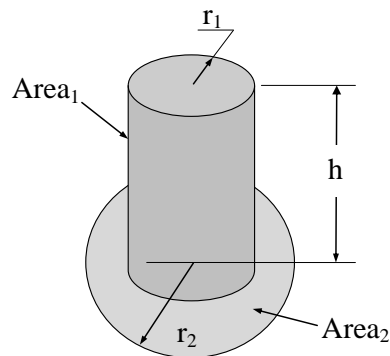
Figure 4.9: View factor from outer surface of cylinder to disk at the end of cylinder [50].

$$R_1 = \frac{r_1}{r_2};$$

$$H_1 = \frac{h}{r_2};$$

$$A_1 = H_1{}^2 + R_1{}^2 - 1; \tag{4.28}$$

$$B_1 = H_1{}^2 - R_1{}^2 + 1$$

$$
\begin{aligned}
F_{cyl \to pl} = \ & \frac{B_1}{8R_1 H_1} + \frac{1}{2\pi} \left\{ \arccos\left(\frac{A_1}{B_1}\right) \right. \\
& \left. - \left[\frac{1}{2H_1} \left[\frac{(A_1 + 2)^2}{R_1^2} - 4 \right]^{1/2} \arccos\left(\frac{A_1 R_1}{B_1}\right) \right] - \frac{A_1}{2R_1 H_1} \arcsin R_1 \right\}
\end{aligned}
\tag{4.29}
$$

Where
$F_{cyl \to pl}$, the view factor from the cylinder to the plate.

According to the vitrified clay tunnel kiln schematic description, there are two cases which will be described in the following two sections.

1. **Supported cylinder to plate view factor :**

   The supported cylinders in the kiln furniture structure radiate heat to the plate. Figure 4.9 demonstrates the same geometrical representation between cylinder and plate. Therefore, the view factor equation between the supported cylinder and plate is the same as in equation 4.29.

2. **Plate to pipes view factor :**

   Due to temperature deference between the plate and the vitrified clay pipes, the plate radiates heat to the pipes. In order to calculate the view factor from the plate to the pipes, the view from vitrified clay pipes to plate is calculated similarly as stated in equation 4.29. Then from the reciprocity relation the view factor from the plate to vitrified clay pipe is obtained as shown in Eq. 4.30

$$F_{pl \to p} = \frac{A_p}{A_{pl2}} \, F_{p \to pl}. \tag{4.30}$$

   Wherein
   $F_{pl \to p}$, the view factor from the plate to vitrified clay pipe,
   A_p, the surface area of vitrified clay pipes, and
   A_{pl2}, the upper surface area of the plate.

   $F_{p \to pl}$, the view factor from the vitrified clay pipe to the plate. Regarding the calculation of this view factor; $r_1 = D/2$, $r_2 = S_D/2$ and $h = H_p$.

The local view factor is determined according to Eq. 4.31. Figure 4.10 shows the view factors from plate to pipe, from pipe to plate, and the local view factor from the plate to the pipe. Furthermore, Fig. 4.11 shows the local view factor from the pipe to plate with logarithmic scale

$$F_{local} = \frac{d(F_{pl \rightarrow p} H_p)}{dH_p}. \tag{4.31}$$
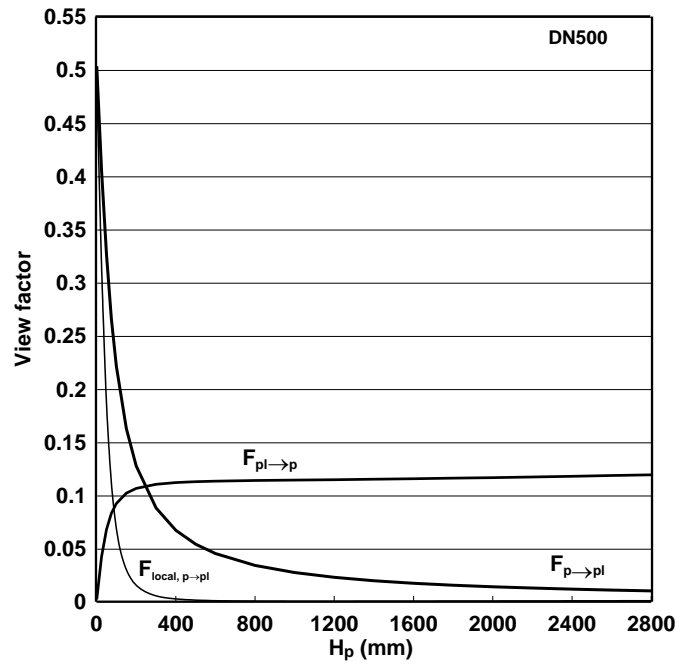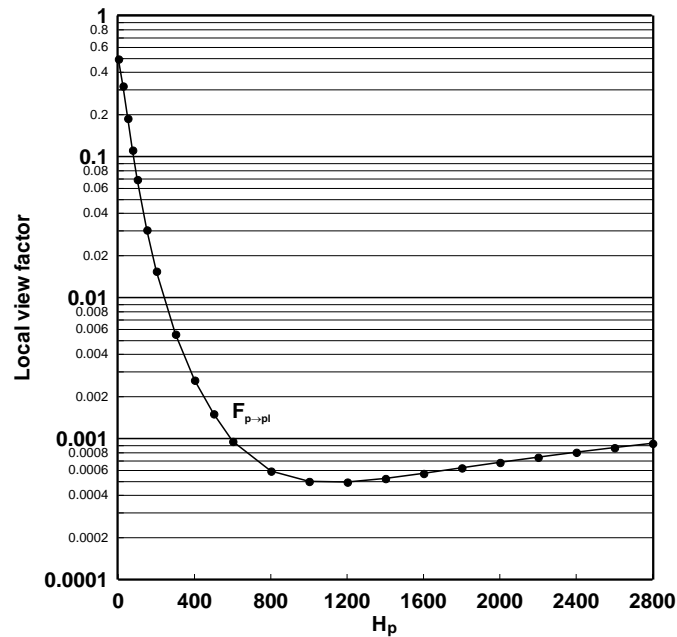

Figure 4.10: View factors between pipe and plate.

Figure 4.11: Local view factor.

4.4.4 Radiative heat transfer determination

To determine the radiative heat exchange between two surfaces two main types of resistance have to be determined. The first is surface resistance which depends on the surface emissivity. The second is the space resistance which depends on the shape of each surface and the view factor between each other. The following equation demonstrates the effective emissivity for such a case

$$\varepsilon_{s1 \to s2} = \frac{1}{\left(\frac{1 - \varepsilon_{s1}}{\varepsilon_{s1}} + \frac{1}{F_{s1 \to s2}} + \frac{A_{s1}}{A_{s2}} \left(\frac{1 - \varepsilon_{s2}}{\varepsilon_{s2}} \right) \right)}. \tag{4.32}$$

Where
s1, refers to surface one, and
s2, refers to second surface.

Consequently, the radiative heat exchange between the two surfaces is represented as in the following general equation :

$$d\dot{Q}_{r_{s1 \to s2}} = \alpha_{r_{s1 \to s2}} A_{s1} \left(T_{s1} - T_{s2} \right) dZ \tag{4.33}$$

Therefore, radiative heat transfer coefficient is represented as

$$\alpha_{r_{s1 \to s2}} = \varepsilon_{s1 \to s2} \sigma T_{s1}^3 \left[1 + \left(\frac{T_{s2}}{T_{s1}} \right) + \left(\frac{T_{s2}}{T_{s1}} \right)^2 + \left(\frac{T_{s2}}{T_{s1}} \right)^3 \right]. \tag{4.34}$$

4.5 Simple case analysis for pipes only

In this section the solution is obtained for only the vitrified clay pipes which means that all the gases pass through the pipes. In the schematic description of the kiln shown in Fig. 4.2, the case looks like case "C", but with $L_f = 35m$. So that Eq. 3.22 represents the ODE for solid in the two zones (preheating, burning). The gas equation depends on the zone. Equation 3.17 is used for the preheating zone. Equation 3.52 represents the gas equation for the firing zone.

Figure 4.12 illustrates the energy consumption which is obtained from the bvp4c program. The figure shows the energy consumption as a function of Stanton number for different excess air numbers. In Fig. 4.12 it is obvious that for constant excess air number, the energy consumption decreases as Stanton number increases. The trend is the same for any excess air number. As a consequence, from the figure a little increase in heat transfer results in a big decrease of E_s for same excess air number. Moreover, the figure shows also that as excess air number increases the energy consumption increases for the same Stanton number. The shadow part in the figure represents the range of energy consumption in industry.

The heat transfer coefficient is calculated according to the following equation:

$$\alpha = \frac{St_s \dot{M}_s c_s}{A_t} \tag{4.35}$$
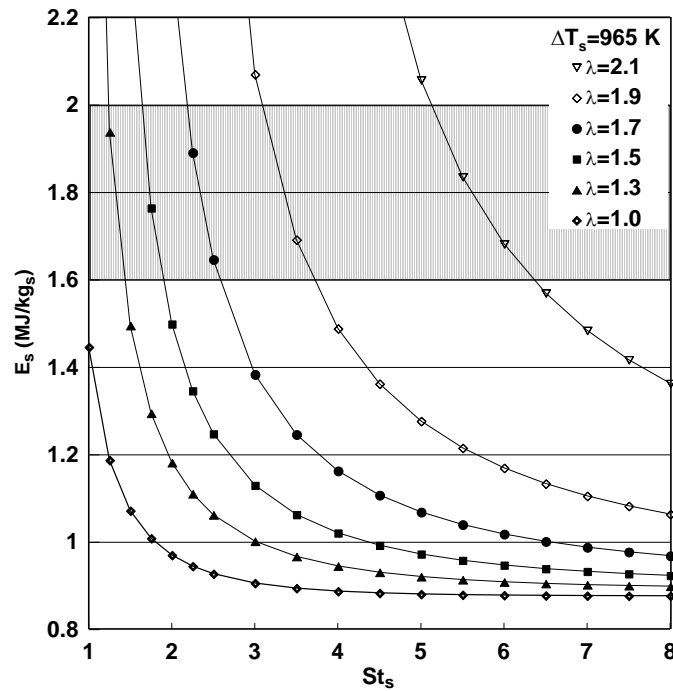
Figure 4.12: Energy consumption of simple case analysis for pipes only.

Then, from this equation and the information from table 4.1, the heat transfer coefficient is calculated for each Stanton number. Table 4.4 shows the heat transfer coefficient related to each Stanton number with the energy consumption in the shadow area. The heat transfer coefficient increases by about 76 % if the excess air number changes from 1.3 to 2.1 therefore Stanton changes from 1.3 to 5.5. Figure 4.13 shows the temperature

Table 4.4: Some results from the calculations

λ	St_s	$\alpha(\text{W}/(m^2\cdot\text{K}))$	E (MJ/kg_s)	Ω
1.3	1.3	0.724	1.8112	1.1383
1.5	1.8	1	1.696	1.2227
1.7	2.5	1.4	1.6456	1.3385
1.9	3.5	1.9	1.691	1.5318
2.1	5.5	3.1	1.835	1.832

profiles for different excess air numbers which stated in table 4.1. The results are all in the shadow range of energy consumption. In Fig. 4.13, the temperature profile slope for the gas changes from firing zone to preheating zone. The influence on the solid temperature is weak. The figure shows that, the lower the excess air number is the higher the energy consumption which results in a higher flue gas temperature.

Figure 4.14 shows the effect of Stanton number on temperature distribution for constant excess air number. Moreover, the results are all in the shadow range of energy consumption. In the figure, the lower the Stanton number the higher the energy consumption which results in a higher flue gas temperature. The values of energy consumption are illustrated in Fig. 4.12. The temperature of the solid is nearly linear along the two zones and there is approximately no difference between them because of

the small change in Stanton number.
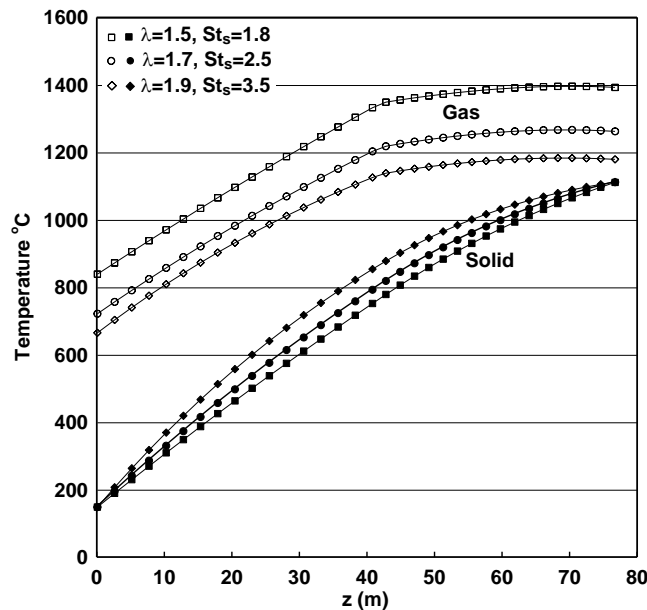
Figure 4.13: Temperature profile with same energy consumption.
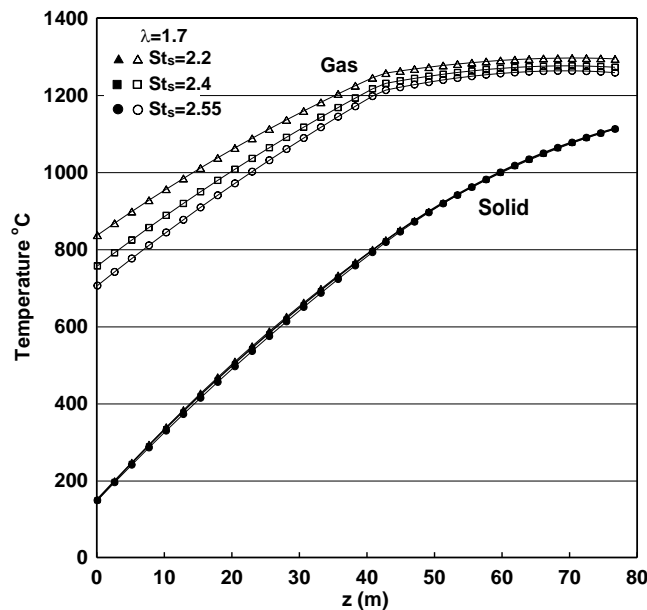
Figure 4.14: Temperature profile with excess air number of $\lambda = 1.7$.

4.6 Heat transfer analysis results

Figure 4.15 shows the temperature profiles for gas and solid due to convective heat transfer analysis. The figure demonstrates that the excess air number should have a higher value to obtain the results. In the figure, the temperature of gas and solid increase sharply at the entrance and weaker at the end of the firing zone.

Figure 4.16 shows the convective heat transfer coefficient α along the kiln. The heat transfer coefficient increases as the firing length increases. This increase is due to the increase of the mass flow of gas and as a result increasing of Reynolds number. At the end of burning zone there is no more addition of gases, so that the maximum amount of gases passes through the preheating zone. Therefore, the heat transfer coefficient is nearly constant along the preheating zone.
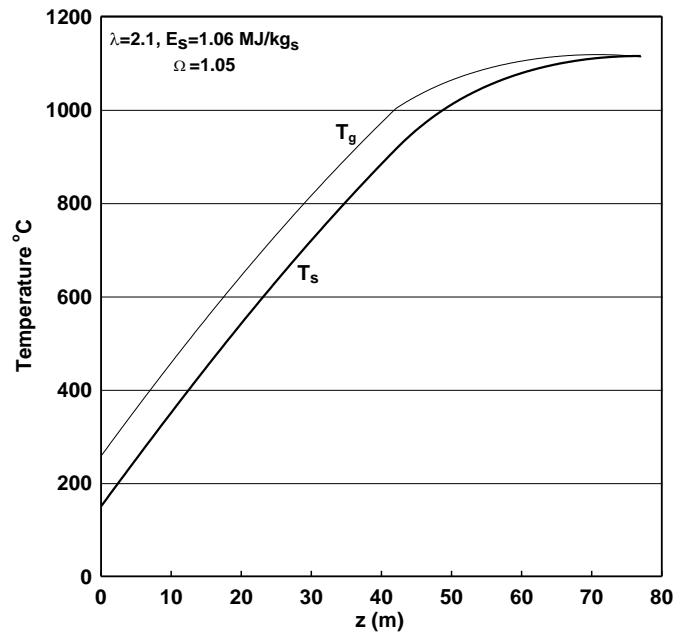
Figure 4.15: Temperature profile along the kiln.
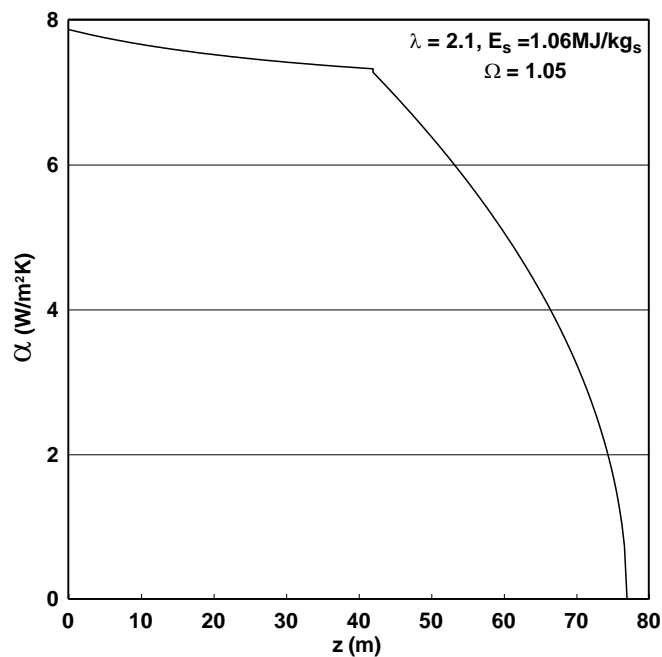
Figure 4.16: Convective heat transfer coefficient α along the kiln.

Chapter 5

Vitrified Clay Pipes Analysis

5.1 Introduction

This chapter focuses on obtaining the ordinary differential equations (ODEs) which are used to draw the temperature profiles for the vitrified clay pipes kiln along the burning and preheating zones. Therefore, the convective heat transfer and the radiative heat transfer are calculated to obtain these ODEs. The foregoing assumptions for case "B" are taken into consideration during the calculations. The analysis is divided into two main sections, burning zone analysis and preheating zone analysis. These analyses are described in the following sections.

5.2 Burning zone analysis

According to the last description of the gas streams, the following sections describe the analysis for both convective and radiative heat transfer. The analysis is related to solid arrangements and the flow of the gases.

5.2.1 ODE for first gas stream (gas$_I$)

As described before the gas distribution equation along the firing length is represented by Eq. 3.44. Moreover, the equation of the first gas stream which passes across the supported cylinders (gas$_I$) is expressed as

$$\dot{M}_{g_1}(z) = \frac{(1-f)\dot{M}_{g,max}L_k}{L_f}(1-Z).$$

(5.1)

Where
f, represents the percentage of the gas which escapes to heat up the vitrified clay pipes.

The calculation steps to obtain the ordinary differential equation for gas$_I$ (ODE) are the same as described in chapter 3. The change in gas enthalpy flow is expressed by equation 3.48. Then by applying the energy balance with neglecting heat loss as stated in the chapter 3, the following equation is obtained.

$$d\dot{H}_g = d\dot{Q}_{g1\rightarrow pl} + d\dot{Q}_{g1\rightarrow fc} + d\dot{Q}_{g1\rightarrow cyl} + d\dot{H}_{in}$$

(5.2)

Where the enthalpy flow input due to combustion of fuel is represented by equation 3.49.

In Eq. 5.2 there are three terms representing the heat transfer. Each term includes convection and radiation. Therefore, the following subsection shows the details of each term to obtain the ODE for gas_I.

- **Convective and radiative heat transfer calculations**

From Fig. 5.1 which shows the arrangement of the supported cylinders, the first gas stream (gas_I) passes across the supported cylinders and the heat is transferred by convection. The heat transfer coefficient is calculated according to Eq. 4.12. Therefore, the following equation represents the convective heat transfer coefficient for gas_I

$$\alpha_1 = \frac{Nu\lambda_{g1}}{d_{cyl}}. \tag{5.3}$$

Where
λ_{g1}, the thermal conductivity of gas_I,
α_1, the convective heat transfer coefficient for gas_I in the burning zone,
d_{cyl}, cylinder diameter, and
Nu, Nusselt number.

Nusselt number is calculated from the analysis in chapter 4 from Eq. 4.14. The calculation is based on the diameter of the supported cylinder. The change in convective heat transfer is calculated according to Eq. 4.13.
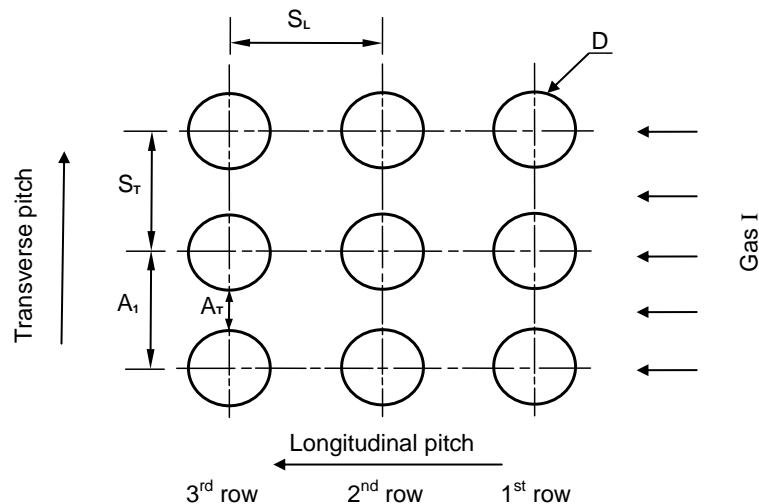

Figure 5.1: Schematic description for the Supported cylinders arrangement in the kiln furniture.

In addition to convection, the radiation takes place in the calculations according to high temperature of the existing gases. The gas which exists between the kiln furniture structures radiates heat to kiln furniture (transportation materials). Moreover, the

furniture structures which are shown in Fig. 4.1 and Fig. 5.1 are taken into consideration during the calculations. The gases used in radiation calculation are carbon dioxide and water vapor. Therefore, the total emissivity of carbon dioxide and water vapor mixture is calculated according to the approximated Eq. 4.22 [48]. Then, the effective emissivity between the gas and each solid surface is calculated according to Eq. 4.24. So, the effective emissivities between gas_I and fire clay plate, plate and supported cylinders are obtained as

$$\varepsilon_1 = \frac{1}{\dfrac{1}{\varepsilon_{pl}} + \dfrac{1}{\varepsilon_{g1}} - 1} \tag{5.4}$$

$$\varepsilon_2 = \frac{1}{\dfrac{1}{\varepsilon_{fc}} + \dfrac{1}{\varepsilon_{g1}} - 1} \tag{5.5}$$

$$\varepsilon_3 = \frac{1}{\dfrac{1}{\varepsilon_{cyl}} + \dfrac{1}{\varepsilon_{g1}} - 1}. \tag{5.6}$$

Where
ε_1, ε_2, and ε_3 are the effective emissivities between gas_I and plate, fire clay plate, and supported cylinders respectively, and
ε_{g1}, the total emissivity of the first gas stream (gas_I) in the burning zone.

The total heat exchange between gas and its surrounding solids is calculated as

$$d\dot{Q}_{g \to s} = d\dot{Q}_r + d\dot{Q}_{conv}. \tag{5.7}$$

The forgoing two equations 4.13 and 4.25 are used for the convective and radiative heat exchange between gas_I and the surrounded solid surface area. Therefore, from Fig. 4.1 the following equations represent the heat exchange terms between gas_I and its surrounded solid based on surface area.

1. **Lower surface of plate**

$$d\dot{Q}_{g1 \to pl} = (\alpha_1 + \alpha_{r_1})A_{pl1}(T_{g_1} - T_{pl})dZ \tag{5.8}$$

   Where
   A_{pl1}, the lower surface area of the plate.

2. **Fire clay plate**

$$d\dot{Q}_{g1 \to fc} = (\alpha_1 + \alpha_{r_2})A_{fc}(T_{g_1} - T_{fc})dZ \tag{5.9}$$

   Where
   A_{fc}, the surface area of the fire clay plate.

3. **Supported cylinders**

$$d\dot{Q}_{g1 \to cyl} = (\alpha_1 + \alpha_{r_3})A_{cyl}(T_{g_1} - T_{cyl})dZ \tag{5.10}$$

   Where
   A_{cyl}, the surface area of the supported cylinders.

The three symbols α_{r_1}, α_{r_2}, and α_{r_3} are the radiative heat transfer coefficients between gas_I and plate, fire clay plate, and supported cylinders respectively. The radiative heat transfer coefficients are calculated according to Eq. 4.26.

By replacing Eqs. 3.48, 3.49, 5.8, 5.9 and 5.10 in Eq. 5.2, the following new first order ordinary differential equation (ODE) for gas_I is obtained as

$$(1-Z)\frac{dT_{g_1}}{dZ} = \frac{L_f}{\dot{M}_{g,max}c_{pg_1}L_k}\{A_{pl1}(\alpha_1+\alpha_{r_1})(T_{g_1}-T_{pl}) + A_{fc}(\alpha_1+\alpha_{r_2})(T_{g_1}-T_{fc})$$

$$(5.11)$$

$$+A_{cyl}(\alpha_1+\alpha_{r_3})(T_{g_1}-T_{cyl})\} - ((1-f)T_{ad}-T_{g_1}).$$

5.2.2   ODE for second gas stream (gas_{II})

The vitrified clay pipes must be heated until the desired sintering temperature is reached. Therefore, from the description of the kiln furniture there is an amount of gas which escapes to heat the pipes. The equation which describes the escaped amount is represented as

$$\dot{M}_{g2}(Z) = \frac{f\dot{M}_{g,max}L_k}{L_f}(1-Z).$$

$$(5.12)$$

Where
f, represents the percentage of the gas which escapes to heat up the vitrified clay pipes.

Moreover, this gas amount passes across the vitrified clay pipes and is used to determine Reynolds number and therefore Nusselt number. The change in gas enthalpy flow for gas_{II} is expressed as stated in equation 3.48. Then by applying the energy balance with neglecting heat loss as before, the following equation is obtained

$$d\dot{H}_{g2} = d\dot{Q}_{g2\rightarrow p} + d\dot{H}_{in_2}.$$

$$(5.13)$$

The enthalpy flow input $d\dot{H}_{in_2}$ in the last equation is the amount of gases which escaped from the space between the kiln walls and plate to heat the vitrified clay pipes. This amount is the heat source and is represented as

$$d\dot{H}_{in_2} = -\frac{f\dot{M}_{g,max}c_{pg_1}T_{ad}L_k}{L_f}dZ.$$

$$(5.14)$$

A negative sign is applied in $d\dot{H}_{in_2}$ because the addition is in the opposite direction of axes z.

Regarding the second term in Eq. 5.13 which includes convection and radiation, the following subsection shows how to obtain it and consequently the ODE for gas_{II}.

- **Convective and radiative heat transfer calculations**

The arrangement of the vitrified clay pipes in the kiln is shown in Fig. 5.2. The second gas stream (gas_{II}) passes across the pipes and the heat is transferred by convection. The convective heat transfer coefficient is calculated according to Eq. 4.12. Therefore, for the vitrified clay pipes the convective heat transfer coefficient is represented as

$$\alpha_2 = \frac{Nu\lambda_{g2}}{D_p}. \tag{5.15}$$

Where
λ_{g2}, the thermal conductivity of gas_{II},
α_2, the convective heat transfer coefficient for gas_{II} in the burning zone,
D_p, vitrified clay pipe outer diameter, and
Nu, Nusselt number.

Nusselt number is calculated from the analysis in chapter 4 from Eq. 4.14 and based on pipe outer diameter of the pipe. The change in convective heat transfer is calculated according to Eq. 4.13.
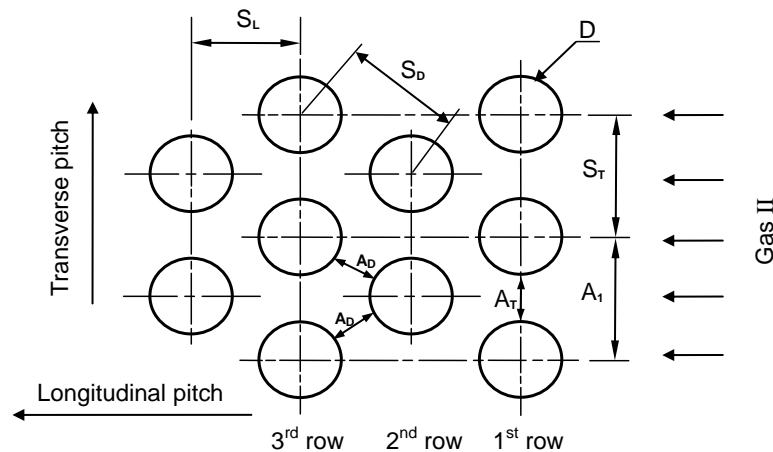
Figure 5.2: Schematic description for pipes arrangement on kiln car.

The amount of gases which escapes from the space between the kiln walls and plate has a high temperature and radiates heat to the pipes. This amount is called as before gas_{II} which exists around the vitrified clay pipes as shown in Figures. 4.1 and 5.2. The gases used in calculations are considered as gas mixture of carbon dioxide and water vapor. Therefore, the total emissivity of carbon dioxide and water vapor mixture is calculated according to the approximated Eq. 4.22 [48]. Then, the effective emissivity between the gas and pipes surface is calculated according to Eq. 4.24. The effective emissivity between gas_{II} and vitrified clay pipes is represented as

$$\varepsilon_4 = \frac{1}{\dfrac{1}{\varepsilon_p} + \dfrac{1}{\varepsilon_{g2}} - 1}. \tag{5.16}$$

Where

ε_4, the effective emissivity between gas_{II} and vitrified clay pipes, and

ε_{g2}, the total emissivity of the second gas stream in the burning zone.

The foregoing two equations Eq. 4.13 and Eq. 4.25 are used for the convective and radiative heat exchange between gas_{II} and the surrounded pipes surface area. The equation which represents the heat exchange between gas_{II} and the vitrified clay pipes is

$$d\dot{Q}_{g2 \to p} = (\alpha_2 + \alpha_{r_4})A_p(T_{g2} - T_p)dZ. \tag{5.17}$$

Where

A_p, the total surface area of the vitrified clay pipes, and

α_{r_4}, the radiative heat transfer coefficient between gas_{II} and vitrified clay pipes.

By replacing Eqs. 3.48, 5.14 and 5.17 in Eq. 5.13, the following new first order ordinary differential equation (ODE) for gas_{II} is obtained

$$(1 - Z)\frac{dT_{g2}}{dZ} = \frac{A_p L_f}{f \dot{M}_{g,max} c_{pg_2} L_k}(\alpha_2 + \alpha_{r_4})(T_{g2} - T_p) - \left(\frac{c_{pg_1}}{c_{pg_2}}T_{ad} - T_{g2}\right). \tag{5.18}$$

5.2.3 ODEs for solids

There are four solids which are considered in the vitrified clay pipes kiln calculations. These four solids are plate, supported cylinders, fire clay plate, and the vitrified clay pipes itself. The vitrified clay pipes are subjected to the second gas stream gas_{II}. The other three solids are subjected to the first gas stream gas_I. Therefore, to obtain the ODE for each solid material the contact gas must be considered for convective and radiative heat exchange calculations; moreover, the heat exchange between the solids themselves. The general solid enthalpy flow change equation is expressed by equation 3.20. In the equation, s, represents the solid material and it is related to the material name.

The mass flow of solid for each solid material in the kiln is calculated related to the data in table 4.1 as

$$\dot{M}_s = N_{cars}\rho_s V_s Load. \tag{5.19}$$

Where

ρ_s, the density of the solid material,

N_{cars}, number of cars in the kiln,

Load, the load inside the kiln (car/day), and

V_s, the volume of solid material per car.

Then the general form of the first order ordinary differential equation ODE for solid is represented as

$$\dot{M}_s c_s dT_s = d\dot{Q}_{g \to s} + d\dot{Q}_{s1 \to s2}. \tag{5.20}$$

In the foregoing equation, there are two terms in the right hand side, each term is calculated according to the heat exchange mechanism. The first term on the right hand side $(d\dot{Q}_{g \to s})$ includes both convective and radiative heat exchange as stated in Eq. 5.7. The

second term $(d\dot{Q}_{s1\to s2})$ is related to solid to solid radiation. The following section shows in detail, how to obtain the (ODE) for each of the four solids material in the vitrified clay pipes kiln.

- **Convective and radiative heat transfer for solids**

The convective heat transfer coefficients from both gas streams $(gas_I$ and $gas_{II})$ are as described before $(\alpha_1$ and $\alpha_2)$.

There are additional terms in the radiative heat transfer calculations which are related to the solid to solid radiation. These additional terms include radiation from the fire clay plate to the plate, radiation from the supported cylinders to the plate, and radiation from the plate to the vitrified clay pipes. Solid to solid radiation depends on view factor determination. As illustrated before in the foregoing chapter, the different view factors have been mentioned in that chapter. So that, referring to these view factors the solid to solid radiation could be obtained as following.

- **Fire clay plate to plate radiation**

  The effective emissivity between the fire clay plate and the plate is calculated according to Eq. 4.32 and it is expressed as

  $$\varepsilon_{fc\to pl} = \frac{1}{\left(\dfrac{1 - \varepsilon_{fc}}{\varepsilon_{fc}} + \dfrac{1}{F_{fc\to pl}} + \dfrac{A_{fc}}{A_{pl1}}\left(\dfrac{1 - \varepsilon_{pl}}{\varepsilon_{pl}}\right)\right)}. \tag{5.21}$$

  Where
  $F_{fc\to pl}$, the view factor between fire clay plate and plate.

  The view factor is determined from Eq. 4.27. The radiative heat transfer is determined according to Eq. 4.33 in which the radiative heat transfer coefficient is determined according to Eq. 4.34. Therefore, the equation which represents the radiative heat transfer between the fire clay plate and the plate is

  $$d\dot{Q}_{r_{fc\to pl}} = \alpha_{r_{fc\to pl}} A_{fc}(T_{fc} - T_{pl})dZ. \tag{5.22}$$

  Where
  $\alpha_{r_{fc\to pl}}$, the radiative heat transfer coefficient between fire clay plate and plate.

- **Supported cylinder to plate radiation**

  The effective emissivity between the supported cylinders and the plate is calculated according to Eq. 4.32 and it is expressed as

  $$\varepsilon_{cyl\to pl} = \frac{1}{\left(\dfrac{1 - \varepsilon_{cyl}}{\varepsilon_{cyl}} + \dfrac{1}{F_{cyl\to pl}} + \dfrac{A_{cyl}}{A_{pl1}}\left(\dfrac{1 - \varepsilon_{pl}}{\varepsilon_{pl}}\right)\right)}. \tag{5.23}$$

  Where $F_{cyl\to pl}$, the view factor between supported cylinder and perforated plate.

The view factor is determined from Eq. 4.29. The radiative heat transfer is determined according to Eq. 4.33 in which the radiative heat transfer coefficient is determined according to Eq. 4.34. Therefore, the equation which represents the radiative heat transfer between supported cylinders and plate is expressed as

$$d\dot{Q}_{r_{cyl \to pl}} = \alpha_{r_{cyl \to pl}} A_{cyl}(T_{cyl} - T_{pl})dZ. \tag{5.24}$$

Where
$\alpha_{r_{cyl \to pl}}$, the radiative heat transfer coefficient between supported cylinders and plate.

- **Plate to vitrified clay pipes radiation**

  Additionally, the effective emissivity between plate and vitrified clay pipes is calculated according to Eq. 4.32 and it is expressed as

$$\varepsilon_{pl \to p} = \frac{1}{\left(\dfrac{1 - \varepsilon_{pl}}{\varepsilon_{pl}} + \dfrac{1}{F_{pl \to p}} + \dfrac{A_{pl2}}{A_p} \left(\dfrac{1 - \varepsilon_p}{\varepsilon_p} \right) \right)}. \tag{5.25}$$

  Where
  $F_{pl \to p}$, the view factor between the plate and the vitrified clay pipes, and
  A_{pl2}, the upper surface area of the plate.

  The view factor, the radiative heat transfer, and the radiative heat transfer coefficient are determined from Eqs. 4.30, 4.33, and 4.34 respectively. Therefore, the equation which represents the radiative heat transfer between the plate and the vitrified clay pipes is expressed as

$$d\dot{Q}_{r_{pl \to p}} = \alpha_{r_{pl \to p}} A_{pl2}(T_{pl} - T_p)dZ. \tag{5.26}$$

  Where
  $\alpha_{r_{pl \to p}}$, the radiative heat transfer coefficient between the plate and the vitrified clay pipes.

The ordinary differential equation for each solid is obtained by replacing the corresponding values of heat exchange in the right hand side of Eq. 5.20. Moreover, for each solid the right hand side contains three parts of heat exchange. The three parts are convective heat transfer from gas to solid, radiative heat transfer according to gas radiation, and solid to solid radiation. These parts are related to each gas and its contact solids and also the solids arrangements as in Figures(4.1 and 4.2). The following equations represent the ODEs for the solids under interest

1. **Plate**

$$\dot{M}_{pl}c_{pl}\frac{dT_{pl}}{dZ} = A_{pl1}(\alpha_1 + \alpha_{r_1})(T_{g_1} - T_{pl}) + \alpha_{r_{fc \to pl}} A_{pl1}(T_{fc} - T_{pl})$$

$$+ \alpha_{r_{cyl \to pl}} A_{cyl}(T_{cyl} - T_{pl}) - \alpha_{r_{pl \to p}} A_{pl2}(T_{pl} - T_p) \tag{5.27}$$

2. **Fire clay plate**

$$\dot{M}_{fc}c_{fc}\frac{dT_{fc}}{dZ} = A_{fc}(\alpha_1 + \alpha_{r_2})(T_{g_1} - T_{fc}) - \alpha_{r_{fc \to pl}}A_{pl1}(T_{fc} - T_{pl}) \qquad (5.28)$$

3. **Supported cylinders**

$$\dot{M}_{cyl}c_{cyl}\frac{dT_{cyl}}{dZ} = A_{cyl}(\alpha_1 + \alpha_{r_3})(T_{g_1} - T_{cyl}) - \alpha_{r_{cyl \to pl}}A_{cyl}(T_{cyl} - T_{pl}) \qquad (5.29)$$

4. **Vitrified clay pipes**

$$\dot{M}_p c_p \frac{dT_p}{dZ} = A_p(\alpha_2 + \alpha_{r_4})(T_{g_2} - T_p) + \alpha_{r_{pl \to p}}A_p(T_{pl} - T_p). \qquad (5.30)$$

5.3 Preheating zone analysis

The hot gas which passes through the burning zone goes directly to the preheating zone to preheat the solids before the burning process. So that, the first gas stream (gas$_I$) passes across the supported cylinders and between the plate and the fire clay plate. The second gas stream (gas$_{II}$) passes across the vitrified clay pipes. Furthermore, the two streams are sucked out from the kiln by blowers. Likewise, by the same method in the burning zone the ODEs for the two gas streams and the solids in the preheating zone are obtained. In this region there is no heat source from combustion gases because the combustion process ends at the end of combustion zone.

5.3.1 ODE for first gas stream (gas$_I$)

In the preheating zone there is no more addition of gases; therefore, the amount of gases is constant along the zone. The gas amount which passes across the supported cylinders is expressed as

$$\dot{M}_{g_1,pre} = (1 - f)\dot{M}_{g,max}. \qquad (5.31)$$

The calculation steps to obtain the ODE for gas$_I$ are the same as described in chapter 3. The change in gas enthalpy flow in the preheating zone is expressed as

$$d\dot{H}_{g_1,pre} = \dot{M}_{g_1,pre}c_{pg_1,pre}dT_{g_1}. \qquad (5.32)$$

Applying the energy balance with neglecting heat loss as stated in the chapter 3, the following equation is obtained

$$d\dot{H}_{g_1,pre} = d\dot{Q}_{g1 \to pl,pre} + d\dot{Q}_{g1 \to fc,pre} + d\dot{Q}_{g1 \to cyl,pre}. \qquad (5.33)$$

In Eq. 5.33, there are three terms represent the heat transfer. Each term includes convection and radiation, the following subsection shows the details of each term to obtain the ODE for gas$_I$.

- **Convective and radiative heat transfer calculations**

Referring to Fig. 5.1 which shows the arrangement of the supported cylinders, and by the same analysis as in the burning zone the convective heat transfer coefficient of gas$_I$ is represented as in equation 5.3.

Nusselt number is calculated from the analysis in chapter 4 from Eq. 4.14 and its calculation is based on the diameter of the supported cylinder. The change in convective heat transfer is calculated according to Eq. 4.13.

The radiation analysis takes place in the preheating zone by the same steps as in the burning zone. Therefore, the total emissivity of carbon dioxide and water vapor mixture is calculated according to the approximated Eq. 4.22 [48]. Then, the effective emissivity between the gas and each solid surface is calculated according to Eq. 4.24. So that, the effective emissivities between gas$_I$ and fire clay plate, plate, and supported cylinders are obtained by the foregoing Eqs. 5.4, 5.5, and 5.6 respectively.

The total heat exchange between gas and its surrounded solids is calculated according to Eq. 5.7. In which Eq. 4.13 and Eq. 4.25 are used for the convective and radiative heat exchange between gas$_I$ and the surrounded solid surface area. Therefore, from Fig. 4.1 the equations which represent the heat exchange terms between gas$_I$ and its surrounded solid (lower surface of plate, fire clay plate, and supported cylinders) based on surface area are the same as 5.8, 5.9, and 5.10 respectively.

The following new first order ordinary differential equation (ODE) for gas$_I$ is obtained by the same steps as in Eq. 5.11.

$$\frac{dT_{g_{1,pre}}}{dZ} = \frac{1}{(1-f)\dot{M}_{g,max}c_{pg_{1,pre}}} \left\{ A_{pl1}(\alpha_3 + \alpha_{r_{1,pre}})(T_{g_1} - T_{pl}) \right.$$

$$\left. + A_{fc}(\alpha_1 + \alpha_{r_{2,pre}})(T_{g_{1,pre}} - T_{fc}) + A_{cyl}(\alpha_1 + \alpha_{r_{3,pre}})(T_{g_1} - T_{cyl}) \right\}$$

$$(5.34)$$

α_3, the convective heat transfer coefficient for gas$_I$ in the preheating zone.
The three symbols $\alpha_{r_{1,pre}}$, $\alpha_{r_{2,pre}}$, and $\alpha_{r_{3,pre}}$, are the radiative heat transfer coefficients between gas$_I$ and plate, fire clay plate, and supported cylinders respectively. The radiative heat transfer coefficients are calculated according to Eq. 4.26.

5.3.2 ODE for second gas stream (gas$_{II}$)

The total amount of the gases which escaped to heat the vitrified clay pipes passes through the preheating zone to preheat the solids before the burning process. The equation which describes the escaped amount is represented as

$$\dot{M}_{g2,pre} = f\dot{M}_{g,max}. \tag{5.35}$$

Where
f, represents the percentage of the gases which escaped to heat up the vitrified clay pipes.

The change in gas enthalpy flow for gas_{II} in the preheating zone is expressed as

$$d\dot{H}_{g2,pre} = \dot{M}_{g2,pre} c_{pg2,pre} dT_{g2,pre}. \tag{5.36}$$

Applying the energy balance with neglecting heat loss as before, the following equation is obtained

$$d\dot{H}_{g2,pre} = d\dot{Q}_{g2\to p,pre}. \tag{5.37}$$

The right hand side in Eq. 5.37 includes convection and radiation. The convective heat transfer coefficient is calculated in the same way as in the burning zone. From the arrangement of the vitrified clay pipes in the kiln as shown in Fig. 5.2, the convective heat transfer coefficient is calculated according to Eq. 4.12. Therefore, the convective heat transfer coefficient is represented as stated before in Eq. 5.15.

Nusselt number is calculated from the analysis in chapter 4 from Eq. 4.14, but its calculation based on outer pipe diameter. Furthermore, the change in convective heat transfer is calculated according to Eq. 4.13.

Besides the convective heat transfer, radiative heat transfer occurs also in the preheating zone between gas_{II} and the vitrified clay pipes. Therefore, the total emissivity of the gas mixture is calculated according to the approximated Eq. 4.22 [48]. Then, the effective emissivity between the gas and pipes surface is calculated according to Eq. 4.24. The effective emissivity between gas_{II} and vitrified clay pipes is expressed as in Eq. 5.16.

Therefore, from this analysis the right hand side of Eq. 5.37 which includes convective and radiative heat transfer between gas_{II} and the surrounded pipes surface area is represented in Eq. 5.17.

The following new first order ordinary differential equation (ODE) for gas_{II} is obtained by the same steps as in Eq. 5.18

$$\frac{dT_{g2,pre}}{dZ} = \frac{A_p}{f\dot{M}_{g,max} c_{pg2,pre}} (\alpha_4 + \alpha_{r4,pre})(T_{g2} - T_p). \tag{5.38}$$

Where
A_p, the total surface area of the vitrified clay pipes,
α_4, the convective heat transfer coefficient for gas_{II} in the burning zone, and
$\alpha_{r4,pre}$, the radiative heat transfer coefficient between gas_{II} and vitrified clay pipes.

5.3.3 ODEs for solids

Likewise the analysis of solids in the preheating zone is the same as in the burning zone. Therefore, the general solid enthalpy flow change equation is represented by Eq. 3.20 and

the general form of the first order ordinary differential equation ODE for solid is expressed by Eq. 5.20. In Eq. 5.20 there are two terms in the right hand side, each term is calculated according to the heat exchange mechanism. The first term in the right hand side ($d\dot{Q}_{g \to s}$) includes both convective and radiative heat exchange as stated in Eq. 5.7. The second term ($d\dot{Q}_{s1 \to s2}$) is related to solid to solid radiation. The following section shows in detail how to obtain the (ODE) for each of the four solids material in vitrified clay pipes kiln.

- **Convective and radiative heat transfer for solids**

The convective heat transfer coefficients from both gas streams (gas_I and gas_{II}) are as described before (α_3 and α_4).

Regarding the radiative heat transfer calculations, the effective emissivities which related to the solid to solid radiation are calculated as in Eqs. 5.21, 5.23, and 5.25 for radiation from the fire clay plate to the plate, radiation from the supported cylinders to the plate, and finally radiation from the plate to the vitrified clay pipes respectively. Consequently, the radiative heat transfer for solid to solid radiation is obtained by Eqs. 5.22, 5.24, and 5.26. The ordinary differential equation for each solid is obtained by replacing the corresponding values of heat exchange in the right hand side of Eq. 5.20. The following equations represent the ODEs for the solids of interest (i.e. plate, fire clay plate, supported cylinders, and vitrified clay pipes)

1. **Plate**

$$\dot{M}_{pl}c_{pl}\frac{dT_{pl}}{dZ} = A_{pl1}(\alpha_3 + \alpha_{r_1,pre})(T_{g_1} - T_{pl}) + \alpha_{r,pre_{fc \to pl}}A_{pl1}(T_{fc} - T_{pl})$$

(5.39)

$$+ \alpha_{r,pre_{cyl \to pl}}A_{cyl}(T_{cyl} - T_{pl}) - \alpha_{r,pre_{pl \to p}}A_{pl2}(T_{pl} - T_p)$$

2. **Fire clay plate**

$$\dot{M}_{fc}c_{fc}\frac{dT_{fc}}{dZ} = A_{fc}(\alpha_3 + \alpha_{r_2,pre})(T_{g_1} - T_{fc}) - \alpha_{r,pre_{fc \to pl}}A_{pl1}(T_{fc} - T_{pl}) \qquad (5.40)$$

3. **Supported cylinders**

$$\dot{M}_{cyl}c_{cyl}\frac{dT_{cyl}}{dZ} = A_{cyl}(\alpha_3 + \alpha_{r_3,pre})(T_{g_1} - T_{cyl}) - \alpha_{r,pre_{cyl \to pl}}A_{cyl}(T_{cyl} - T_{pl}) \quad (5.41)$$

4. **Vitrified clay pipes**

$$\dot{M}_p c_p \frac{dT_p}{dz} = A_p(\alpha_4 + \alpha_{r_4,pre})(T_{g_2} - T_p) + \alpha_{r,pre_{pl \to p}}A_p(T_{pl} - T_p). \qquad (5.42)$$

5.4   Numerical solution results

There is a system of ordinary differential equations (ODEs) for solids and gases for both burning and preheating zones. In the case of vitrified clay pipes, the system consists of six first order (ODEs) for the burning zone and also six (ODEs) for the preheating zone. Equations 5.11, 5.18, 5.27, 5.28, 5.29, and 5.30 are the ODEs for the burning zone. On the other hand Eqs 5.34, 5.38, 5.39, 5.40, 5.41, and 5.42 are the ODEs for the preheating zone. Therefore, it is necessary to solve this system of ODEs equations numerically. In order to solve this system of ODEs equations, algebraic equations with boundary conditions, the MATLAB bvp4c solver is used. The bvp4c solver required six boundary conditions for the solution in which the four solids inlet temperatures ($T_{p,in}$, $T_{pl,in}$, $T_{fc,in}$, and $T_{cyl,in}$) for pipes, plate, fire clay plate, and supported cylinders respectively, then the last two boundary conditions ($T_{p,f}$ and $T_{fc,f}$) are the outlet temperatures of pipes and fire clay plate respectively. The basics of this solver are shown in Appendix (A).

Regarding the previous analysis in chapter 3, there are many numerical results to display the temperature profile for both solid and gas. Furthermore, from the results the temperature profiles for the gases and solids along the two zones, preheating and burning are obtained. Some variables used in solving this system are listed in table 4.1. In this program the outlet temperature of pipes is $T_{p,f}$= 1115°C as a sintering temperature for the vitrified clay pipes production. In addition, the suggested outlet temperature of fire clay plate is $T_{fc,f}$= 1227°C. In the solution for the same excess air number, the iteration is done to obtain the results and to fit the energy balance. The value of f is adjusted and then the iterations are done by changing the energy input until the balance is obtained and then the solution is accepted. Furthermore, the value of f is changed and the sequences are followed again to obtain the solution. The following sections show sample of results obtained from the numerical solution.

5.4.1   Results for radiative heat transfer calculations only

In this section the results are obtained for radiation's calculations only. Therefore, the convective heat transfer coefficient in the ODEs is neglected.

Figure 5.3 illustrates the energy consumption which obtained from the bvp4c program. The energy consumption in the figure is shown as a function of the percentage of gas escaped, f, for different excess air numbers. The figure demonstrates that for constant excess air number, the energy consumption decreases as the escaped percentage of gas increases. The all excess air number the trend remains the same. The figure shows that for some values of f there is no solution for the combined equations with the boundary conditions for some excess air number's values. The figure shows also that as excess air number increases the energy consumption increases for the same f.

Figure 5.4 and 5.5 show the temperature profiles for excess air number λ = 2.1 and f = 15 % and 20 % respectively. These figures demonstrate that the temperature profile of the vitrified clay pipes is nearly linear. From these figures it can be seen the lower the escaped gas is, the higher the energy consumption which results in a higher flue gas temperature. Unfortunately, the temperature profiles for the kiln furniture solids
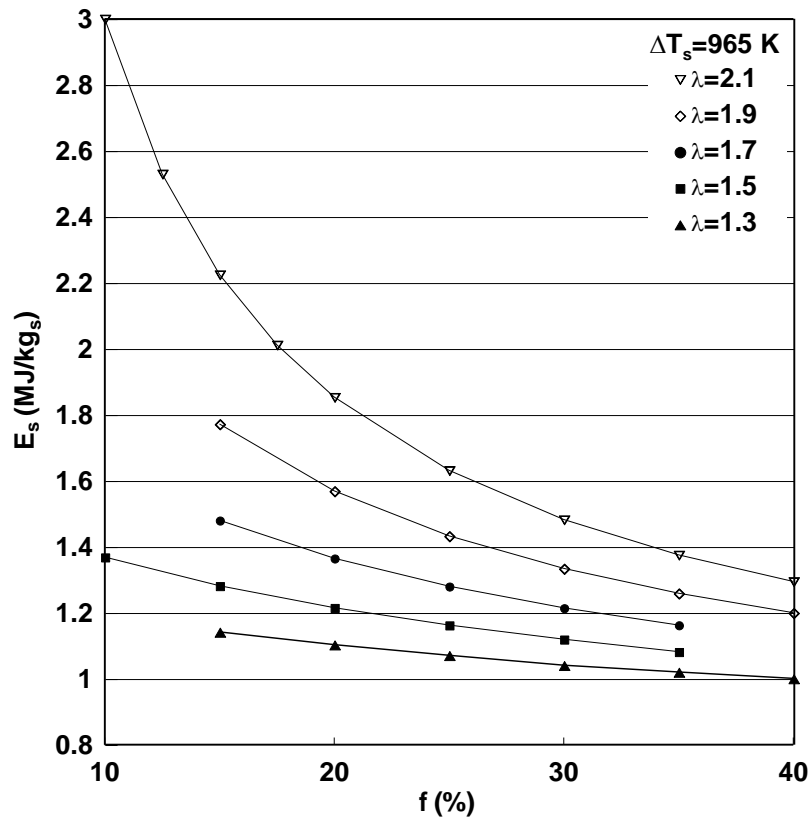
Figure 5.3: Energy consumption for radiation only.

differ from industrial experience. The sharp decreasing in temperature profiles of kiln furniture materials is due to the boundary conditions which are equal to pipes inlet temperature. Also the material has to be heated to an extremely high temperature due to radiation. Moreover, the values of f affect on the temperature profiles of the kiln furniture and the difference between T_{g_1} and T_{g_2}.

Figure 5.6 shows the radiative heat transfer coefficients along the kiln for both gas radiation and solid to solid radiation. In the figure, the heat transfer coefficients decrease as the firing length increases. Therefore, the heat transfer between gas and solid is very high. As a consequence, the temperature profiles of gas and solid are very close to each other as shown in the figure.

Figure 5.7 shows the emissivities of carbon dioxide, ε_{CO2}, water vapor, ε_{H2O}, and gas$_{II}$ emissivity, ε_{g_2}, for excess air number of value $\lambda = 2.1$ and escaped percentage of value f = 20 %.
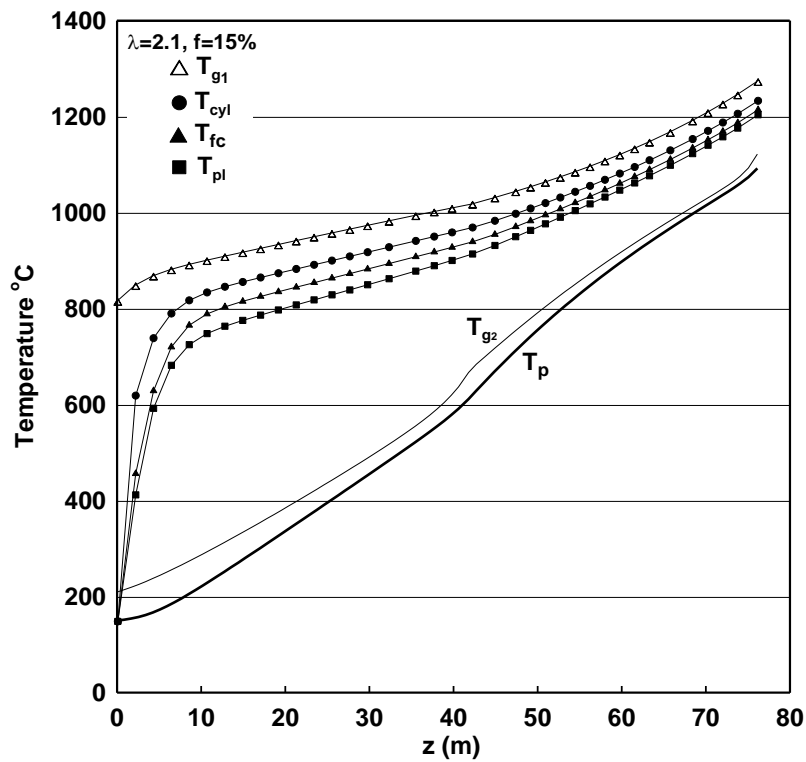
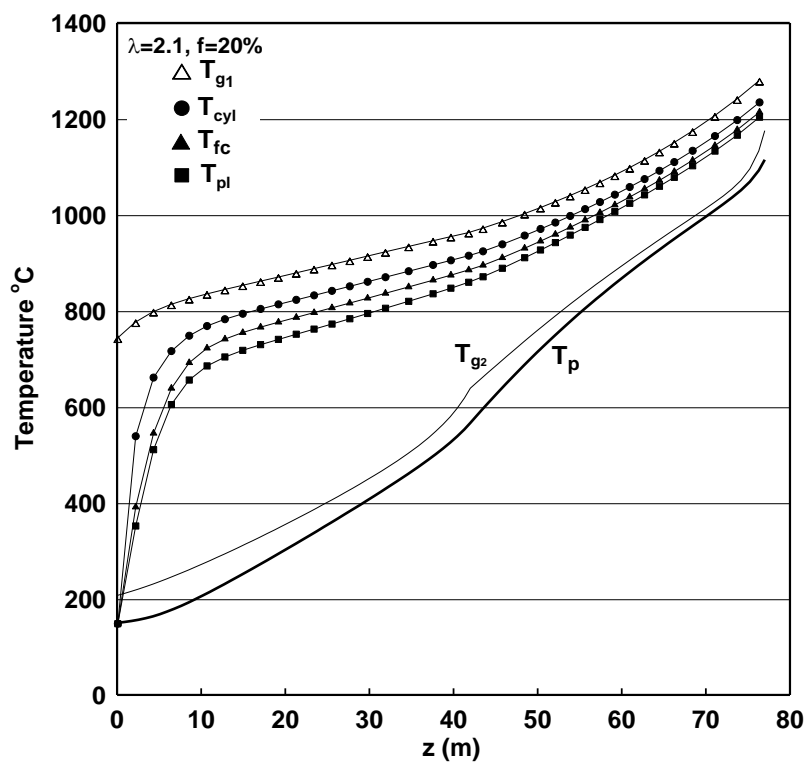Figure 5.4: Temperature profile with excess air number of $\lambda = 2.1$ and f= 15 %.

Figure 5.5: Temperature profile with excess air number of $\lambda = 2.1$ and f= 20 %.
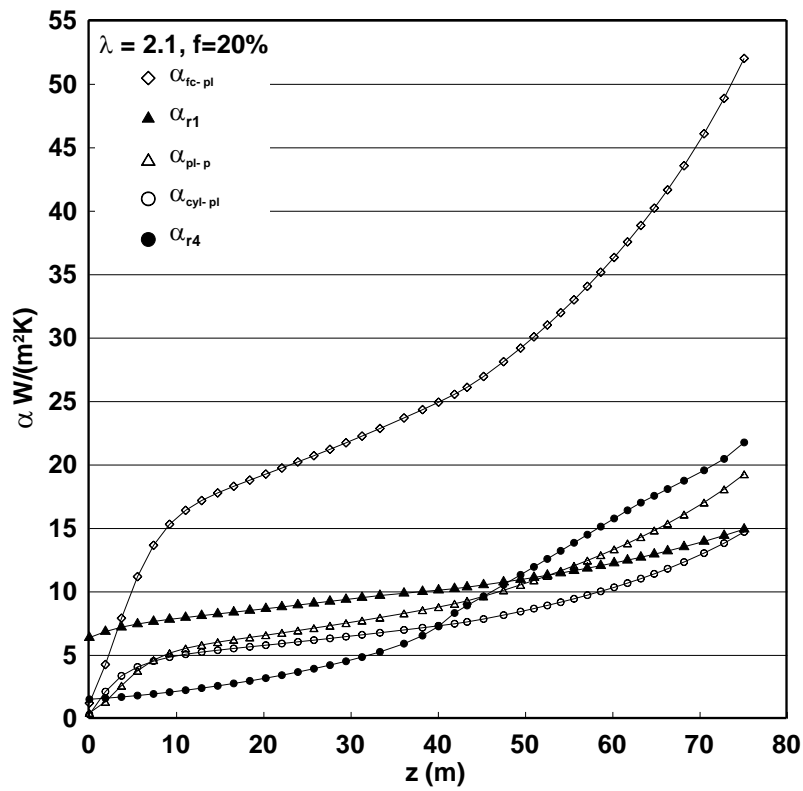
Figure 5.6: Radiative heat transfer coefficient (α_r) along the kiln.

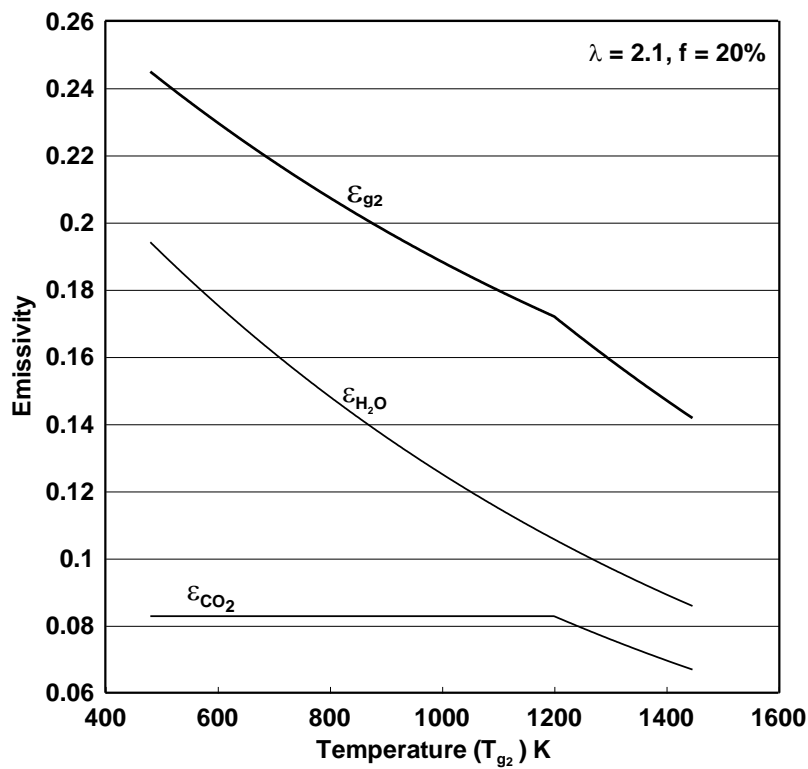Figure 5.7: Emissivities of ε_{CO2} and ε_{H2O}.

5.4.2 Results for all system

This section shows the results which obtained for all the system with convection and radiation calculations.

Figure 5.8 illustrates the energy consumption which obtained from the bvp4c program. The energy consumption in the figure is shown as a function of the percentage of gas escaped f for different excess air numbers. The figure demonstrates that for constant excess air number, the energy consumption decreases as the escaped percentage of gas increases. The trend is the same for any excess air number. The figure shows that for some values of f there is no solution for the combined equations with the boundary conditions for some excess air number's values. The figure demonstrates that as excess air number increases the energy consumption increases for the same f. For lower excess air number values the available results obtained for $25\% < f < 40\%$.
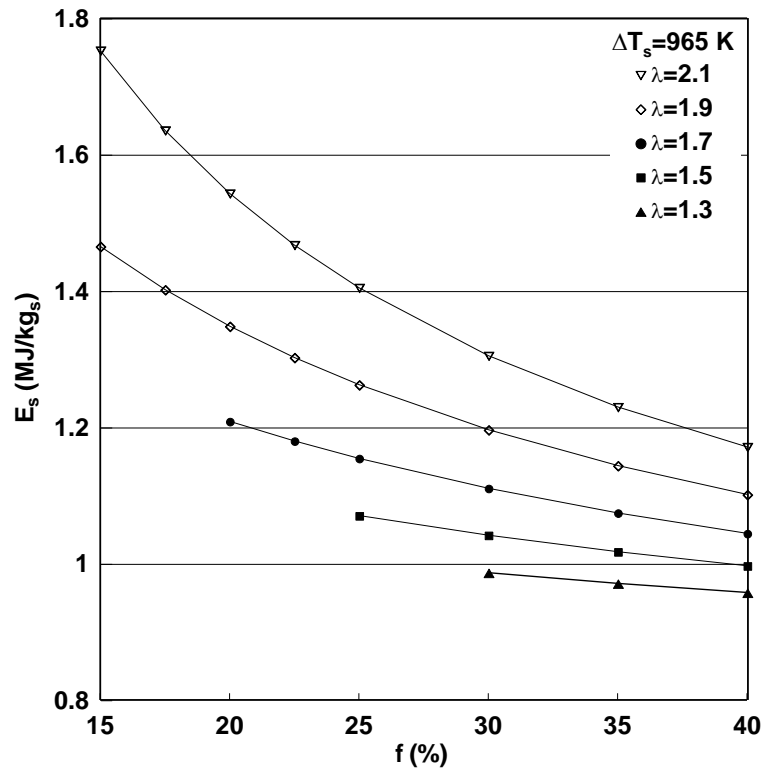
Figure 5.8: Energy consumption for all system.

Figure 5.9 and 5.10 show the temperature profiles for two values of f = 15 % and 20 % respectively with excess air number λ = 2.1. These figures demonstrate that the temperature profile of the vitrified clay pipes is nearly linear. In the figures the lower the escaped gas is, the higher the energy consumption which results in a higher flue gas temperature. Unfortunately, the temperature profiles for the kiln furniture solids differ from the industrial experience. The sharply decreasing in temperature profiles of kiln furniture materials is due to the assumed inlet temperature of these materials. Moreover, the values of f affect on the temperature profiles of the kiln furniture and the difference between T_{g_1} and T_{g_2}.

Figure 5.9: Temperature profile with excess air number of $\lambda = 2.1$ and f= 15 %.

Figure 5.11 shows the heat transfer coefficients α along the kiln for the two gas streams. From the figure, the heat transfer coefficients increase as the firing length increases for both streams. This increase is due to the increase of the mass flow of gas and therefore an increase of the Reynolds number. At th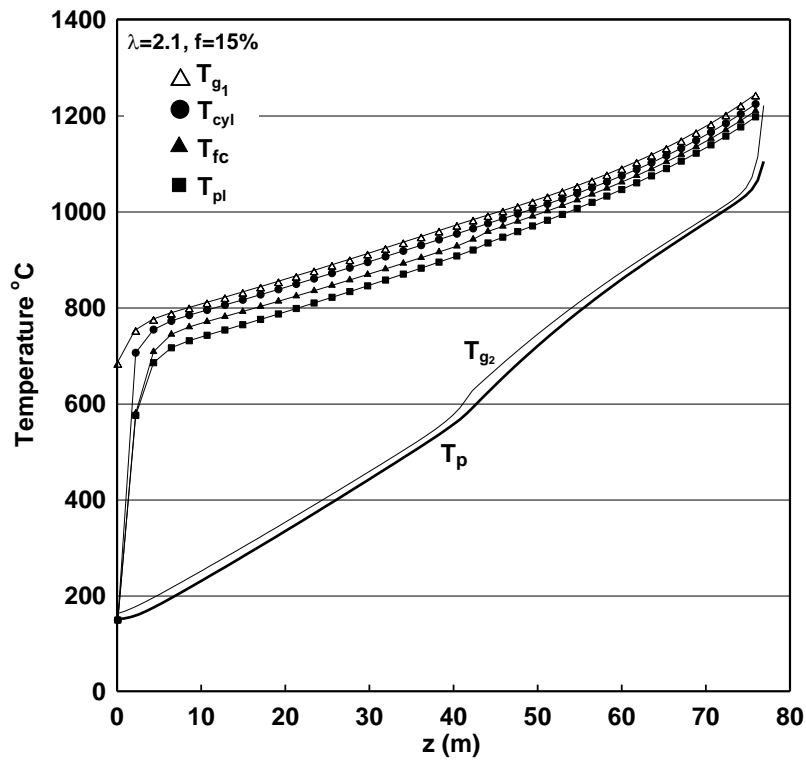e end of burning zone there is no more addition of gases, so that the maximum amount of gases passes through the preheating zone. Therefore, the heat transfer coefficients being almost constant along the preheating zone.

Figure 5.12 shows the radiative heat transfer coefficients along the kiln. In the figure, the heat transfer coefficients for both gas radiation and solid to solid radiation decrease as the firing length increases which are related to the decrease of the temperature along the kiln. Therefore, the heat transfer between gas and solid is very high. As a consequence, the temperature profiles of gas and solid are very close to each other as shown in the Fig 5.10.

The emissivities of carbon dioxide, ε_{CO2}, water vapor, ε_{H2O}, and gas$_{II}$ emissivity, ε_{g_2}, for excess air number of value $\lambda = 2.1$ and f = 20 % are shown in Fig. 5.13.
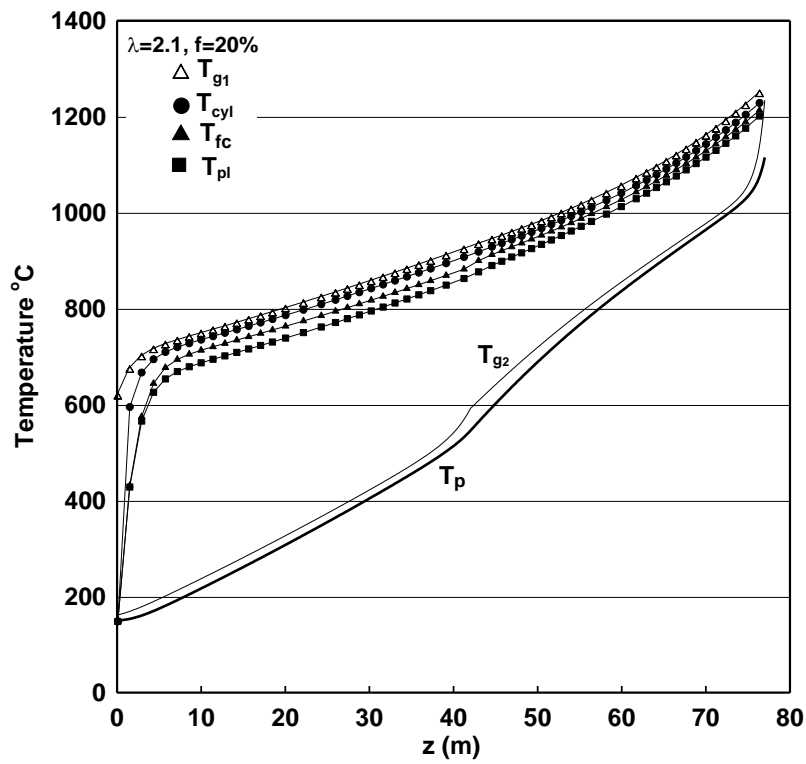
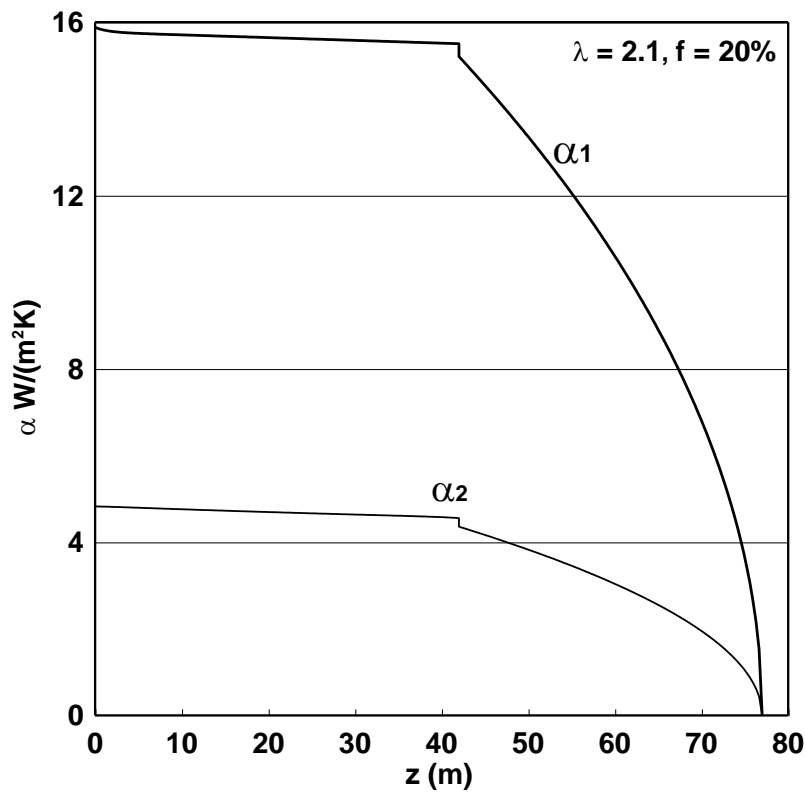Figure 5.10: Temperature profile with excess air number of $\lambda = 2.1$ and f= 20 %.

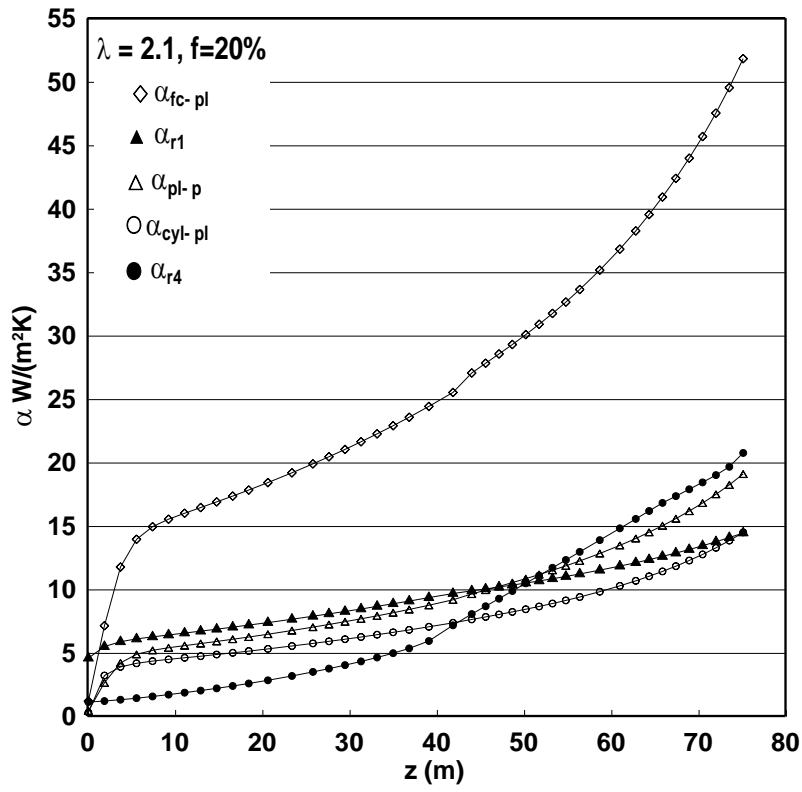Figure 5.11: Convective heat transfer coefficient (α) along the kiln.

Figure 5.12: Radiative heat transfer coefficient (α_r) along the kiln.
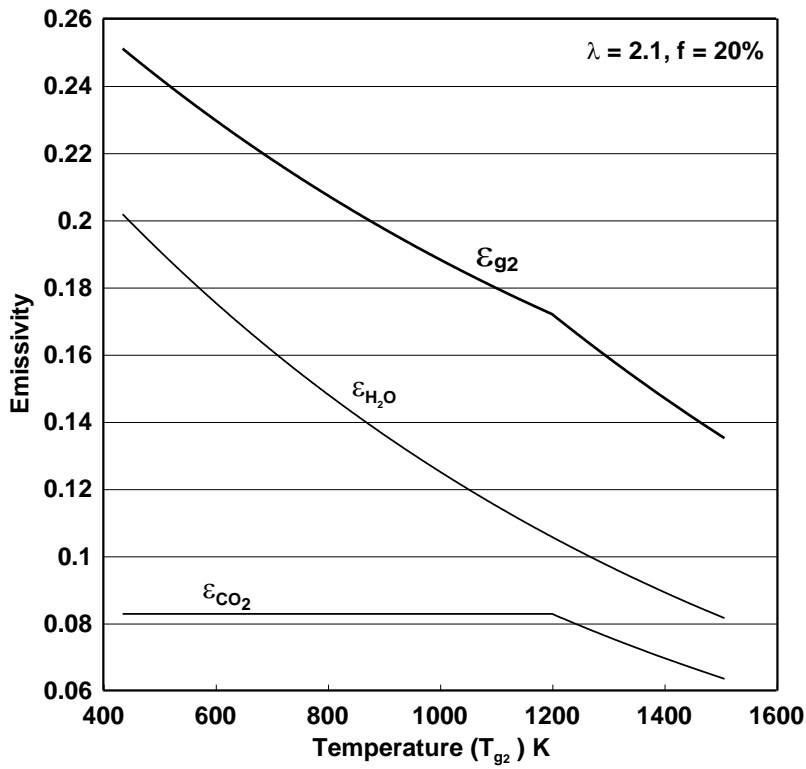
Figure 5.13: Emissivities of ε_{CO2}, ε_{H2O} and ε_{g2}.

Chapter 6

Sanitaryware Kiln

6.1   Introduction

The heat transfer mechanism is different from one kiln to another. The complexity of the mechanism depends on the type of products and its interaction with kiln car and kiln furniture. Furthermore, it is important in the tunnel kilns to have a good mixing of the gas around the products. Therefore, the technique of mixing is important and depends on the type of product and its sintering temperature. Sanitaryware kiln is an example of a kiln that requires a good mixing of the gases because of the complexity of the product shape. Figure 6.1 shows one type of the products which is produced in the Sanitaryware kiln. In this kiln there is a special way to thoroughly mix the preheating

Figure 6.1: Sanitaryware product.

zone. In the kiln there is an amount of air which is added in the preheating zone for mixing. The air is added through lateral nozzles. Therefore, it is important to establish a simplified model to understand the principal behavior of the kiln process and to analyze the heat transfer. This model considers the preheating and burning zone in which the solid materials (product, furniture, and car) are heated to the required heating temperature. Therefore, the following assumptions have to be made to perform analysis on this kiln.

Assumptions :

- The process is assumed to be a steady state process.

- The temperature of product and of gas is assumed to be constant at any cross section. As a consequence, the temperature depends only on the length.

- The temperature of product and transportation materials are the same.

- The heat losses through the walls are neglected.

- The fuel is distributed uniformly along the firing zone of length L_f.

- The air is distributed uniformly along the preheating zone of length L_{pre}.

- The solid material properties (specific heat capacity, density) are assumed as constant.

6.2 Case "A,new" with the new concept

6.2.1 Description of the case

As in chapter 3, the burning zone is considered with zero length. Therefore, the two zones are considered as one zone (preheating only). The new case is called case "A,new". The difference between case "A" and case "A,new" is the preheating zone has additional air nozzles in order to circulate the flue gases between the products. This circulation is done to achieve a homogenous mixture in order to uniformly heat the products during the preheating process. Figure 6.2 shows a schematic description of case "A,new". The gas is added from one position and the air is uniformly distributed along the preheating zone. According to the combustion of fuel in an assumed adiabatic combustion chamber, the outlet gas temperature from the combustion process is the adiabatic flame temperature. As illustrated in the figure, the kiln car carries the product through the kiln in counter direction to gas flow. Therewith, the kiln process is reduced to a simple counter current heat exchanger.
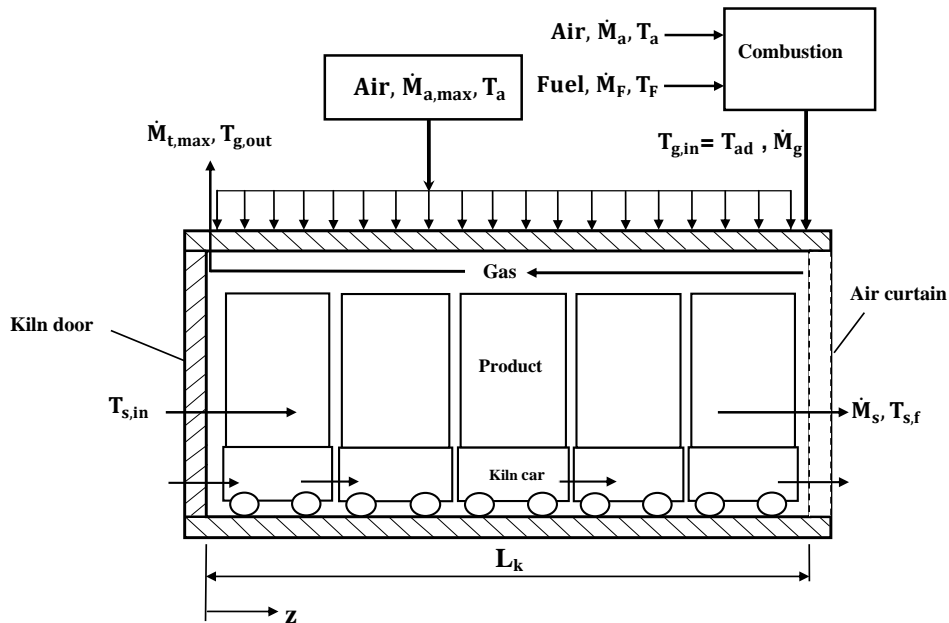

Figure 6.2: Schematic description of case "A,new".

6.2.2 The ordinary differential equations for gas and solid

For this heat exchanger the temperature profile of solid and gas can be calculated using an energy balance for a differential kiln length dz. The axial distribution of the added air

in the preheating zone is given as

$$\dot{M}_a(z) = \frac{\dot{M}_{a,max}}{L_{pre}} \left(L_{pre} - z \right). \tag{6.1}$$

Then with Eq. 3.41 the dimensionless form is obtained

$$\dot{M}_a(Z) = \frac{\dot{M}_{a,max} L_k}{L_{pre}} \left(\frac{L_{pre}}{L_k} - Z \right). \tag{6.2}$$

Where
L_k, the length of the kiln,
L_{pre}, the length of the preheating zone, and
$M_{a,max}$, the maximum mass flow rate of air.

Then by differentiation with respect to Z the following differential form for the air mass flow rate is obtained as

$$\frac{d\dot{M}_a}{dZ} = -\frac{\dot{M}_{a,max} L_k}{L_{pre}}. \tag{6.3}$$

From the description of the kiln, the air is added through nozzles and its maximum amount is calculated from the continuity equation as

$$\dot{M}_{a,max} = \rho_o A_{no} w_a N_{no}. \tag{6.4}$$

Where
A_{no}, the cross section area of nozzle,
w_a, the velocity of the injected air from the nozzle, and
N_{no}, the total number nozzles used.

The following table 6.1 shows some of the data used in the calculations.

Table 6.1: Part of the data used in the calculations

Symbol	Description	Value	Unit
D_{no}	nozzle diameter	0.021	m
ΔP	pressure drop through nozzle	20	mbar
sp	space between two nozzles	0.75	m

The following are the equations used to calculate the nozzle's numbers, the nozzle area and the velocity of air respectively

$$N_{no} = \frac{L_{pre}}{sp} - 1 \tag{6.5}$$

$$A_{no} = \frac{\pi}{4} D_{no}^2 \tag{6.6}$$

$$w_a = \sqrt{\frac{2\Delta P}{\rho_o}}. \tag{6.7}$$

- **Ordinary differential equation for gas**

The gas enthalpy flow for this new concept is expressed as

$$\dot{H}_t = \dot{M}_t(z)c_{pg}T_g(z). \tag{6.8}$$

There are two variables depending on length, z, so that the change in gas enthalpy flow is represented as

$$d\dot{H}_t = \dot{M}_t(z)c_{pg}dT_g + T_g c_{pg}d\dot{M}_t(z). \tag{6.9}$$

The axial distribution of the total gas in the preheating zone is given as

$$\dot{M}_t(z) = \frac{\dot{M}_{a,max}}{L_{pre}}\left(\frac{L_{pre}\dot{M}_{t,max}}{\dot{M}_{a,max}} - z\right). \tag{6.10}$$

Where
$M_{t,max}$, the total mass flow rate of gases; $M_{t,max} = M_{a,max} + M_{g,max}$.
Then with Eq. 3.41 the dimensionless form is obtained as

$$\dot{M}_t(Z) = \frac{\dot{M}_{a,max}L_k}{L_{pre}}\left(C_2 - Z\right). \tag{6.11}$$

and the constant C_2 is expressed as

$$C_2 = \frac{L_{pre}\dot{M}_{t,max}}{L_k\dot{M}_{a,max}}. \tag{6.12}$$

Then by differentiation with respect to Z the following differential form for the air mass flow rate is obtained as

$$\frac{d\dot{M}_t}{dZ} = -\frac{\dot{M}_{a,max}L_k}{L_{pre}}. \tag{6.13}$$

For this heat exchanger the temperature profile of the gas can be calculated using an energy balance for a differential kiln length dz. The gas enthalpy flow change $d\dot{H}_t$ is expressed as

$$d\dot{H}_t = d\dot{Q}_{conv} + d\dot{H}_{air}. \tag{6.14}$$

The convective heat transfer between the gas and solid is expressed by Eq. 3.14. For this case there is another source of enthalpy flow input of the added air $(d\dot{H}_{air})$ through the preheating zone which is represented as

$$d\dot{H}_{air} = T_{air}c_{pgo}\frac{\dot{M}_{a,max}}{L_{pre}}(-dz). \tag{6.15}$$

There is a negative sign in $d\dot{H}_{air}$, because the addition is in the opposite direction of z axes.

From the energy balance, the inlet energy to the element is equal to the

outlet one with neglecting heat loss. Solving Eqs. 3.14, 6.9 6.15 with Eq. 6.14 the following first order ordinary equation for the gas is obtained as

$$\dot{M}_t(z)c_{pg}dT_g + T_g c_{pg}d\dot{M}_t(z) = \frac{\alpha A_t}{L_k}(T_g - T_s)dz - T_{air}c_{pgo}\frac{\dot{M}_{a,max}}{L_{pre}}dz. \qquad (6.16)$$

Equation 6.16 can be represented in the following form as a general equation

$$\dot{M}_t(z)\frac{dT_g}{dz} = \frac{\alpha A_t}{L_k c_{pg}}(T_g - T_s) - \frac{\dot{M}_{a,max}}{L_{pre}c_{pg}}\left(c_{pgo}T_{air} - c_{pg}T_g\right). \qquad (6.17)$$

By substituting Eq. 6.11 in Eq. 6.17 the general form for the first order ordinary differential equation (ODE) is obtained as

$$(C_2 - Z)\frac{dT_g}{dZ} = St_a\frac{L_f}{L_k}(T_g - T_s) - \left(\frac{c_{pgo}}{c_{pg}}T_a - T_g\right). \qquad (6.18)$$

Where the Stanton number for the air is expressed as

$$St_a = \frac{\alpha A_t}{\dot{M}_{a,max}c_{pg}}. \qquad (6.19)$$

- **Ordinary differential equation for solid**

The solid enthalpy flow change is expressed by

$$d\dot{H}_s = \dot{M}_s c_s dT_s. \qquad (6.20)$$

For this heat exchanger the temperature profile of the solid can be calculated using an energy balance for a differential kiln length dz. The convective heat transfer between the gas and solid is expressed by Eq. 3.14. Then the following first order ordinary differential equation (ODE) for solid is obtained as

$$\frac{dT_s}{dz} = \frac{\alpha A_t}{\dot{M}_s c_s L_k}\left(T_g - T_s\right). \qquad (6.21)$$

And in dimensionless form the ODE for solid is expressed as

$$\frac{dT_s}{dZ} = St_s\left(T_g - T_s\right). \qquad (6.22)$$

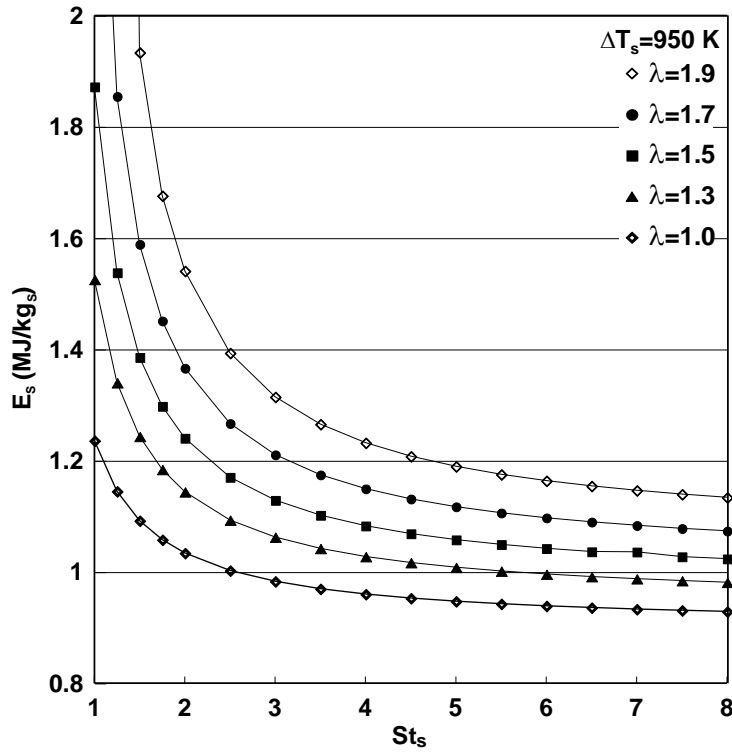Where the Stanton number for solid is expressed by Eq. 3.23.

Figure 6.3: Energy consumption from the numerical solution program of case "A,new".

6.2.3 Numerical solution

This section focuses on solving the two first order ODEs Eqs. 6.17 and 6.21 of gas and solid numerically. The commercial code (bvp4c) is used to solve this system of coupled ODE and boundary conditions. As stated before in chapter 3 the bvp4c solver needs two boundary conditions for the solution in which the solid inlet and outlet temperatures are known (inlet temperature of solid $T_{s,in}$, and outlet solid temperature $T_{s,f}$).

Figure 6.3 illustrates the energy consumption which is obtained from the bvp4c program of case "A,new". In the figure, for constant excess air number, the energy consumption decreases as Stanton number increases. The trend is the same for all excess air number. The Stanton number increases if the heat transfer coefficient (α) increases. The figure illustrates that for Stanton < 3, with a small decrease in Stanton number there is a big influence on the energy consumption for all excess air numbers. The figure shows also that as excess air number increase the energy consumption increase.

By comparing the results in Fig. 6.3 with the corresponding results in case "A" (Fig. **??**), it is obvious that the energy consumption in the new concept is higher than in simple case in chapter 3. The percentage of the increase for almost values of Stanton numbers is ranged from 10 % to 25 % for the different values of excess air number.

Regarding the previous analysis for case "A,new", there are many numerical results to display the temperature profile for both solid and gas for different Stanton number and excess air number. Some variables used in solving this system are listed in tables 3.1 and 6.1.

Figure 6.4 shows a comparison between the numerical solution of the case "A" and case "A,new" for $St_s = 2$ and $\lambda = 1.3$ with the corresponding value of energy consumption in each case. The figure demonstrates that the two cases are completely
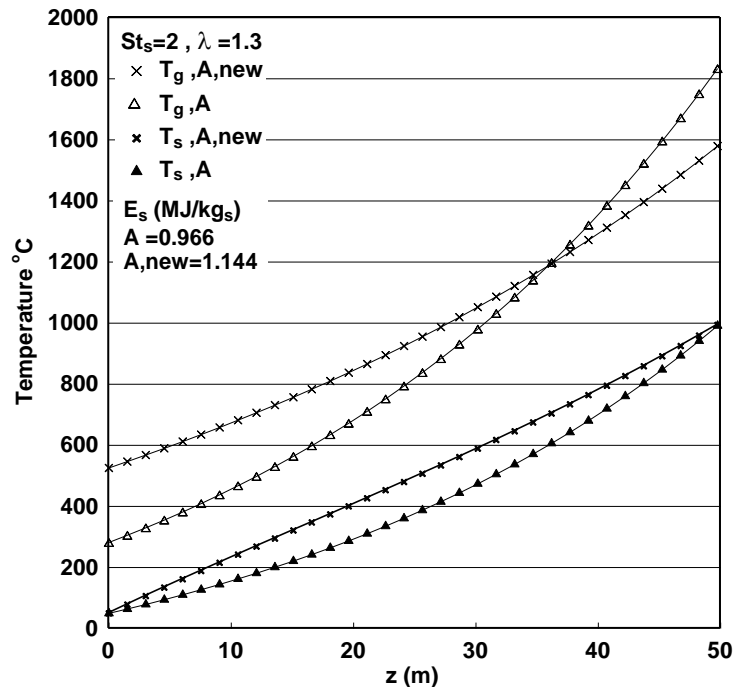

Figure 6.4: Temperature profiles of cases "A" and "A,new" for $St_s = 2$.

different in temperature profiles therewith the same outlet solid temperature. This can be attributed to the different energy consumption which is required in each case to satisfy the requirements as shown in the figure. The figure illustrates that the outlet gas temperature obtained from case "A,new" is approximately doubled the outlet temperature obtained from simple case "A". Also, the figure illustrates that the temperature profile of the solid is different. The solid curve shows that the heating of the material can be changed related to the required heating trend of the product. Therefore, the thermal heating of the material can be controlled according to the model results.

6.3 Case "C,new" with the new concept

6.3.1 Description of the case

In case "C,new" ($L_f = L_{pre}$) additional air nozzles are added to circulate the flue gases between the products as shown in Fig. 6.5. This circulation is done to achieve thorough mixing and good thermal heating of products during the preheating process. This figure shows that there is a homogeneous inlet of combustion gas along the burning zone.

1. **Burning zone ODEs for gas and solid**

   The ordinary differential equations for case "C,new" which represent gas and solid are the same as described before in chapter 3. Therefore, equation 3.51 represents
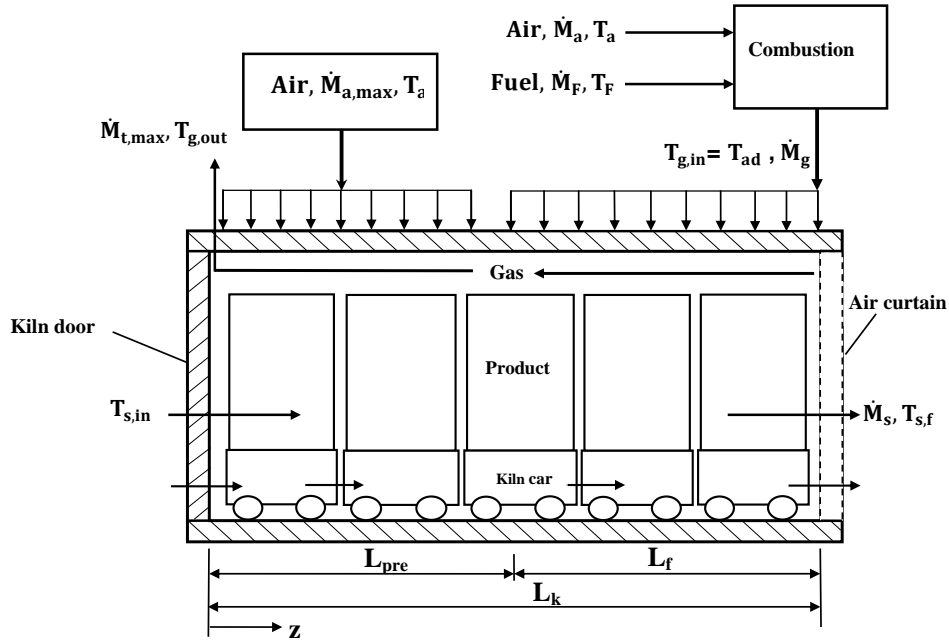
Figure 6.5: Schematic description for the second case "C,new".

the gas equation for the burning zone. Furthermore, equation 6.21 represent the ODE for solid in the burning zone.

2. **Preheating zone ODEs for gas and solid**

   The ordinary differential equations which represent the preheating zone in case "C,new" is the same as described before in case "A,new". Therefore, equation 6.18 represents the gas equation for the burning zone. Furthermore, equation 6.21 represent the ODE for solid in the preheating zone.

6.3.2 Numerical solution for case "C,new"

In the previous analysis the numerical solution with bvp4c code is used to solve the system. Then from the results the temperature profiles are obtained for both gas and solid along the two zones. As stated before in chapter 3 the bvp4c solver needs two boundary conditions for the solution in which the solid inlet and outlet temperatures are known (inlet temperature of solid $T_{s,in}$, and outlet solid temperature $T_{s,f}$).

Figure 6.6 illustrates the energy consumption as a function of Stanton number for different excess air numbers. The trend is the same for any excess air number therewith Stanton number increases from 1 to 3. The figure illustrates that for excess air number $\lambda < 1.5$ there are no logic results for a Stanton number > 3 (i.e. the results are obtained for a higher Stanton number, but the temperature of solid exceeds that of the gas in the burning zone). The figure demonstrates that for Stanton < 3, with a small decrease in Stanton number there is a big influence on the energy consumption E_s for all excess air numbers. The figure shows also that as excess air number increase the energy
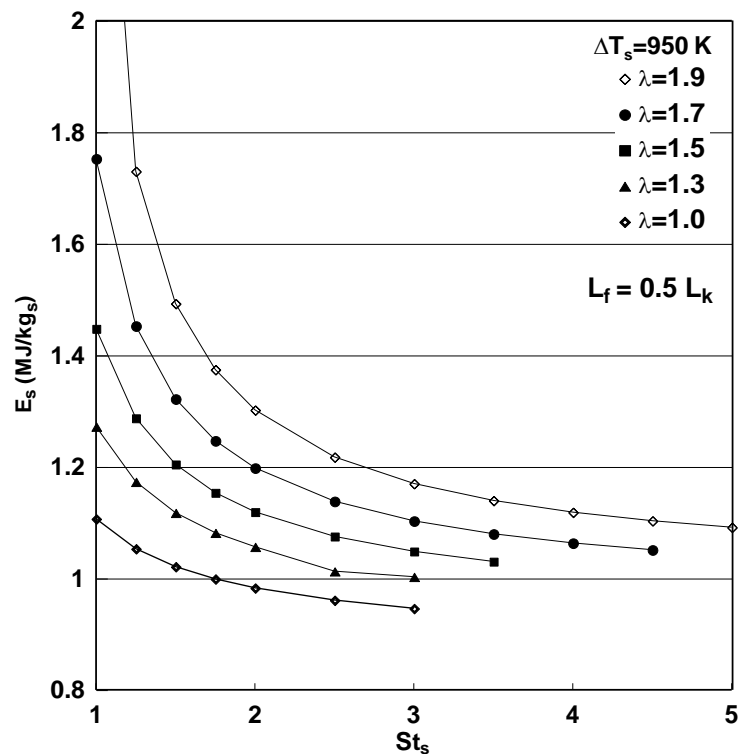
consumption increase.

Figure 6.6: Energy consumption from the numerical solution program of case "C,new".

By comparing the results in Fig. 6.6 with the corresponding results in case "C" (Fig. 3.15), it is obvious that the energy consumption in case "C,new" is mostly lower than that in case "C" in chapter 3.

Figure 6.7 shows a comparison between the numerical solution of the case "C" and case "C,new" for $St_s = 2$ and $\lambda = 1.3$ with the corresponding value of energy consumption in each case. The figure demonstrates that the two cases are approximately similar in temperature profiles thereby the same outlet solid temperature. Moreover, the figure illustrates that the outlet gas temperature obtained from case "C" is higher than the outlet temperature obtained from "C,new". This result is due to higher energy consumption in case "C". The figure shows that the temperature profile of the solid is increased linearly along the two zones and is nearly the same for both cases.

Figure 6.8 shows another comparison between the two cases for $St_s = 3$ and $\lambda = 1.3$. The figure shows that the two cases are different in temperature profiles thereby the same outlet solid temperature. Also, the figure illustrates that the outlet gas temperature obtained from case "C,new" is about 100 K higher than the outlet temperature obtained from "C". This result is due to higher energy consumption in case "C,new". Furthermore, the figure illustrates that the temperature profile of the solid is also different in the two cases.
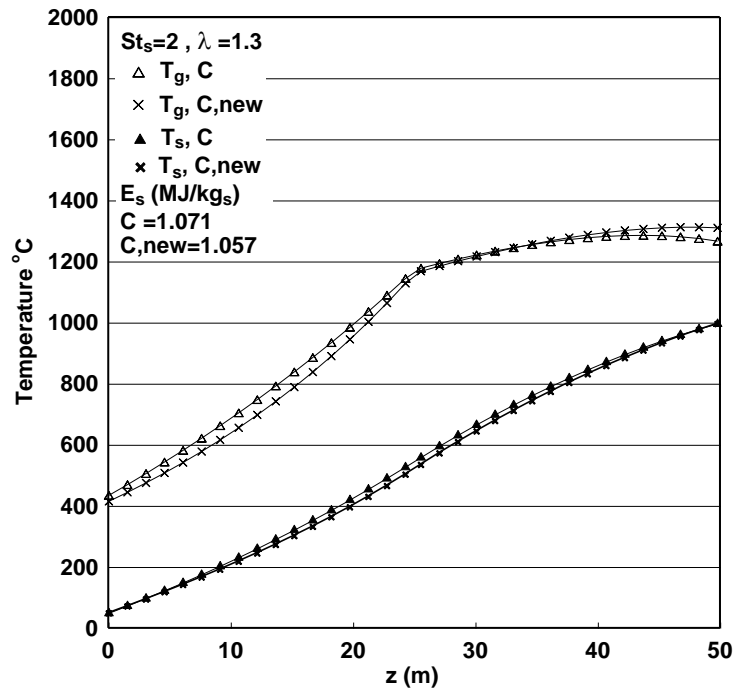
Figure 6.7: Temperature profiles of cases "C" and "C,new" for $St_s = 2$.
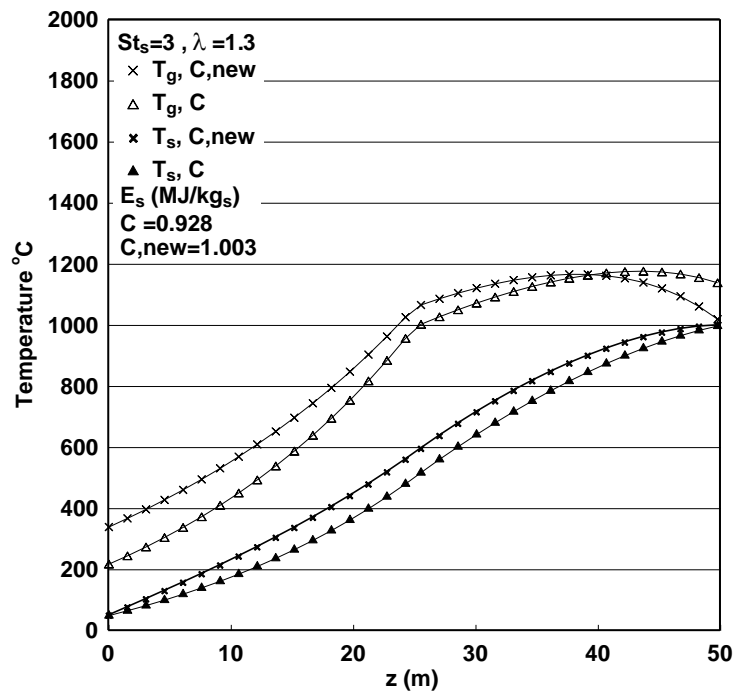
Figure 6.8: Temperature profiles of cases "C" and "C,new" for $St_s = 3$.

The heat transfer coefficient is calculated according to the following Eq. 4.35. Table 6.2 shows the heat transfer coefficient related to each Stanton number with the energy consumption. The heat transfer coefficient increases by about 76% if the excess air number changes from 1.3 to 2.1 thereby Stanton changes from 1.3 to 5.5 as in chapter4.

Table 6.2: Some results for case C,new

λ	St_s	$\alpha(\text{W}/(m^2 \cdot \text{K}))$	E (MJ/kg_s)	Ω
1.3	1.3	0.59	1.1598	0.7289
1.5	1.8	0.8	1.1458	0.826
1.7	2.5	1.1	1.1382	0.9258
1.9	3.5	1.6	1.1396	1.0323
2.1	5.5	2.5	1.1405	1.1386

6.4 Heat Transfer Analysis for Sanitaryware Kiln

Understanding the heat transfer coefficient helps in drawing the temperature profiles. There are two main types of heat transfer between the hot gases in the kiln and the solid materials, convection and radiation as stated before in chapter 5. The Sanitaryware products are not regular in shape as shown in Fig. 6.1. The kiln produces various products with different shapes. Consideration of the total surface area of the Sanitaryware which is exposed to gas flow, thereby heat transfer coefficient, it is unlikely to estimate an accurate value of overall rate of the convective heat transfer to the Sanitaryware. Therefore, to analyze the heat transfer in the Sanitaryware kiln the following assumptions are taken into consideration:

Assumptions :

- The Sanitaryware is roughly approximated as pipes with a staggered arrangement.

- There is no kiln furniture.

- The calculation considered only the convective heat transfer between the gases and the solid material.

It is obvious that the fuel is distributed uniformly along the burning zone. As a consequence, the gases are distributed uniformly along the burning zone which can be seen from Fig. 6.5. Furthermore, the air is distributed uniformly along the preheating zone. The following sections describe the heat transfer analysis in the burning and preheating zone. Furthermore, table 6.3 shows some of the data used in calculations.

6.4.1 Burning zone analysis

The axial distribution of gas flow equation along the burning length is represented by Eq. 3.44. Therefore, the ODE for the gas is represented as

$$\dot{M}_g(z)\frac{dT_g}{dz} = \frac{\alpha_b A_t}{L_k c_{pg}}(T_g - T_s) - \frac{\dot{M}_{g,max}}{L_f}(T_{ad} - T_g). \quad (6.23)$$

Where
$A_t = \pi D H_s N_{cars} N_{p,cars}$,
A_t, the total surface are of the pipes, and
H_s, the solid material height.

Table 6.3: Some of data used in the Sanitaryware kiln calculations

Symbol	Description	Value	Unit
B_k	kiln height	3.1	m
c_s	Specific heat of solid	0.9	$kJ/(kg.K)$
D	assumed diameter	0.4	m
D_N	nozzle diameter	0.021	m
H_{fur}	kiln furniture height	0.365	m
H_k	kiln height	1.195	m
H_s	solid height	0.63	m
hu	lower heating value	47300	kJ/kg_F
L_k	kiln height	50	m
$\dot{M}_s$	capacity of kiln	2.4	t/h
N_{cars}	number of cars	25	car
$N_{p,cars}$	number of pipes per car	33	pipes/car
S_L	longitudinal pitch	0.8D	m
S_T	transverse pitch	1.5D	m
$T_{s,in}$	solid inlet temperature	20	°C
$T_{s,f}$	solid outlet temperature	1200	°C
L	air demand	16.9	kg_{air}/kg_{fuel}

The gas passes across the assumed arrangement which is shown in Fig. 6.9. The convective heat transfer coefficient is calculated according to Eq. 4.12. Therefore, for the convective heat transfer coefficient is represented as

Figure 6.9: Schematic description of staggard arrangement.

$$\alpha_b = \frac{Nu\lambda_g}{D}.$$ (6.24)

Where
D, the assumed pipe outer diameter,
Nu, Nusselt number,
λ_g, the thermal conductivity of the gas, and
α_b, the convective heat transfer coefficient for the gas in the burning zone.

Nusselt number is calculated from Eq. 4.14 according to the analysis in chapter 4. The change in convective heat transfer is calculated according to Eq. 4.13.

The solid ODE is the same as stated before in chapter 3 in equation 3.21 and the ODE for solid is represented as

$$\frac{dT_s}{dz} = \frac{\alpha_b A_t}{\dot{M}_s c_s L_k} \left(T_g - T_s\right).$$

(6.25)

6.4.2 Preheating zone analysis

The axial distribution of total gas flow equation along the preheating length is represented by Eq. 6.10. The analysis for the gas in the preheating zone is represented by equation 6.17. Therefore, the ODE for the gas is represented as

$$\dot{M}_t(z)\frac{dT_g}{dz} = \frac{\alpha_{pre} A_t}{L_k c_{pg}}(T_g - T_s) - \frac{\dot{M}_{a,max}}{L_{pre} c_{pg}}\left(c_{pgo}T_a - c_{pg}T_g\right).$$

(6.26)

The convective heat transfer coefficient is calculated according to Eq. 4.12. Therefore, for the preheating zone the convective heat transfer coefficient is represented as
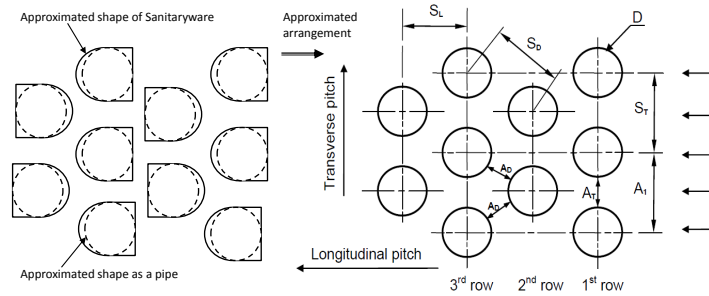
$$\alpha_{pre} = \frac{Nu\lambda_g}{D}.$$

(6.27)

Where
α_{pre}, the convective heat transfer coefficient for the gas in the preheating zone.

The solid ODE is the same as stated before in chapter 3 in equation 3.21. Therefore, the ODE for solid is represented as

$$\frac{dT_s}{dz} = \frac{\alpha_{pre} A_t}{\dot{M}_s c_s L_k} \left(T_g - T_s\right).$$

(6.28)

6.4.3 Numerical solution results

From the foregoing analysis, the bvp4c code is used to solve the system of ODEs. Then, the temperature profiles are obtained for both gas and solid along the two zones. The two boundary conditions for the solution in which the solid inlet and outlet temperatures are known, inlet temperature of solid $T_{s,in}$ and outlet solid temperature $T_{s,f}$ which are taken from table 6.3.

For that system of ODEs many trials had been done for the different excess air numbers till the logical solution is obtained (i.e. the temperature profile of gas is always higher than that of solid). Figure 6.10 shows the temperature profiles for gas and solid due to convective heat transfer analysis. In the figure, the excess air number has a higher value to obtain the results. The figure shows that the temperature profiles of gas and solid increase sharply during the preheating zone and weaker through the firing zone. Furthermore, the gas and solid profiles are too close to each other in the burning zone. The results are obtained at a high excess air number (λ= 2.1) and the energy consumed is E_s= 1.5243 MJ/kg_s.

Figure 6.11 shows the heat transfer coefficient, α, along the kiln. The convective heat transfer coefficient increases rapidly through the burning zone according to the gas

distribution along the zone and thereby increasing of Reynolds number. At the end of burning zone there is no more addition of gas so that the maximum amount of gas passes through the preheating zone. Therefore, the heat transfer coefficient is nearly constant along the preheating zone.
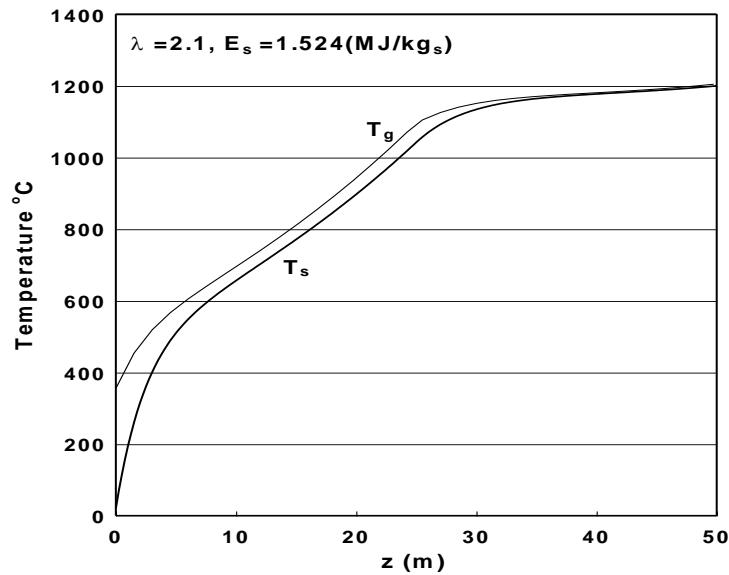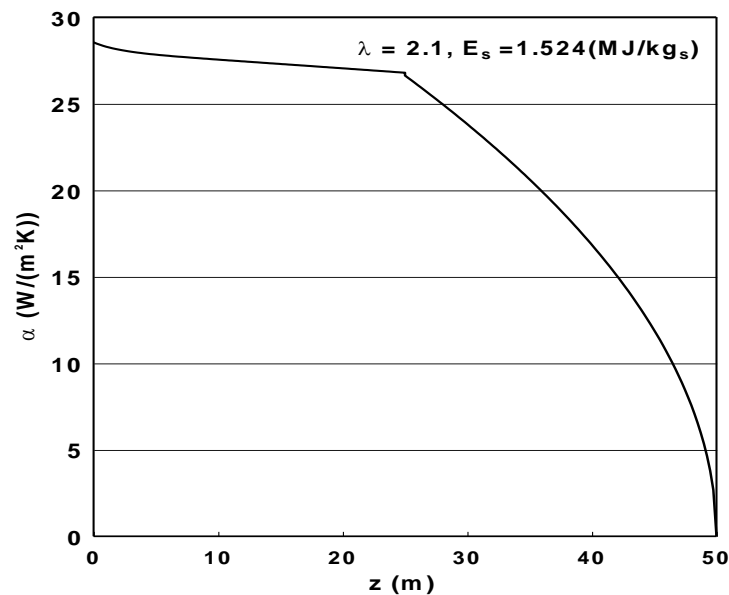
Figure 6.10: Temperature profiles $\lambda = 2.1$.

Figure 6.11: Convective heat transfer coefficient (α) along the kiln.

6.5 Flow field simulation with CFD

6.5.1 Introduction

The commercial CFD packages is one of the used codes for modeling and analyzing systems which involve fluid flow, heat transfer, and dissociative phenomena. There are some generalized equations which are used by FLUENT. The Navier Stokes equations for conservation of mass and momentum are used as a generalized equations to calculate laminar flow without heat transfer. Also, there are some additional equations which are used for solve heat transfer, species mixing or reaction or turbulent cases. There are three main elements in CFD simulation: Preprocessing, Solving, and Post-processing. This section concentrates on the use of FLUENT software package to simulate the flow field for the Sanitaryware kiln. The Fluent 6.2 Users Guide contains the basic equations and background of these equations [51]. The basic procedure steps to solve the problem by FLUENT are as follow:

1. Using Gambit to create the geometry, mesh, and specify the boundary types.

2. Start fluent by selecting 3D modeling.

3. Follow up fluent steps to import, check grids, select solver, and physical models.

4. Specify material properties and the boundary conditions.

5. Make the appropriate adjustments to start the solution.

6. Obtain the results from the program and make the analysis to these results.

For solving the problem by CFD program there are some assumptions which must be taken into consideration, the problem is steady state and the flow is incompressible. Figure 6.12 shows the 3D free domain for the part of the kiln with two nozzles, upper nozzle and lower nozzle. The full scale kiln geometry is extremely large. Therefore, a small part of the total kiln volume has been taken for 3D simulation as a computational domain in order to minimize the simulation time. Figure 6.13 shows a part of the kiln's geometry which is considered as symmetrical cuboid ($112\,cm$ length, $159\,cm$ width and $120\,cm$ in height). GAMBIT 2.2.30 package as a pre-processing program is used to generate the mesh. Unstructured mesh with tetrahedron mesh type is used in mesh generation of the computational domain as shown in Fig. 6.14. The standard k-ϵ model is the most popular and most widely used turbulence model, especially for industrial applications, but it depends on the computational domain. The model is a semi-empirical model which is based on model transport equations for the turbulent kinetic energy (k) and its dissipation rate (ϵ) [51]. For this work the realizable k-ϵ model is the recommended model from the FLUENT program for the shown domain.

• **Grid independence analysis**

A number of 3D meshes with increasing in the density of meshes to perform a mesh independence study to make sure that the solution is converged as the mesh size increases. Grid independent analysis was carried out for the computational domain. As shown in Fig. 6.15, the mesh number varied from 1,219,420 to 2,523,6790 cells. Based on this independence study there is no more change in the maximum velocity, so that the
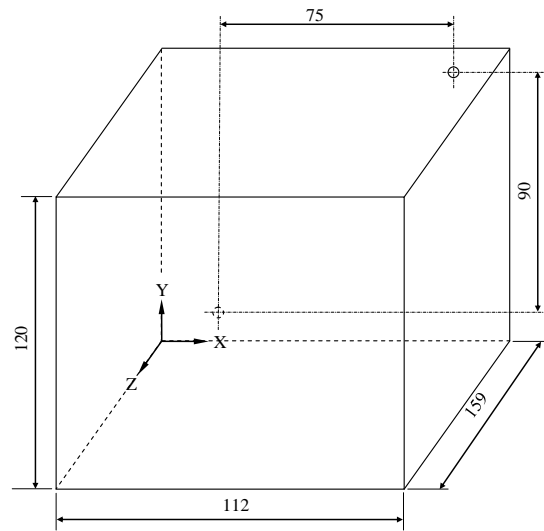
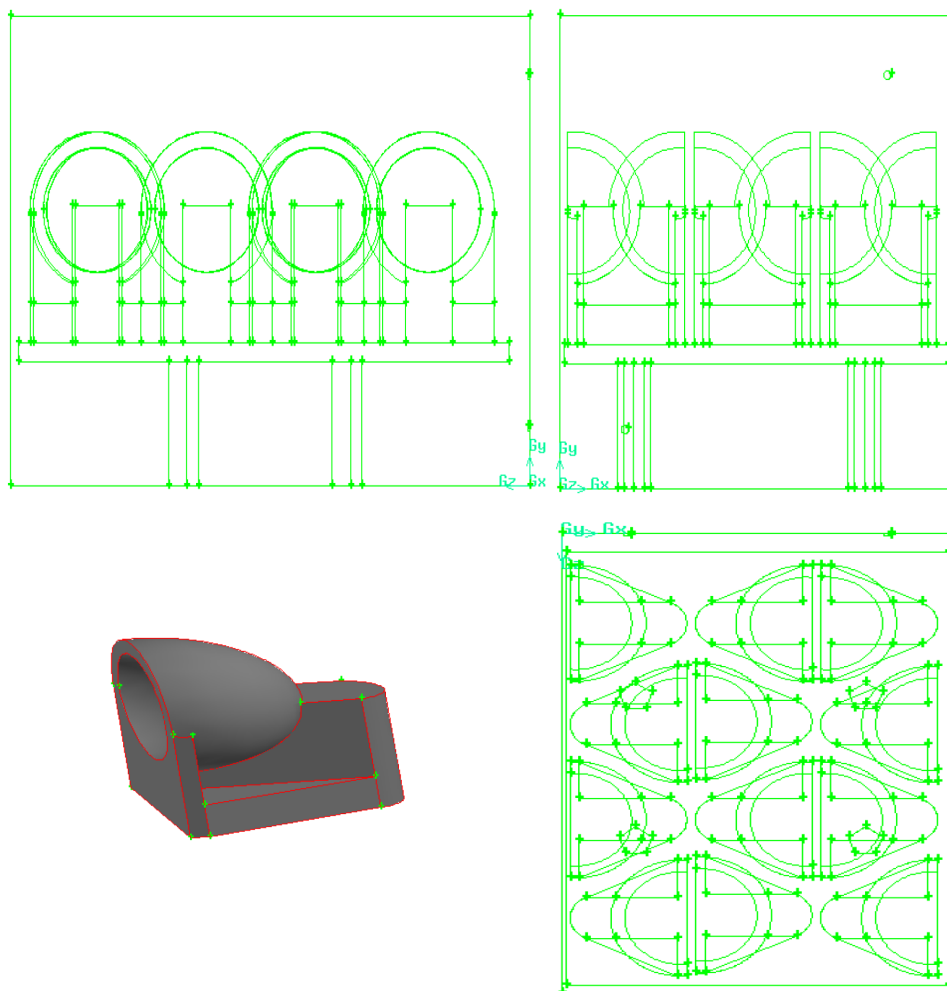Figure 6.12: The 3D free domain of the kiln (dimension in cm).

Figure 6.13: The three views of the 3D domain with the isometric of Sanitaryware piece.
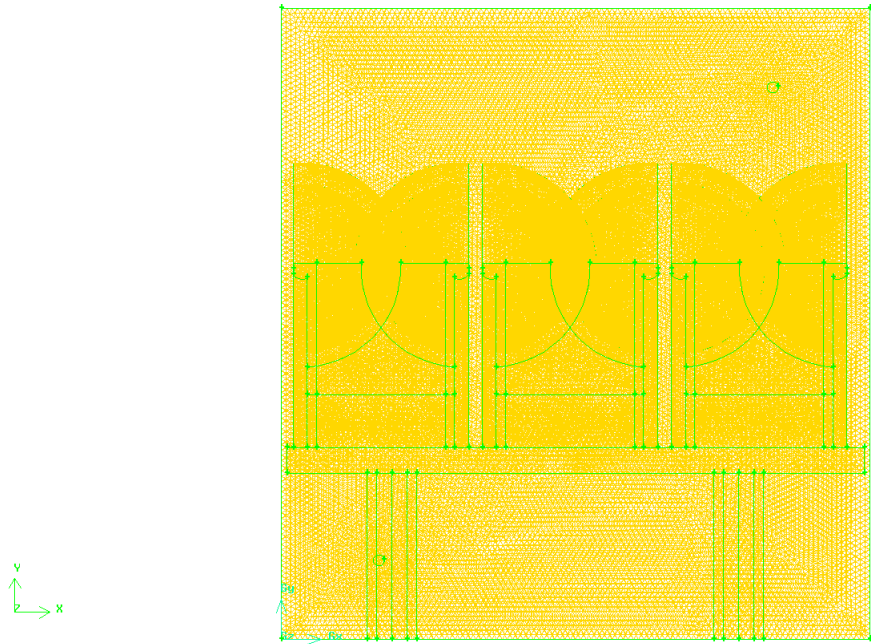
Figure 6.14: The computational domain.

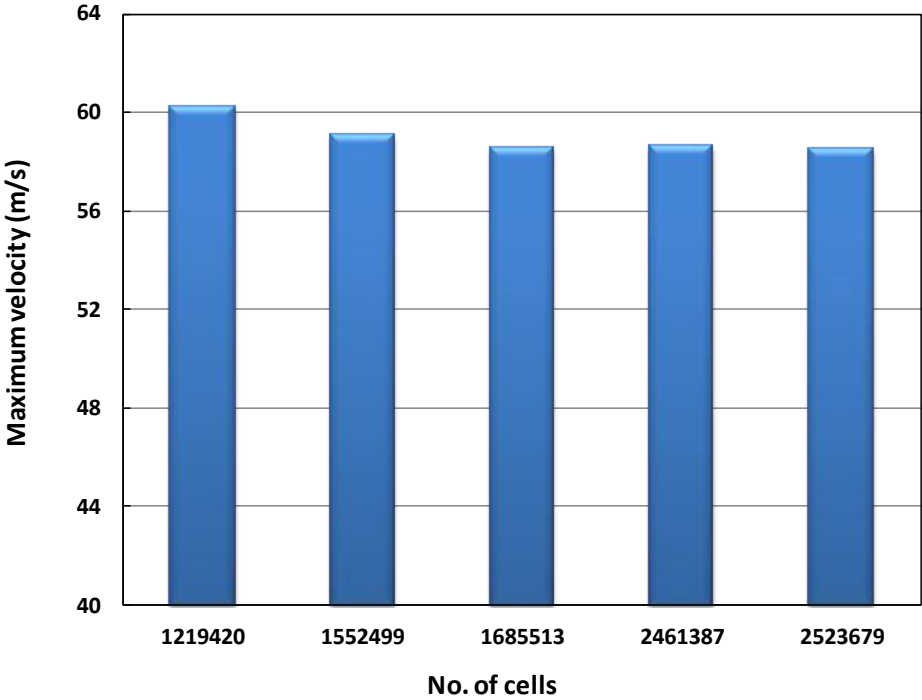cell numbers 2,461,387 is the recommended for further simulations for the computational domain.

Figure 6.15: Grid independence study for the computational domain.

6.5.2 CFD results

Meanwhile, an investigation for the gas flow in the preheating zone is carried out to show the gas circulation. Figure 6.16 shows the velocity vectors in a cross sectional plane of the computational domain. The shown plane passes through the upper nozzle in the computational domain. The figure illustrates the flow circulation in the cross section, it is evident that the flow circulation can be ensured between the products. The figure shows velocity vectors for a certain limit of the velocity in the computational domain. The figure demonstrates the flow circulations in the Sanitaryware gaps. The calculations also show that the average velocity inside the domain is around 1 m/s. The cross sectional velocity
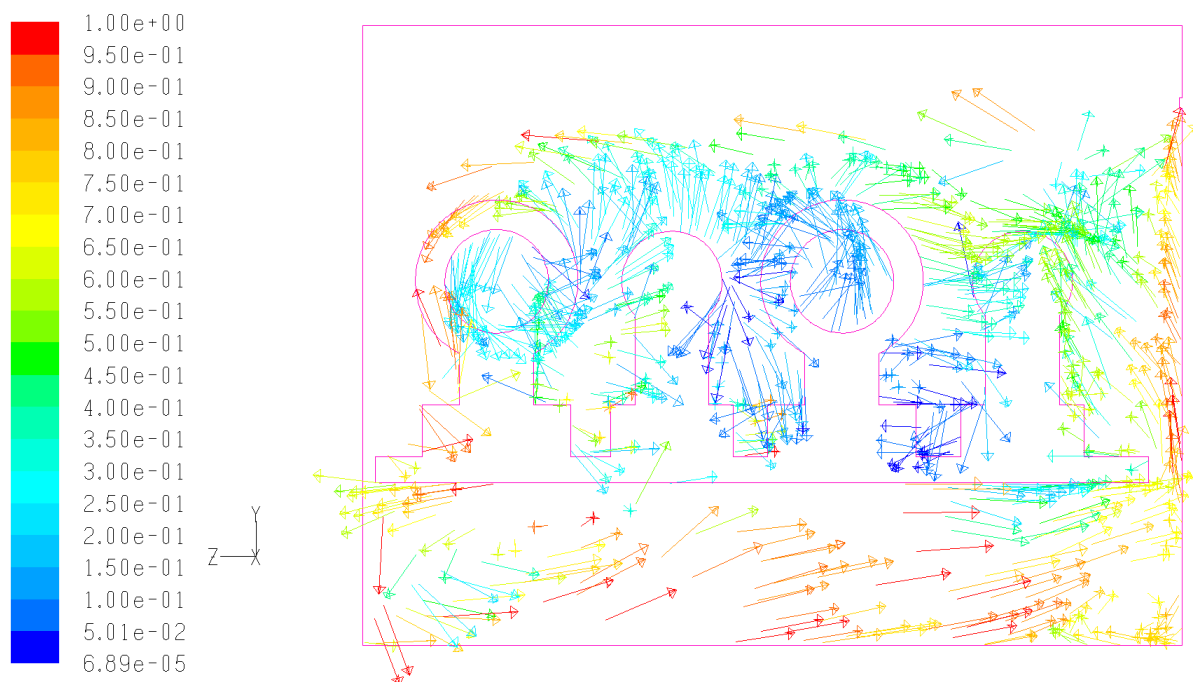

Figure 6.16: The velocity vector map colored by velocity.

profiles (Z direction) are plotted in Fig. 6.17. The figure shows the velocity profiles at three different levels in the same cross sectional plane. The flow is a typical turbulent flow velocity profile with some fluctuations on the velocity profile. The flow is very uneven due to the complex structure of the Sanitaryware. In Fig. 6.17, there are three lines, the first line (Line1) is placed over the Sanitaryware products. Therefore, the velocity profile is a continuous line and has regular velocity profile. The second and third lines (Line2 and Line3) are place in between the Sanitaryware products. Therefore, the velocity profiles are discontinuous, not homogenous, and appear in the free space between the solids.

The axial velocity profiles along the kiln length (X direction) are plotted in Fig 6.18. The figure shows the velocity profiles at three different levels. In Fig. 6.18, there are three lines, the first line (Line1) is placed over the Sanitaryware products. Therefore, the velocity profile is continuous line and has regular velocity profile. The second and third lines (Line2 and Line3) are place in between the Sanitaryware products. Therefore, the velocity profiles are discontinuous, not homogenous, and appear in the free space between the solids. Comparing the two velocity profiles for the cross sectional and the axial, it is clear obvious that the axial velocity is small; therefore, the heat transfer coefficient
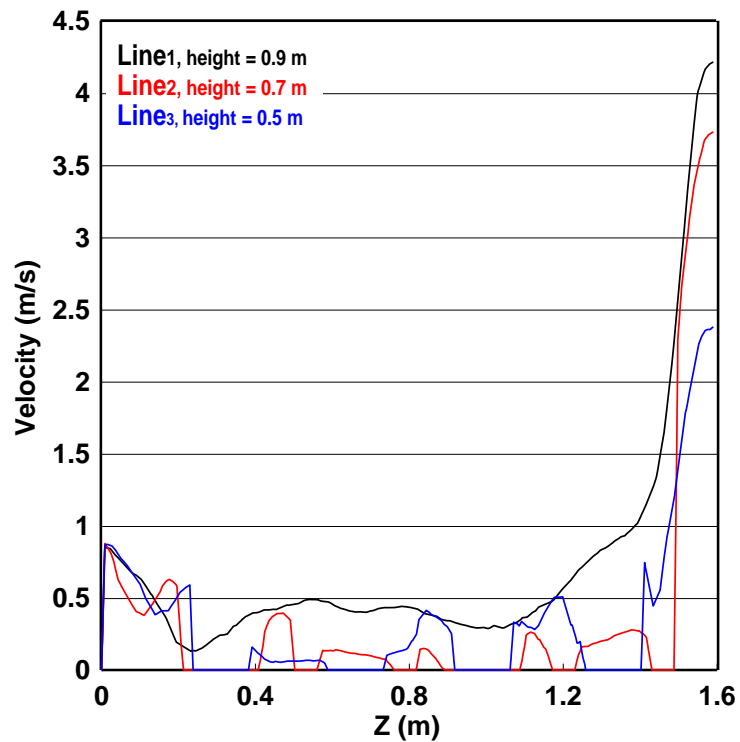
Figure 6.17: Velocity profiles in the cross section of the 3D domain.

is small. As a consequence, the radial velocity produced by the burner and nozzles is necessary in order to increase the heat transfer to decrease the energy consumption.
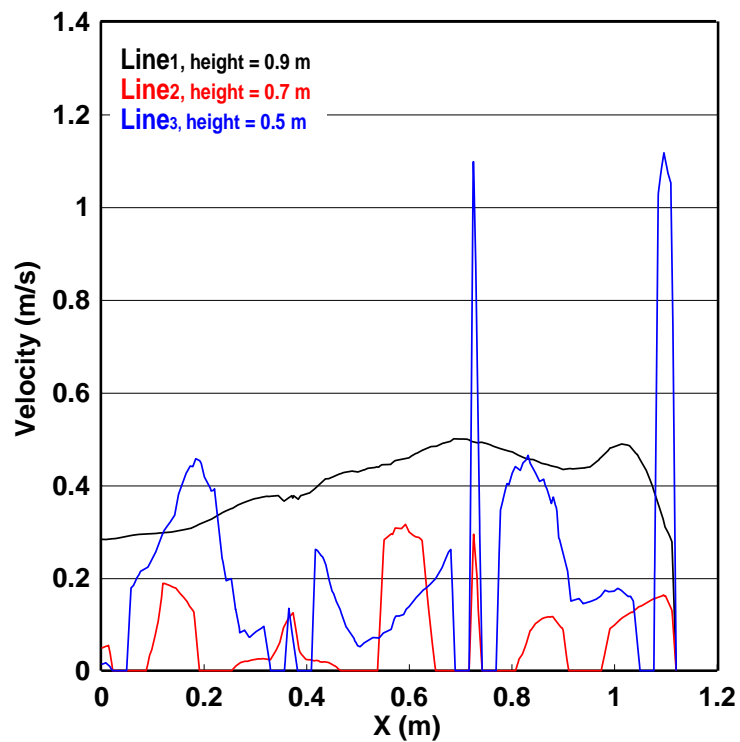

Figure 6.18: Velocity profiles in the longitudinal direction of the 3D domain.

Chapter 7

Conclusions and Outlook

7.1   Summary

A numerical model for simulating the process in the tunnel kiln is developed. The details of the mathematical model are described in the present work. The model predicts the temperature profiles of product, furniture, and gas along the preheating and firing zone in tunnel kilns. The model describes the method to obtain the ordinary differential equations for solids and gas in the preheating and firing zones. The developed mathematical model has been used to predict temperature profiles of different operating conditions (excess air number and Stanton number) on the energy consumption of the kiln.

A one dimensional mathematical model was established to analyze the heat transfer in the vitrified clay pipes kiln as a simple product. In addition 1D mathematical model was established for the Sanitaryware kiln to simulate the process inside the kiln. Moreover, another one dimensional mathematical model was established to analyze the heat transfer in the Sanitaryware kiln with a simplification of the products which looking like a pipe.

3D-CFD simulations using commercial CFD code (FLUENT 6.3) for preheating zone in Sanitaryware kiln were conducted and presented in order to study the flow field in the zone. Depending on the special dimension of the kiln, the CFD simulation can be applied particularly to simulate the flow field in the preheating zone.

7.2   Conclusions

The major conclusions from this work are represented in the following points:

- The higher the Stanton number the lower the energy consumption.

- The higher the excess air number the stronger is the influence of the heat transfer.

- The higher the excess air number the higher is the energy consumption resulting in a higher flue gas temperature.

- The firing zone length has a significant effect on the energy consumption and should be as short as possible for low energy consumption.

- A lower excess air number with higher Stanton number yields a lower flue gas temperature.

- The thesis contributes in understanding the process in the vitrified clay pipes tunnel kiln.

- The heat transfer is very low and it is between 1 and 5 W/m^2·K.

- The main radiation in the vitrified clay pipes kiln is from the plate to the top of the pipes.

- For the vitrified clay pipes kiln it is of great importance to change the pipes arrangement to allow gas passage between the pipes; therefore, enhancing the heat transfer and decreasing the energy consumption.

- If the heat transfer coefficient could be increased, then there is high potential to save the energy.

- The flow field for the preheating zone with air nozzles is simulated. So that, the cross section velocity is much higher than the axial velocity. This air jets dramatically improve the heat transfer which is advantageous in decreasing energy consumption.

7.3   Outlook

In the present study basic simplified equations to simulate the process in tunnel kilns have been introduced. Moreover, ordinary differential equations to analyze the heat transfer in the vitrified clay pipes kiln have been obtained. However, there are several areas where further analysis is required including:

- Experimental measurements should be carried out to verify the models (difficult in the present time).

- Study the effect of spacing between air nozzles on the results.

- Pipe to pipe radiation should be added to the mechanism.

- Including the wall radiation to the kiln (it need more data).

- The verification of the models used in this work should be done with advanced mathematical models and should be further developed to the tunnel kiln.

Appendix A

Boundary Value Problem Solver (BVP)

The boundary value problem solver (BVP) is one of the solvers which used to solve two-point boundary value problems for ordinary differential equations (ODEs). The ordinary differential equations (ODEs) describe a phenomena that change continuously. For solving the BVP a guess for the solution is required. There are parameters have to be determined so that the BVP has a solution. Furthermore, there might be more than one possibility, so that the program requires a guess for the parameters desired.

The bvp4c solver in MATLAB is the function which solves two-point boundary value problems for ordinary differential equations (ODEs). The bvp4c function integrates a system of first-order ordinary differential equations of the form,

$$z' = f(x; z) \tag{A.1}$$

on the interval [a; b], the equation is subject to general two-point boundary conditions,

g(z(a); z(b))=0.

This equation form also used to solve other types of boundary value problems which have any of the following; problems with unknown parameters, problems with singularities in the solutions and multi point conditions problems. For such cases, the number of boundary conditions must be sufficient to determine the solution of the problem and the unknown parameters.

The bvp4c function produces a continuous solution on the interval $[a; b]$ and has a continuous first derivative there. Furthermore, bvp4c code implements the 3-stage Lobatto IIIA formula. The Lobatto methods used for the numerical integration of differential equations which named after Rehuel Lobatto. The Lobatto methods are characterized by the use of approximations to the solution at the two end points. Due to their good stability properties, the Lobatto IIIA methods are used for boundary value problems (BVP). In the solver the mesh selection and error control are based on residual of the continuous solution. This mesh of points is used to divide the interval of integration into subintervals.

The numerical solution is obtained from this solver by solving a global system of

algebraic equations resulting from the boundary conditions and the collocation conditions imposed on all the subintervals. Then, the solver estimates the numerical solution error in each subinterval. Furthermore, the solver adapts the mesh and repeats the process when solution does not satisfy the tolerance criteria. Moreover, the points of the initial mesh must be provided by the user as an initial approximation of the solution at the mesh points.

Bibliography

[1] http://en.m.wikipedia.org/wiki/Ceramic engineering.

[2] http://www.epa.gov/ttnchie1/ap42/ch11/final/c11s07.pdf.

[3] J. Shular, *The Emission Factor Documentation for AP-42 Section 11.7: Ceramic Products Manufacturing for U.S*, 1996.

[4] O. Rentz, A. Schmittinger, R. Jochum, and F. Schultmann, "Exemplary investigation into the state of practical realisation of integrated environmental protection within the ceramics industry under observance of the IPPC-directive and the development of BAT reference documents, Research project 298 94 313/07," *Environmental Research Plan of the Federal Minister for the Environment, Nature Conservation and Safety*, 2001.

[5] http://www.gladdingmcbean.com.

[6] http://www.bathroomcity.co.uk/pdf/sanitaryware1 30.pdf.

[7] http://en.m.wikipedia.org/wiki/Porcelain.

[8] http://en.m.wikipedia.org/wiki/Ceramic.

[9] "Merkblatt über die Besten Verfügbaren Techniken in der Keramikindustrie," *Umweltbundesamt*, 2007.

[10] http://honeywell.com/Pages/Home.aspx, "Application profile tunnel kiln."

[11] V. De Paulo Nicolau and A. P. Dadam, "Numerical and experimental thermal analysis of a tunnel kiln used in ceramic production," *Journal of the Brazilian Society of Mechanical Sciences and Engineering*, vol. 31, no. 4, pp. 297–304, 2009.

[12] P. Meng, "Solid-solid Recuperation to Improve the Energy Efficiency of Tunnel Kilns," Ph.D. dissertation, Otto-von-Guericke-Universität, Magdeburg, Germany, 2011.

[13] D. R. Dugwell and D. E. Oakley, "Correlation of convective heat transfer data for tunnel kilns," *ZI, Ziegelindustrie International/Brick and Tile Industry International*, vol. 42, no. 10, pp. 536–545, 1989.

[14] S. A. Karaush, Y. I. Chizhik, and E. G. Bober', "Optimization of ceramic setting as a function of their heat absorption from the radiating walls of the furnace," *Glass and Ceramics (English translation of Steklo i Keramika)*, vol. 54, no. 5-6, pp. 190–192, 1997.

[15] H. Z. Abou-Ziyan, "Convective heat transfer from different brick arrangements in tunnel kilns," *Applied Thermal Engineering*, vol. 24, no. 2-3, pp. 171–191, 2004.

[16] O. B. Gol'tsova, V. S. Klekovkin, O. B. Nagovitsin, and S. V. Antonychev, "Heat losses in a tunnel kiln for brick firing," *Glass and Ceramics (English translation of Steklo i Keramika)*, vol. 63, no. 3-4, pp. 127–129, 2006.

[17] S. Vogt and M. Beckmann, "Convective heat transfer on brick settings," *ZI, Ziegelindustrie International/Brick and Tile Industry International*, vol. 60, no. 9, pp. 34–49, 2008.

[18] V. Mandhani, R. Chhabra, and V. Eswaran, "Forced convection heat transfer in tube banks in cross flow," *Chemical Engineering Science*, vol. 57, no. 3, pp. 379 – 391, 2002.

[19] J. Kang and Y. Rong, "Modeling and simulation of load heating in heat treatment furnaces," *Journal of Materials Processing Technology*, vol. 174, no. 1-3, pp. 109–114, 2006.

[20] F. H. Becker, G. Walter, and L. Lorenz, "Heat exchange in a fast firing kiln for glost firing of porcelain," *CFI Ceramic Forum International*, vol. 83, no. 9, pp. E59–E65, 2006.

[21] V. G. Abbakumov, "Analyzing the heating and cooling of products in a high temperature tunnel kiln," *Refractories*, vol. 9, no. 1-2, pp. 77–83, 1968.

[22] D. R. Dugwell and D. E. Oakley, "Simulation of tunnel kilns for firing refractory products," *British ceramic. Transactions and journal*, vol. 86, no. 5, pp. 150–153, 1987.

[23] B. Yu, "Dynamic modeling of a tunnel kiln," *Heat Transfer Engineering*, vol. 15, no. 2, pp. 39–53, 1994.

[24] R. H. Essenhigh, "Studies in furnace analysis: Prediction of tunnel kiln performance by application of the integral energy equation," *Energy and Fuels*, vol. 15, no. 3, pp. 552–558, 2001.

[25] J. Durakovic and S. Delalic, "Temperature field analysis of tunnel kiln for brick production," *RMZ - Materials and Geoenvironment*, vol. 53, no. 3, pp. 403–408, 2006.

[26] O. B. Gol'tsova, V. S. Klekovkin, and V. A. Tenenev, "Development and approval of a mathematical model of a brick firing kiln," *Glass and Ceramics (English translation of Steklo i Keramika)*, vol. 65, no. 3-4, pp. 100–102, 2008.

[27] E. Mancuhan, K. Kücükada, and E. Alpman, "Mathematical modeling and simulation of the preheating zone of a tunnel kiln," *Isi Bilimi Ve Teknigi Dergisi/ Journal of Thermal Science and Technology*, vol. 31, no. 2, pp. 79–86, 2011.

[28] M. Z. Shvartsman, I. P. Tsibin, and G. A. Ketslakh, "The uniformity of firing and fuel economics in tunnel kilns," *Refractories*, vol. 20, no. 11-12, pp. 735–739, 1980.

[29] E. Mancuhan and K. Kucukada, "Optimization of fuel and air use in a tunnel kiln to produce coal admixed bricks," *Applied Thermal Engineering*, vol. 26, no. 14-15, pp. 1556–1563, 2006.

[30] S. Kaya, E. Mancuhan, and K. Kücükada, "Modelling and optimization of the firing zone of a tunnel kiln to predict the optimal feed locations and mass fluxes of the fuel and secondary air," *Applied Energy*, vol. 86, no. 3, pp. 325–332, 2009.

[31] T. S. Possamai, R. Oba, V. Nicolau, and O. Otte, "Numerical simulation of a ceramic kiln used in frits production," in *20th International Congress of Mechanical Engineering , Gramado, RS, Brazil COB09 1152*, November 2009.

[32] R. Oba, T. S. Possamai, A. T. Nunes, and V. De Paulo Nicolau, "NUMERICAL SIMULATION OF TUNNEL KILNS APPLIED TO WHITE TILE WITH NATURAL GAS," in *21st Brazilian Congress of Mechanical Engineering, Natal, RN, Brazil COBEM 2011*, October 2011.

[33] V. G. Abbakumov and S. I. Vel'sin, "Thermal operation of the firing zone of an automated tunnel kiln," *Refractories*, vol. 27, no. 9-10, pp. 541–546, 1986.

[34] Z. Chen, H. Zhang, and Z. Zhu, "An integrated intelligent system for ceramic kilns," *Expert Systems with Applications*, vol. 16, no. 1, pp. 55–61, 1999.

[35] P. Michael and S. Manesis, "Modelling and control of industrial tunnel-type furnaces for brick and tile production," *Proceeding of the 5th Int.Conference on Technology and Automation, Patras, GR-26500, Greece*, pp. 216–221, 2005.

[36] J. B. De Wit, "Use of energy-saving tunnel kiln cars in the ceramic industry," *ZI, Ziegelindustrie International/Brick and Tile Industry International*, vol. 42, no. 10, 1989.

[37] M. D. G. Carvalho and M. Nogueira, "Improvement of energy efficiency in glass-melting furnaces, cement kilns and baking ovens," *Applied Thermal Engineering*, vol. 17, no. 8-10, pp. 921–933, 1997.

[38] B. A. Unaspekov, "Operation of a combined gas heating system for firing refractory components in a tunnel funnel at the Kazogneupor plant," *Refractories and Industrial Ceramics*, vol. 43, no. 9-10, pp. 319–321, 2002.

[39] E. Specht, "Kinetik der Abbaureaktionen," *Cuvillier Verlag, Göttingen*, 1993.

[40] Y. A. Cengel and A. J. Ghajar, *Heat and Mass Transfer: Fundamentals and Applications*.   McGraw-Hill Companies, Inc., U.S.A., 2011.

[41] A. Zukauskas, "Heat Transfer from Tubes in Crossflow," ser. Advances in Heat Transfer, J. P. Hartnett and T. F. Irvine, Eds.   Elsevier, 1972, vol. 8, pp. 93 – 160.

[42] E. C. Huge, "Experimental investigation of effects of equipment size on convection heat transfer and flow resistance in cross flow of gases over tube banks," *Trans.ASME*, vol. 59, no. 7, pp. 573–581, 1937.

[43] O. L. Pierson, "Experimental investigation of the influence of tube arrangement on convection heat transfer and flow resistance in cross flow of gases over tube banks," *Trans.ASME*, vol. 59, no. 7, pp. 563–572, 1937.

[44] H. Hausen, "The pressure drop accompanying fluid flow through tubes and ducts," *Heat Transfer in Counterflow, Parallel-flow, and Cross-flow*, 1983.

[45] W. Khan, J. Culham, and M. Yovanovich, "Convection heat transfer from tube banks in crossflow: Analytical approach," *International Journal of Heat and Mass Transfer*, vol. 49, no. 25-26, pp. 4831 – 4838, 2006.

[46] D. Vortmeyer and S. Kabelac, "K3 Gas Radiation: Radiation from Gas Mixtures," in *VDI Heat Atlas*, 2010, pp. 979–988.

[47] E. Specht, *Lecture Note of Combustion Engineering.* University of Magdeburg, Germany, 2008.

[48] ——, *Lecture Note of Advanced Heat and Mass Transfer.* University of Magdeburg, Germany, 2008.

[49] J. H. Lienhard IV and J. H. V. Lienhard, *A Heat Transfer Textbook Third Edition.* Phlogiston press Cambridge, Massachusetts, U.S.A., 2004.

[50] W. M. Rohsenow, J. P. Hartnett, and Y. I. Cho, *Handbook of Heat Transfer Third edition.* McGraw-Hill Companies, Inc., U.S.A., 1998.

[51] F. Inc., *FLUENT 6.3 User's Guide, Tutorial Guide, FLUENT User Services Center.* Fluent Inc., Lebanon, NH, 2006.

Curriculum Vitae

Personal Information

Name:	Hassanein Refaey
Birth date:	07.02.1978 in Qaliubiya, Egypt
Nationality:	Egyptian
E-mail:	hassanein_refaey@yahoo.com
Social status:	Married, 2 children

Education

1984 - 1989	Elementary school, Senduin, Qaliubiya, Egypt.
1989 - 1992	Primary school, Senduin, Qaliubiya, Egypt.
1992 - 1995	Secondary school, Senduin, Qaliubiya, Egypt.
1995 - 2000	B.Sc. in Mechanical Power Engineering, Faculty of Engineering at Shoubra, Benha University, Cairo, Egypt.
2001 - 2003	Postgraduate courses for M.Sc. in Mechanical Power Engineering, Faculty of Engineering at Shoubra, Benha University, Cairo, Egypt.
2003 - 2006	M.Sc. in Mechanical Power Engineering, Faculty of Engineering at Shoubra, Benha University, Cairo, Egypt.
Sep. 2009 - Till now	Ph.D. in Engineering (Dr.-Ing.), Faculty of Process and System Engineering, Otto von Guericke University Magdeburg, Germany.

Work Experience:

2002 - 2006	Demonstrator at Faculty of Engineering at Shoubra, Benha University, Cairo, Egypt.
2006 - 2009	Assistant lecturer at Faculty of Engineering at Shoubra, Benha University, Cairo, Egypt.
Sep. 2009 - Till now	Scientific assistant (Ph.D student) at Otto von Guericke University, Magdeburg, Germany.

Magdeburg, 30 January 2013
Hassanein Refaey